Measurement of the $D^{*\pm}$ Meson Production Cross Section and $F_2^{c\bar{c}}$ at High Q^2 in ep Scattering at HERA

by

Martin Brinkmann

Measurement of the $D^{*\pm}$ Meson Production Cross Section and $F_2^{c\bar{c}}$ at High Q^2 in ep Scattering at HERA

Dissertation

zur Erlangung des Doktorgrades
des Department Physik
der Universität Hamburg

vorgelegt von

Martin Brinkmann

aus Hamburg

Hamburg
2010

Gutachter der Dissertation:	Dr. Katerina Lipka Prof. Dr. Robert Klanner
Gutachter der Disputation:	Dr. Katerina Lipka Prof. Dr. Peter Truöl
Datum der Disputation:	25. März 2010
Vorsitzender des Prüfungsausschusses:	Prof. Dr. Dieter Horns
Vorsitzender des Promotionsausschusses:	Prof. Dr. Jochen Bartels
Leiterin des Department Physik:	Prof. Dr. Daniela Pfannkuche
Dekan der MIN Fakultät:	Prof. Dr. Heinrich Graener

Abstract

The inclusive production cross section of $D^{*\pm}(2010)$ mesons in deep-inelastic $e^{\pm}p$ scattering is measured in the kinematic region of photon virtuality $100 < Q^2 < 1000\,\mathrm{GeV}^2$ and inelasticity $0.02 < y < 0.7$. Single and double differential cross sections for inclusive D^* meson production are measured in the visible range defined by $|\eta(D^*)| < 1.5$ and $p_T(D^*) > 1.5\,\mathrm{GeV}$. The data were collected by the H1 experiment during the period from 2004 to 2007 and correspond to an integrated luminosity of $351\,\mathrm{pb}^{-1}$. The charm contribution, $F_2^{c\bar{c}}$, to the proton structure function F_2 is determined. The measurements are compared with QCD predictions.

Kurzfassung

Es wird der inklusive Erzeugungswirkungsquerschnitt von $D^{*\pm}(2010)$ Mesonen in tief-unelastischer ep-Streuung in dem kinematischen Bereich der Photonvirtualität $100 < Q^2 < 1000\,\mathrm{GeV}^2$ und der Inelastizität $0.02 < y < 0.7$ gemessen. Einfach und doppelt differentielle Wirkungsquerschnitte für inklusive D^* Meson Erzeugung werden in einem Bereich des Phasenraumes gemessen, der definiert ist durch $|\eta(D^*)| < 1.5$ und $p_T(D^*) > 1.5\,\mathrm{GeV}$. Die Daten wurden vom H1 Experiment aufgezeichnet in den Jahren 2004 bis 2007 entsprechend einer integrierten Luminosität von $351\,\mathrm{pb}^{-1}$. Der Beitrag des Charm-Quarks, $F_2^{c\bar{c}}$, zur Protonstrukturfunktion F_2 wird bestimmt. Die Messungen werden mit Vorhersagen der Quantenchromodynamik verglichen.

Contents

Introduction

The standard model of particle physics, established during the last decades, is a very successful theory. The standard model describes most of the phenomena observed in elementary particle physics except gravity. It includes the theory of electro-weak interactions and the theory of strong interactions, also called quantum chromo dynamics (QCD). The theoretical predictions, for both theories, are usually based on perturbative calculations. However in QCD, due to the nature of the strong coupling, only processes with large momentum transfer can be calculated perturbatively, which limits the predictive power of this theory.

An excellent experimental testing ground to test QCD is deep-inelastic scattering of leptons on nucleons where the exchanged photon is utilized to probe the nucleon. Deep-inelastic scattering experiments played a major role for the measurement of the nucleon structure, which is dominated by QCD effects. These experiments started as fixed-target experiments at low center of mass energies. The HERA[1] accelerator at DESY[2] in Hamburg, where electron and proton beams have been collided, allowed the access to much higher energies than realized at existing fixed target experiments. At HERA many aspects of the standard model, in particular of QCD have been confirmed with high experimental precision. Nowadays, HERA results represent the ultimate knowledge of QCD and nucleon structure.

An elegant way of testing perturbative QCD (pQCD) in deep-inelastic scattering (DIS) at HERA is offered by the processes which involve production of charm quarks since their large mass of $\approx 1.5\,\mathrm{GeV}$ already provides a hard scale for perturbative calculations. Significant contributions to charm production at HERA arise from the boson-gluon fusion process where the exchange boson interacts with a gluon from the proton via a $c\bar{c}$ pair. This process is therefore sensitive to the gluon density in the proton. Thus measurements of charm production at HERA yield very important information on the gluon content of the proton. Therefore, a proper treatment of charm quark mass effects in perturbative QCD models is an important issue in the determination of parton distribution functions (PDFs). Different schemes to incorporate these effects are available and can be tested.

[1] Hadron-Elektron-Ring-Anlage

[2] Deutsches Elektronen-Synchrotron.

The charm production cross section in ep scattering can be estimated using the factorisation theorem in perturbative QCD as a convolution of parton distributions in the proton, the perturbatively calculable hard matrix element and the fragmentation of the charm quarks into hadrons.

Via the measurement of charm production at high photon virtuality Q^2 the reliability of recent pQCD calculations of the hard matrix element can be tested accurately, since the theoretical uncertainties are smaller than at lower Q^2. Especially the extrapolation of the measured cross sections to the full phase space is less model dependent since at higher Q^2 the hadronic final state is produced more centrally with the advantage to be fully measured in the detector. Also the charm contribution to the inclusive ep scattering cross section rises up to 20% at higher Q^2.

Charm quarks can be tagged by either full reconstruction of D mesons or using variables which are sensitive to the lifetime of heavy flavour hadrons decaying via the weak interaction. This thesis presents a measurement of the D^* production cross section in the range of large photon virtualities $100 < Q^2 < 1000\,\mathrm{GeV}^2$. The data were collected with the H1 detector at HERA during the running period $2004 - 2007$ corresponding to the integrated luminosity of $351\,\mathrm{pb}^{-1}$. The measured cross sections are compared to QCD predictions providing an insight into the dynamics of D^* meson production at high Q^2. The charm contribution, $F_2^{c\bar{c}}$, to the proton structure function, F_2^c, is determined. The measurement has been published by the H1 collaboration [1]. For all D^* measurements the precise knowledge of the track reconstruction efficiency is mandatory. Therefore detailed studies of the track reconstruction efficiency have been performed within this thesis.

The thesis is organized as follows. In the first chapter the theoretical foundations are presented. The second chapter is devoted to the H1 detector with main focus on detector components relevant for this analysis. In chapter 3 the reconstruction of the D^* sample at high Q^2 is presented focussing on two parts namely the reconstruction of the scattered electron and the event kinematics as well as the reconstruction of the D^* mesons. The determination of D^* meson production cross section and its features as well as a detailed description of the systematic errors are covered in chapter 4. In chapter 5 the measured single and double differential D^* meson cross sections are presented and compared to various pQCD predictions. Further the extraction of $F_2^{c\bar{c}}$ based on the double differential cross sections in Q^2 and y is described and the result is compared to various QCD predictions. Tables with the results including a complete listing of all systematic errors for each individual bin of $F_2^{c\bar{c}}$ are given in appendix A. In appendix B the track efficiency studies are presented.

Chapter 1

Theory of Charm Production

In this chapter the basic theoretical concepts of charm production in deep inelastic electron scattering will be introduced. Following the definition of the kinematical variables, the description of the electron proton scattering based on the proton structure functions will be given. Subsequently some fundamental concepts of quantum chromo dynamics (QCD) and of the proton structure will be discussed to provide the basis for the description of the charm production mechanisms. Charm fragmentation and the D^*-mesons properties will be introduced. At the end of the chapter the event generators used in this analysis and the detector simulation will be discussed followed by the description of the program package HVQDIS providing calculations in next to leading order pertubative QCD.

1.1 Kinematics of Electron-Proton Scattering

The interaction between electrons[1] and protons is described in leading order by the exchange of a virtual gauge boson as shown in Fig. 1.1. In the charged current (CC) interaction a $W^{\pm}$ is exchanged with a neutrino produced in the final state. The neutral current (NC) interaction proceeds via the exchange of a γ or Z^0 with an electron produced in the final state. The four momenta of the incoming and outcoming lepton are labeled with $\mathbf{k}$ resp. $\mathbf{k}'$. The four momentum of the incoming proton is denoted with $\mathbf{p}$ and the negative squared four momentum of the exchanged gauge boson is denoted by $-\mathbf{q}^2$, also called virtuality Q^2:

$$Q^2 = -\mathbf{q}^2 = -\left(\mathbf{k} - \mathbf{k}'\right)^2 \tag{1.1}$$

In this thesis only the case of one photon exchange is considered since the additional contributions from the weak interaction are suppressed by $Q^2/M^2_{Z^0,W^{\pm}}$ with

[1] In this thesis "electron" is used to denote both electron and positron.

the $W^{\pm}$ and Z^0 masses being $M_{W^{\pm}} \approx 80\,\mathrm{GeV}$ and $M_{Z^0} \approx 91\,\mathrm{GeV}$, respectively, and therefore negligible for $Q^2 < 1000\,\mathrm{GeV}^2$. In the Breit system [2] the wavelength λ of the virtual photon is related to Q^2 by $\lambda \approx 1/Q$ which means that the resolving power of the photon for probing the proton is increasing with Q^2, e.g. for $Q^2 = 1\,\mathrm{GeV}^2$ the wavelength amounts to $\lambda = 1.2 \cdot 10^{-15}\,\mathrm{m}$ whereas for $Q^2 = 20000\,\mathrm{GeV}^2$ a value of $\lambda = 8.8 \cdot 10^{-18}\,\mathrm{m}$ is reached.

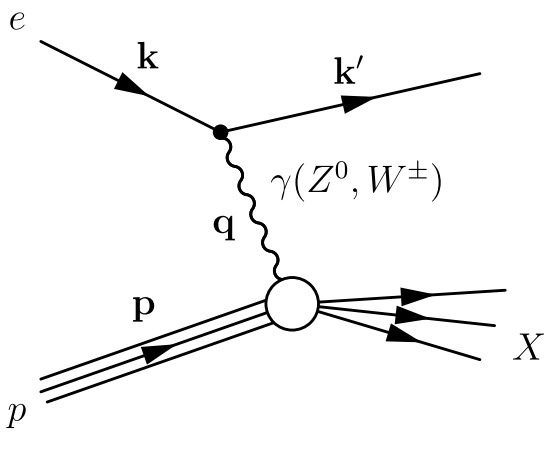

Figure 1.1: Schematic representation of deep inelastic electron-proton scattering

With the four-momenta introduced above one can derive the Lorentz invariant quantities defining the kinematics of the electron-proton scattering process:

- The center of mass energy $\sqrt{s}$ of the proton-electron system

$$s = (\mathbf{k} + \mathbf{p})^2. \tag{1.2}$$

- The Bjorken scaling variable

$$x = \frac{Q^2}{2\mathbf{p} \cdot \mathbf{q}} \tag{1.3}$$

  can be interpreted in the Quark Parton Model (QPM) (see next section) as the fraction of the proton momentum carried by the parton entering the scattering process in the infinite momentum frame of the proton.

- The inelasticity

$$y = \frac{\mathbf{p} \cdot \mathbf{q}}{\mathbf{p} \cdot \mathbf{k}} \tag{1.4}$$

  is the relative energy transfer from the lepton to the hadronic system in the proton rest frame.

- The energy of the boson-proton center of mass system $W_{\gamma p}$ is given by

$$W_{\gamma p}^2 = (\mathbf{q} + \mathbf{p})^2 \tag{1.5}$$

  and is the invariant mass of the hadronic final state X.

Neglecting the electron and proton masses the following approximation holds:

$$Q^2 \approx sxy \tag{1.6}$$

and

$$W_{\gamma p}^2 \approx ys - Q^2 \tag{1.7}$$

In this way, the kinematics of the complete interaction is described by three Lorentz-invariant variables. In the case of HERA with constant beam energies only two variables determine the kinematics of a DIS event.

Two kinematic regions are distinguished: $Q^2 \approx 0\,\mathrm{GeV}^2$ is called (quasi-real) photoproduction; $Q^2 \geq 2\,\mathrm{GeV}^2$ corresponds to deep inelastic scattering (DIS). This thesis reports for the first time an analysis of D^* production in DIS at H1 at high photon virtualities $Q^2 > 100\,\mathrm{GeV}^2$

1.2 Deep Inelastic Scattering and QCD

1.2.1 The Structure of the Proton

Neglecting contributions from Z^0 exchange the differential cross section for the process $ep \to eX$ in the Born approximation in QED can be written in terms of the structure functions $F_1(x, Q^2)$ and $F_2(x, Q^2)$:

$$\frac{d^2\sigma_{NC}^{ep}}{dxdQ^2} = \frac{4\pi\alpha_{em}^2}{xQ^4}\left(xy^2F_1(x, Q^2) + (1-y)F_2(x, Q^2)\right) \tag{1.8}$$

where α_{em} is the electromagnetic coupling constant. The differential cross section can also be written in terms of two different structure functions $F_2(x, Q^2)$ and $F_L(x, Q^2)$:

$$\frac{d^2\sigma_{NC}^{ep}}{dxdQ^2} = \frac{4\pi\alpha_{em}^2}{xQ^4}\left(\left(1 - y + \frac{y^2}{2}\right)F_2(x, Q^2) - \frac{y^2}{2}F_L(x, Q^2)\right) \tag{1.9}$$

where $F_L(x, Q^2)$ is defined as:

$$F_L(x, Q^2) = F_2(x, Q^2) - 2xF_1(x, Q^2). \tag{1.10}$$

The structure functions are related to the virtual photon-proton cross sections $\sigma_{\perp}^{\gamma p}$ and $\sigma_{\parallel}^{\gamma p}$, corresponding to a transversely and longitudinally polarised photon, respectively:

$$F_L(x,Q^2) = \frac{Q^2}{4\pi^2\alpha_{em}}\sigma_{\parallel}^{\gamma p} \tag{1.11}$$

$$2xF_1(x,Q^2) = \frac{Q^2}{4\pi^2\alpha_{em}}\sigma_{\perp}^{\gamma p} \tag{1.12}$$

$$F_2(x,Q^2) = \frac{Q^2}{4\pi^2\alpha_{em}}\left(\sigma_{\perp}^{\gamma p} + \sigma_{\parallel}^{\gamma p}\right) = \frac{Q^2}{4\pi^2\alpha_{em}}\sigma^{\gamma p}. \tag{1.13}$$

In the following those structure functions are discussed in detail.

1.2.2 The Quark Parton Model

The proton structure is most easily discussed in the simple quark parton model, where pointlike and massless quarks are treated as quasi free objects within the proton. The scattering of electrons on protons can then be described by the scattering on the corresponding partons as shown in Fig. 1.2, where the momentum fraction of the quark with respect to the proton is given by the Bjorken variable x defined above. Since no interaction between the partons in the proton is considered, the mo-

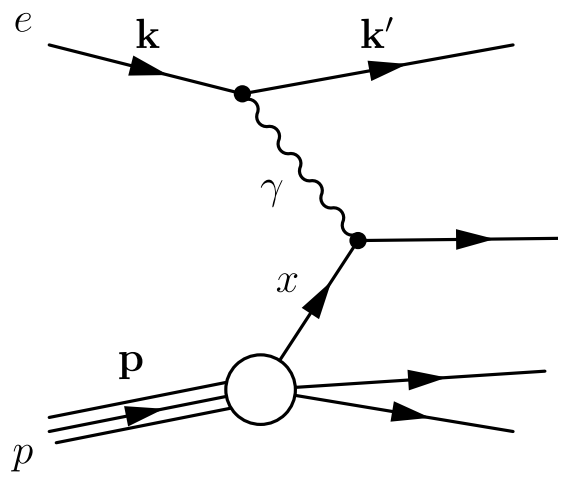

Figure 1.2: Feynman graph of deep inelastic scattering on a quark of the incoming proton in the Quark Parton Model (QPM)

mentum fraction for each parton is not time dependent. In that case, as predicted by Bjorken in the high Q^2 limit [3], the structure function F_2 is scale invariant i.e.

depends only on x and not on Q^2. In terms of the quark and antiquark distribution functions $q_i(x)$ and $\bar{q}_i(x)$ the structure function F_2 is written as:

$$F_2(x) = \sum_{i=1}^{n_f} e_i^2 x \left(q_i(x) + \bar{q}_i(x)\right), \tag{1.14}$$

where the sum $i = 1, ..., n_f$ runs over all active quark flavours ordered by increasing quark masses, and e_i denotes the electric charge of the quark of type i. Since in the QPM the virtual photon is exchanged between the electron and an on-shell massless spin 1/2 quark, the cross section for longitudinally polarized photons is vanishing ($\sigma_{\parallel}^{\gamma p} = 0$) as shown in [4]. This leads according to Eq. 1.11 to the Callan-Gross relationship:

$$F_L(x) = F_2(x) - 2xF_1(x) = 0. \tag{1.15}$$

A first extension to the simple QPM allows for bound quarks particular in DIS by introducing quark distribution functions $q_i(x, Q^2)$ and $\bar{q}_i(x, Q^2)$ which depend also on Q^2. In leading order F_2 keeps the same form as in the QPM:

$$F_2(x, Q^2) = \sum_{i=1}^{n_f} e_i^2 x \left(q_i(x, Q^2) + \bar{q}_i(x, Q^2)\right), \tag{1.16}$$

The Q^2-dependence of the structure function F_2 can be illustrated as follows: with rising Q^2 the electron probe can distinguish smaller fluctuations with lower fractional momentum x in the proton. The lower x the earlier and stronger the Q^2 dependence appears. Such behavior (scaling violations) was observed at HERA as described in Sec. 1.2.5.

1.2.3 Quantum Chromodynamics

The modern understanding of the hadronic substructure and strong interactions is based on quantum chromodynamics (QCD) which is a local non-Abelian gauge theory, based on the $SU(3)$ gauge group. The main aspects of the QCD are described in the following.

The static quark model was introduced to explain the spectrum of the mesons and baryons [5]. To be consistent with the Pauli-principle for spin 1/2 particles an additional degree of freedom was needed, called color. Each quark or anti-quark can be in one of three basic states which are labeled red $= r$, green $= g$ and blue $= b$ in the case of quarks and $\bar{r}$, $\bar{g}$ and $\bar{b}$ in the case of anti-quarks. For mesons consisting of a quark and an anti-quark as well as baryons consisting of three quarks (three anti-quarks) the color part of the state must be totally antisymmetric, they are color singlets. The colors are additive quantum numbers. Due to the antisymmetry the

color neutral state called white $= w$ is achieved by $r + g + b = w$, $\bar{r} + \bar{g} + \bar{b} = w$ and $c + \bar{c} = w$, $c \in \{r, g, b\}$ motivating the association to colors. There are several experimental evidences that the number of colors is exactly three. [5].

QCD is based on local gauge transformations concerning the color states within the symmetry group $SU(3)$. The requirement of gauge invariance leads to the existence of eight fields, which couple to the color charges and can change the color of the quarks. The eight different field-quanta are called gluons. They are massless and carry color charges due to the non-Abelian nature of QCD. The eight gluons are distinguished by the colors they carry occuring in the combination color/anti-color. Since the gluons carry color charge, their self-interaction is allowed.

According to experimental results all physical observable states consisting of quarks and gluons are colorless (w). Therefore the quarks and gluons do not appear as free particles but only in colour singlet hadronic bound states. This behavior is known as "color-confinement".

1.2.4 Renormalisation and the Running Coupling Constant

As mentioned above in QCD the interaction between quarks is mediated by gluons. In the lowest order one gluon is exchanged with four momentum transfer Q^2 in the propagator. The matrixelement describing this scattering process is proportional to the strong coupling constant $\alpha_s = g_s^2/4\pi$ defined in analogy with the fine structure constant in QED. The coupling parameter at the vertex is denoted by g_s. The strong coupling constant, α_s, in QCD is significantly larger than the electromagnetic one and therefore higher order contributions in perturbative quantum chromodynamics (pQCD), where the transition matrix element is evoluted in series of α_s, cannot be neglected anymore. Higher order contributions arise from loop diagrams as shown in Fig. 1.3 (one loop) and can be absorbed in an effective coupling constant. Within this treatment α_s is expected to vary with the momentum transfer squared Q^2 (running coupling constant) as explained in the following.

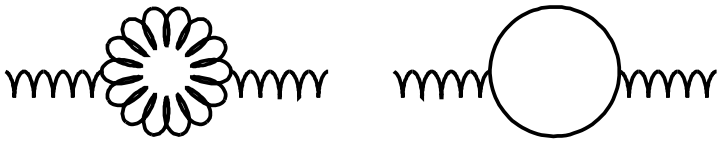

Figure 1.3: Loop diagramms

When evaluating loop diagrams according to the Feynman rules one independent internal momentum p_L per loop occurs which has to be integrated leading to

divergences for $p_L \to \infty$. These divergences are therefore called ultraviolet loop divergencies and are removed by a renormalisation procedure introducing a renormalisation scale μ^2 at which these divergencies are subtracted out. This leads to a dependence of the renormalised coupling constant α_s on the renormalisation scale μ^2 [6].

Predictions of physical observables $R(Q^2/\mu^2, \alpha_s(\mu^2))$ up to all orders of perturbation theory should not depend on the renormalisation scale. Therefore any explicit dependence of R on μ^2 should be cancelled by the dependence of α_s on μ^2 as follows:

$$\mu^2 \frac{\partial R}{\partial \mu^2} + \mu^2 \frac{\partial \alpha_s}{\partial \mu^2} \frac{\partial R}{\partial \alpha_s} = 0. \tag{1.17}$$

If physical quantities are computed to a fixed order, the dependencies of the observables on the scale will remain due to missing higher order diagrams. This scale dependence can be estimated as part of the theoretical uncertainty for an observable. The choice of the renormalisation scale is free. In most calculations, it is set naturally to $\mu^2 = Q^2$.

The running of the coupling constant α_s is determined by the renormalisation group equation:

$$Q^2 \frac{\partial \alpha_s}{\partial Q^2} = \alpha_s \beta(\alpha_s) = -\beta_0 \frac{\alpha_s^2}{4\pi} - \beta_1 \frac{\alpha_s^3}{16\pi^2} + ... \tag{1.18}$$

with

$$\beta_0 = 11 - 2/3\, n_f \quad , \quad \beta_1 = 102 - 38/3\, n_f. \tag{1.19}$$

Here β_0 and β_1 are the first coefficients occuring in the expansion due to one loop and two loop contributions and n_f denotes the number of active flavours in the nucleon, i.e. the number of quark flavours with mass smaller than μ. When solving the differential equation Eq. 1.18 for α_s an integration constant is introduced. This constant is determined from experiment and is chosen to be the value of α_s at a fixed reference scale. The preferred reference scale is the Z_0 boson mass m_Z. At leading order the solution reads:

$$\alpha_s(Q^2) = \frac{\alpha_s(m_Z^2)}{1 - \beta_0 \frac{\alpha_s(m_Z^2)}{4\pi} \ln\left(\frac{Q^2}{m_Z^2}\right)}. \tag{1.20}$$

After introducing the QCD constant Λ_{QCD} which in LO is given by:

$$\Lambda_{QCD}^{(n_f)\,2} = m_Z^2 \exp\left(\frac{4\pi}{\beta_0 \alpha_s(m_Z^2)}\right), \tag{1.21}$$

the equation 1.20 can be written as:

$$\alpha_s(Q^2) = \frac{4\pi}{\beta_0 \ln(Q^2/\Lambda_{QCD}^{(n_f)\,2})} \tag{1.22}$$

At small distances or large energy scales ($Q^2 \to \infty$), the coupling between quarks and gluons becomes small, $\alpha_s \to 0$, and the quarks inside the proton can be treated as quasi free particles. This property of QCD is referred to as "asymptotic freedom". However this situation is not described by the quark parton model due to gluon radiation where a quark in the proton can acquire large transverse momentum. For $Q^2 \to \Lambda_{QCD}^{(n_f)^2}$, the coupling diverges, reflecting the confinement of quarks and gluons inside hadrons. However, confinement is not yet completely understood since the increase of the coupling constant prohibits the use of perturbation theory in the region of small renormalisation scale.

The logarithmic increase of the strong coupling constant with decreasing momentum transfer leading to the confinement is a direct consequence of the gluon self-coupling (gluon loops) and therefore a specific feature of QCD not occuring in QED. The strong coupling constant is only in the presence of large scales small enough to make predictions with perturbative QCD (pQCD). Therefore the production of heavy quarks in DIS is an ideal process to study pQCD since due to the high masses $m_{c,b,t}$ always a large scale exists in the scattering process. In general one can have additional hard scales like the virtuality Q^2 or the transverse momentum of the quarks rendering predictions more difficult (multi scale problem [7]).

1.2.5 Scaling Violations in QCD

At HERA, the scaling violations, namely the dependence of the proton structure function F_2 on Q^2 were precisely measured. In Fig. 1.4 the reduced cross section σ_r is shown as a function of Q^2 for various fixed values of x as measured by the H1 and ZEUS experiments at HERA and fixed target experiments [8]. In most of the kinematic range the relation $\sigma_r \approx F_2$ holds to a very good approximation [9]. The scaling behavior, expected in the QPM, is observed only for values of Bjorken $x \approx 0.13$ whereas in all other regions of x the structure function F_2 depends on Q^2.

The rise of the proton structure function with increasing Q^2 at low x and the decrease at high x arise from the gluon interactions in QCD: the quarks inside the proton continuously emit gluons, which may then fluctuate into virtual quark and anti-quark pairs. These virtual quark and anti-quark pairs called "*sea quarks*" are distinguished from the original quark content of the proton in the static QPM namely the "*valence quarks*".

The scaling violations due to the contribution of virtual quarks to the ep scattering cross section can be interpreted in such a way, that with increasing Q^2 the photon emitted by the electron is more likely to find the proton in a state in which one of the valence quarks has radiated one or more gluons and is surrounded by a cloud of virtual quark and anti-quark pairs. The photon may then scatter off one of the sea quarks, which typically carry only a small fraction x of the momentum of the

proton. This explains why F_2 increases with Q^2 at $x < 0.13$ when the photon starts to resolve sea quarks. If the photon, however, scatters off the valence quark that has radiated off the gluons, the struck quark carries on average a smaller fraction x of the proton's momentum than without gluon emission. The contribution of the valence quarks are therefore shifted to lower x with increasing Q^2. This illustrates the scaling violation of F_2 in the opposite direction at $x > 0.13$.

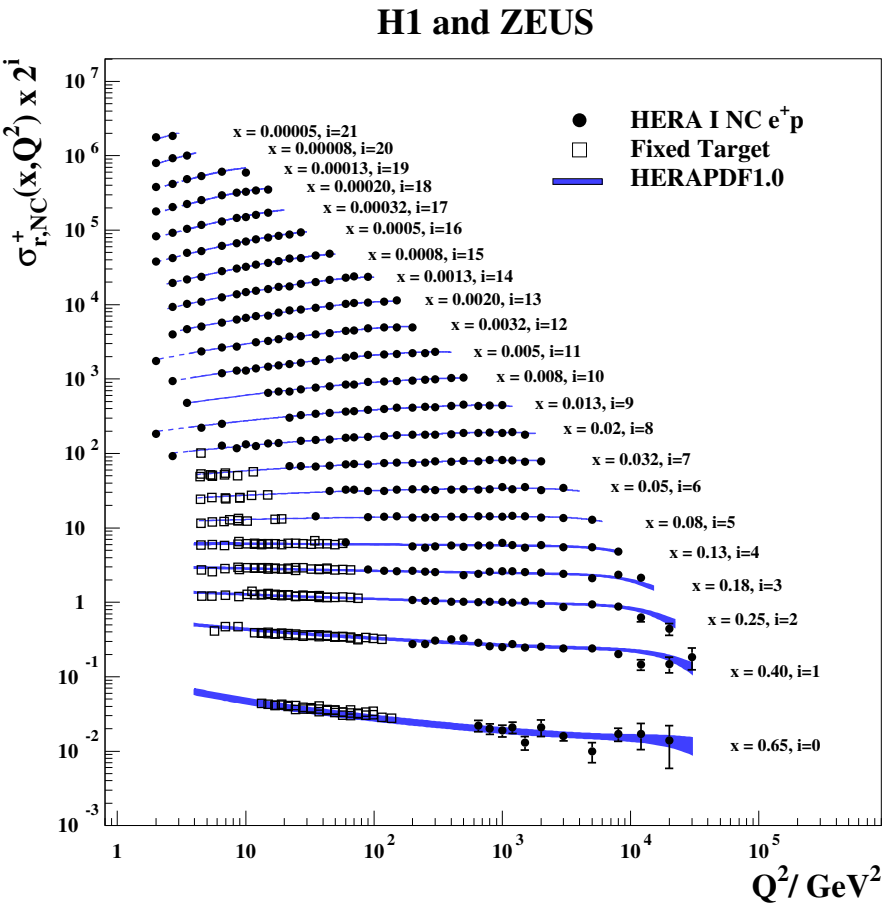

Figure 1.4: Measurement of the NC e^+p reduced cross section $\sigma_r^+(x, Q^2)$ as a function of Q^2 at fixed x. Shown are the combination of H1 and ZEUS inclusive measurements from the HERAI period (filled circles) and the corresponding Standard Model expectation determined from the recent HERA PDF fit HERAPDF1.0 [8]. Further shown results from fixed target experiments (open squares).

1.2.6 QCD Factorisation

The treatment of the ep-scattering process in pQCD leads to additional divergencies due to gluon radiation where large divergent logarithms in the perturbation series occur in two different regions. The case where the emitted gluon is moving in the direction of the outgoing quark with vanishing transverse momentum is referred to as collinear divergence, while soft divergence refers to the case where the emitted gluon is soft, i.e. has low energy. Both types of divergences are caused by small momenta why they are also referred to as infrared divergencies. Inspite of these divergencies it is possible to provide theoretical predictions within pQCD. They are renormalised in analogy to the ultraviolet divergences described above, introducing an additional factorisation scale μ_F^2. For momentum transfers $Q^2 > \mu_F^2$, α_s is taken to be small and perturbation theory is applicable. This is the regime of short range, high momentum transfer ("hard") interactions. Processes belonging to the "soft" regime with $Q^2 < \mu_F^2$ including the infrared divergencies are absorbed in the renormalised parton distribution functions. These functions depend on the factorisation scale μ_F^2. The separation of "hard" and "soft" scale processes is called factorisation [6]. Within the factorisation ansatz the structure function F_2 can be written as a convolution of a hard interaction part C^i and the parton density functions f_i with $f_i = q_i$, $i \leq n_f$ for quarks and $f_{n_f+1} = g$ for gluons:

$$F_2(x, Q^2) = \sum_{i=1}^{n_f+1} \int_x^1 C^i(x/x', Q^2/\mu_R^2, \mu_F^2, \alpha_s)\, f_i(x', \mu_R^2, \mu_F^2, \alpha_s) dx'. \tag{1.23}$$

where μ_R is the renormalisation scale described above and n_f the number of active quark flavours. The functions C^i describe how a parton i with momentum fraction x with respect to the proton evolves from pQCD processes via the exchange of virtual partons out of the initial parton with fractional proton momentum x'. Nowadays most of the pQCD calculations are performed at the leading order (LO) or at the next to leading order (NLO) in α_s. All non calculated higher orders are absorbed in the parton density functions f_i.

For the determination of the f_i in Eq. 1.23 experimental input is needed (see next section). Nevertheless, the extracted parton density functions (PDFs) are completely independent of the underlying process and can therefore be measured in one process and applied to another. As an example this universality property means that the PDFs of the proton measured at HERA should be able to describe any other process involving protons, be it ep interactions at HERA, $p\bar{p}$ interations at the Tevatron, or pp interactions at the LHC.

1.2.7 Parton Evolution Models

The non perturbative part in the QCD factorsation ansatz according to Eq. 1.23 contained in the parton density functions f_i can be further restricted by QCD. Applying perturbation theory the evolution of the parton densities of quarks $q_i(x, Q^2)$ and gluons $g(x, Q^2)$ from a scale Q_0^2 to higher Q^2 can be predicted. This reduces the experimental input since the parton densities are measured only at a certain value of Q^2. The scale Q_0^2, with the requirement $\alpha_s(Q_0^2) \ll 1$, can be considered as the factorisation scale. There are several schemes for the treatment of the evolution which are valid in different regions of the (x, Q^2) space respectively.

The DGLAP Approach

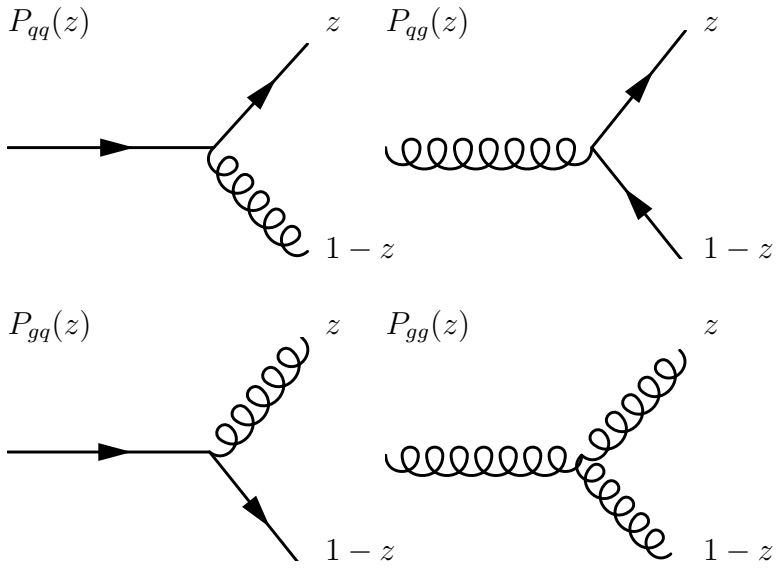

Figure 1.5: Feynman diagrams for the processes for calculating the splitting functions $P_{qq}(z)$, $P_{qg}(z)$, $P_{gq}(z)$ and $P_{gg}(z)$

In the DGLAP[2] formalism [10] two equations govern the evolution in LO in α_s:

$$\frac{\partial q_i(x,Q^2)}{\partial \ln Q^2} = \frac{\alpha_s(Q^2)}{2\pi} \int_x^1 \frac{dx'}{x'} \left[P_{qq}\left(\frac{x}{x'}\right) q_i(x',Q^2) + P_{qg}\left(\frac{x}{x'}\right) g(x',Q^2) \right], \quad (1.24)$$

$$\frac{\partial g(x,Q^2)}{\partial \ln Q^2} = \frac{\alpha_s(Q^2)}{2\pi} \int_x^1 \frac{dx'}{x'} \left[\sum_{i=1}^{n_f} P_{gq}\left(\frac{x}{x'}\right) q_i(x',Q^2) + P_{gg}\left(\frac{x}{x'}\right) g(x',Q^2) \right]. \quad (1.25)$$

[2]Dokshitzer, Gribov, Lipatov, Altarelli, Parisi

The splitting functions $P_{ab}(z)$ describe the probability that a parton b emits a parton a carrying away a fraction z of its longitudinal momentum. The corresponding Feynman graphs are shown in Fig. 1.5.

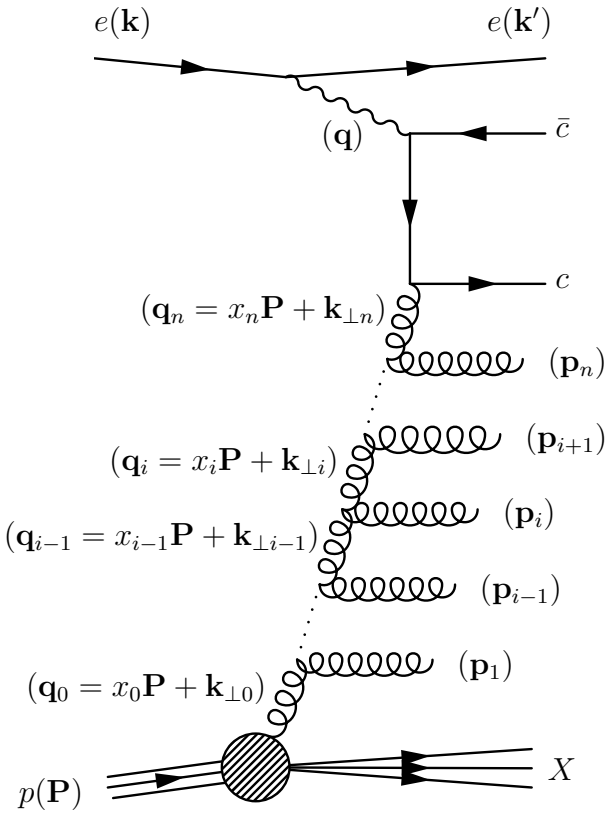

Figure 1.6: Emissions of gluons within the parton evolution in the so called gluon ladder. The emitted gluons have the three momenta $\mathbf{p}_i$ and the intermediary partons the three momenta $\mathbf{q}_i$ divided in the longitudinal component $x_i\mathbf{P}$ and the transverse momentum $\mathbf{k}_{\perp i}$.

In leading order the DGLAP ansatz is equivalent to the resummation of gluon ladder diagrams shown in Fig. 1.6 whose rungs are strongly ordered in transverse momenta [11]:

$$Q^2 \gg k^2_{\perp n} \gg k^2_{\perp n-1} \gg ... \gg k^2_{\perp 1} \gg k^2_{\perp 0}, \tag{1.26}$$

with an opposite soft ordering in the longitudinal momenta:

$$x < x_n < x_{n-1} < ... < x_1 < x_0. \tag{1.27}$$

The DGLAP ansatz is only valid at sufficiently high x. It fails when for very small x the splitting function P_{gg} becomes the dominant term in comparison to $\ln(Q^2)$. The condition for the so called collinear leading logarithmic approximation (LLA) is:

$$\alpha_s(Q^2) \ln \frac{1}{x} \ll \alpha_s(Q^2) \ln \left(\frac{Q^2}{Q_0^2} \right) < 1. \tag{1.28}$$

The BFKL Approach

In the case of very small values of x and small values of Q^2 the BFKL[3] formalism [12, 13] is applicable. There the resummation of $(\alpha_s \ln(1/x))^n$ terms is done independent of Q^2. The condition for this ansatz is:

$$\alpha_s(Q^2) \ln \frac{Q^2}{Q_0^2} \ll \alpha_s(Q^2) \ln \frac{1}{x} \ll 1. \tag{1.29}$$

The gluon ladders are considered with strong ordering in longitudinal momenta and soft ordering in transverse momenta:

$$Q^2/c^2 > k_{\perp n}^2 > k_{\perp n-1}^2 > ... > k_{\perp 1}^2 > k_{\perp 0}^2, \tag{1.30}$$

and

$$x \ll x_n \ll x_{n-1} \ll ... \ll x_1 \ll x_0. \tag{1.31}$$

This results in the BFKL evolution equation [12, 13] describing the evolution in x of the unintegrated gluon distribution $\mathcal{F}(x, k_\perp^2, Q_0^2)$. This distribution depends also on the transverse momentum of the gluon. The reason for this is that $k_{\perp 0}^2$ at the beginning of the ladder (Fig. 1.6) has finite values due to the only soft ordering according eq. 1.30 in contrast to the DGLAP ansatz. The unintegrated gluon density is related to the conventional DGLAP gluon distribution via:

$$xg(x, Q^2) = \int_0^{Q^2} \mathcal{F}(x, k_\perp^2, Q_0^2) \frac{dk_\perp^2}{k_\perp^2}. \tag{1.32}$$

The CCFM Approach

In general large $\ln(Q^2)$ and $\ln(1/x)$ terms can occur simultanously. Then both conditions of equations 1.28 and 1.29 for the DGLAP and BFKL approach do not hold. The divergencies in the corresponding logarithmic terms are taken into account by a different ansatz called double leading logarithmic approximation (DLLA). A general threatment of the gluon ladder within the DLLA leads to the CCFM[4] evolution

[3] Balitsky,Fadin,Kuraev,Lipatov

[4] Catani, Ciafaloni, Fiorani, Marchesini

equation [14–17]. This evolution scheme is based on the requirement that the emitted gluons are ordered according to their angles with respect to the incoming proton. The angles increase following the parton ladder in direction of the hard process (cf. Fig. 1.6).

Due to the consideration of divergencies in both logarithms mentioned above the CCFM formalism remains valid in the entire (x, Q^2) plane. The CCFM model contains the BFKL and DGLAP models as special cases: It is equivalent to DGLAP for large Q^2 and moderate x and equivalent to BFKL in case of small x and moderate Q^2. Therefore one can assume that in general the parton evolution is better characterised by the CCFM evolution equation than by DGLAP especially at small x: F_2 measurements are well described by the CCFM model [18, 19]. Furthermore by fitting the F_2 data [20] one obtains a solution of the CCFM evolution equation which provides a significantly better description of the cross section for the production of forward jets than the DGLAP scheme [20].

1.2.8 Extraction of the Parton Densities

When parton densities are extracted by a QCD fit to experimental data the separate contributions from valence-quarks, sea-quarks and gluons are appropriately parametrised using power laws or polynomial functions in the fractional momentum, respectively.

Concerning the treatment of the data sets there are currently two distinct approaches. The MRST [21] and CTEQ [22] collaborations perform a global fit to a data set which includes deep inelastic scattering, Drell-Yan pair production in fixed target and collider experiments, and Tevatron inclusive jet cross sections. This approach benefits from a variety of data with different sensitivities to the three contributions, respectively. A disadvantage of this approach however is that an inconsistency of a particular data set may influence the quality of the global fit. Furthermore going beyond the next-to-leading order within this framework is difficult since very few partonic processes are currently treatable with NNLO pQCD.

A different approach was initiated by Alekhin [23] where the data used are restricted to deep inelastic scattering. The pQCD calculations needed for the fit, especially the DGLAP evolution, extends up to NNLO. The disadvantage of this approach is that the DIS data are only sensitive to certain combinations of PDFs meaning that not every parton distribution function can be reliably constrained. This leads to large, approximately 20%, errors on sea quark and gluon distributions at relatively large values of the Bjorken variable x, $x > 0.1$ [24].

The recent extraction of the parton densities of the proton within the H1 and ZEUS collaboration is done by performing a NLO QCD fit to the inclusive NC and CC data where the results of both the H1 and ZEUS analyses for the HERAI period have been combined to reduce the systematic uncertainties [8]. The parton densities

are parameterised at an initial scale $Q_0^2 = 4\,\mathrm{GeV}^2$. The parton densities are then evolved in Q^2 using the NLO DGLAP equations and fitted to the experimental data. The results of the recent HERA PDF fit HERAPDF1.0 are shown in Fig. 1.7 at $Q^2 = 10\,\mathrm{GeV}^2$. The gluon and sea quark densities are seen to dominate at low x whereas the valence quarks dominate at high x ($x > 0.2$). The bands represent estimates of the experimental and theoretical uncertainties of the fit.

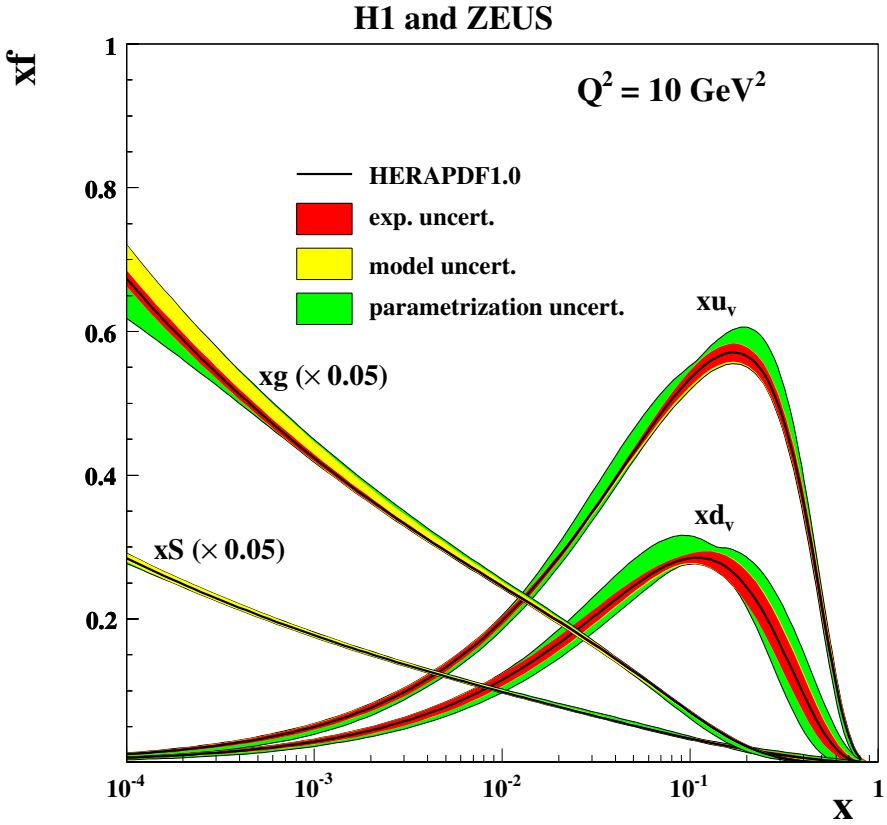

Figure 1.7: Extracted parton density functions from the recent HERA PDF fit HERAPDF1.0 [8] for the valence quarks xu_v, the sea quarks xS and the gluons xg. The distributions are shown at $Q^2 = 10\,\mathrm{GeV}^2$. The bands represent estimates of the experimental and theoretical uncertainties. Gluon and seaquark distributions are scaled down by 0.05.

The main problem in extracting the parton densities by the approaches described above are the parametrisation assumptions made in the fit procedure. Therefore the results concerning one distribution, for example the gluons, are dependent on the parametrisation of the others. Study of boson-gluon process provides a direct handle on the gluon density in the proton because of a directly involved gluon distribution.

Also, using the charm contribution $F_2^{c\bar{c}}$ to the proton structure function F_2 in the PDF fit together with the inclusive cross-section data allows to constrain the charm quark mass which is one of the important fit parameters.

1.3 Charm in Electron-Proton Scattering

In this section the main aspects of charm production in *ep*-scattering at HERA are presented. Charm quarks are produced in *ep*-scattering at HERA predominantly in the boson-gluon fusion process (BGF). Therefore, charm tagging provides the possibility of a direct access to the gluon density in the proton. Experimentally charmed hadrons can only be observed via their decay particles. This section is organised as follows: first the production of charm quarks and their transition to charmed hadrons and finally the decay of charmed hadrons is described.

1.3.1 Charm Production

For the description of charm production in *ep*-scattering three different methods exists in the literature which differ by their treatment of the charm quark mass [25]:

In the **massive approach** the light quarks (u, d, s) are active flavours in the proton whereas the charm quark is considered as massive and is produced at the perturbative level in QCD. Within this approach the dominant pQCD process is the boson-gluon fusion (BGF) where the virtual photon interacts with a gluon in the proton via a charm-anti-charm quark pair (see Fig. 1.8a). The proton structure function F_2 is represented as follows:

$$F_2(x, Q^2) = \sum_{i=1}^{n_f=3} e_i^2 x \left(q_i(x, Q^2) + \bar{q}_i(x, Q^2)\right) + F_2^c, \tag{1.33}$$

where at the LO in α_s:

$$F_2^c = \frac{Q^2 \alpha_s}{4\pi m_c^2 c^4} \int_{x_{min}}^{1} \frac{dx'}{x'} e_c^2 g(x_g, \mu^2) C_{2,g}^0 \left(\frac{x}{x'}, Q^2, m_c^2, \mu^2\right). \tag{1.34}$$

The charm contribution F_2^c to the proton structure function F_2 factorises into the gluon density $g(x_g, \mu^2)$ and the hard interaction part contained in the coefficient function $C_{2,g}^0$ corresponding to the cross section of the BGF process in the photon gluon system. The lower boundary of the integration x_{min} is given by $x(Q^2 + 4m_c^2)/Q^2$. The massive approach, valid for $Q^2 \approx m_c^2$, breaks down for $Q^2 \gg m_c^2$ due to divergencies in terms of $\ln(Q^2/m_c^2)$. Usually the massive approach is treated in the fixed flavour number scheme (FFNS).

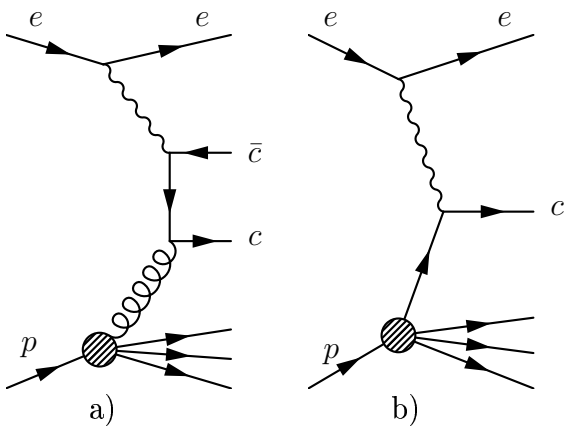

Figure 1.8: Feynman diagrams for the charm production mechanisms: direct boson gluon fusion (a) and sea charm from proton (b).

In the **massless approach** the charm quark is considered as an active flavour in the proton with the charm mass neglected. Charm is now described by a parton density and the ep scattering process is in lowest order characterised by a direct coupling of the photon to the charm quark in the sea (see Fig. 1.8b). This direct QED coupling to the charm in the proton can be expressed by the following decomposition of the proton structure function [25]:

$$F_2(x,Q^2) = \sum_{i=1}^{n_f=4} e_i^2 x \left(q_i(x,Q^2) + \bar{q}_i(x,Q^2)\right) = \sum_{i=1}^{n_f=3} e_i^2 x \left(q_i(x,Q^2) + \bar{q}_i(x,Q^2)\right) + F_2^c, \tag{1.35}$$

with $q_{n_f=4} = c$. This approach can be used either in the fixed flavour number scheme or in the variable flavour number scheme (VFNS). Within this approach F_2^c is not directly connected to the gluon density in the proton.

A combination of these both approaches leads to the **generalized mass variable flavour number scheme (GMVFNS) approach** [26] which consists of a sequence of n_f-FFNS calculations, each in its region of validity, for flavour number $n_f = 3, 4, ...$ They are matched at a certain scale which is usually set to the heavy quark mass.

A completely different mechanism for charm production is **intrinsic charm production** [27, 28] which explains some special features of charm production at large x. In this approach a $c\bar{c}$-pair is considered as a non pertubative component in the proton bound state. In this model the Fock space decomposition of the proton wave function contains a non-negligible $uudc\bar{c}$ component.

In this analysis the measured cross sections for charm production in the kine-

matic range $100\,\mathrm{GeV}^2 < Q^2 < 1000\,\mathrm{GeV}^2$ are compared with calculations within the massive scheme (LO and NLO) as well as the massless scheme (NLO). A measurement allowing a distinction between the two production mechanisms at lower Q^2 was published by the H1 experiment [29]. It was shown that at least for $Q^2 < 100\,\mathrm{GeV}^2$ a fraction of more than 5% charm from the proton sea can be excluded at a 95% confidence level. Within the analysis presented here it could be shown that also at much higher Q^2 the massive scheme (in NLO) provides a good description of the data whereas the calculations in the massless scheme fail.

1.3.2 Charm Fragmentation

The transition of a charm quark into a charmed hadron is, however, not calculable within the framework of pQCD and is thus usually described by phenomenological models. Within this fragmentation process two independent aspects have to be checked. The first aspect involves the probabilities of a quark to hadronize into various types of colorless objects. The fraction $f(c \to D^*)$ of charm quarks fragmenting into D^* mesons is taken as $f(c \to D^*) = 23.8 \pm 0.8\%$ [30] from the combination of measurements in e^+e^- experiments. The second aspect deals with the probability density distribution $D_Q^H(z)$, where z is the energy fraction which is transferred due to fragmentation from the parent parton Q to the daughter hadron H (fragmentation function). Similar to the QCD description of the structure functions F_2 discussed above, the fragmentation process can be factorised into a hard interaction part treatable within pQCD and a soft non-perturbative part. The perturbative part is described via parton showers, where the virtual quarks partipicipating in the hard matrix element emit particles until they become on-shell. The calculations use similar splitting functions as for the parton evolution. The non-perturbative part, called hadronisation, corresponds to the transition of the on-shell partons to bound hadron states.

Various models exist which describe the fragmentation. The Monte-Carlo generators used in this analysis have implemented the Lund-String-Model [31–33] to describe the hadronisation of the light quarks u,d und s. The basic idea of this model is described in the following: when both particles of a $q\bar{q}$ pair are moving away after the interaction, the resulting color field is compressed into a narrow tube, the so-called string. If sufficient energy is stored in the string it breaks and a new $q\bar{q}$ is produced. Radiated gluons cause kinks in the strings, which influence the angular distribution of the hadrons produced.

Beside this model further approaches are on the market like the cluster-model [34, 35], Bowler fragmentation [32], Peterson fragmentation [36] and the Kartvelishvili parametrisation [37]. The Monte-Carlo Generators RAPGAP and CASCADE used in this analysis implement the Bowler model whereas in HVQDIS, providing NLO calculations for charm production, charm quarks are fragmented according to the

Kartvelishvili approach. This models are described in the following.

Within the Kartvelishvili approach the explicit form of the heavy quark (Q) fragmentation function is determined on the basis of the reciprocity between the fragmentation function $D_Q^H(z)$ and the heavy quark density $f_H^Q(z)$ in the hadron H, which can be calculated using the Kuti-Weisskopf model [38]. Assuming the validity of the "reciprocity relation" $D_Q^H(z) = f_H^Q(z)$ at $z \sim 1$, and the universality of the quark-antiquark sea, one obtains the fragmentation function:

$$D_Q^H(z) = N z^\alpha (1-z), \tag{1.36}$$

where α is the fragmentation parameter. According to [37], the value of this parameter shold be equal to 3 for charm quarks and 9 for beauty quarks.

The parametrisation of the fragmentation of heavy quarks by the Bowler approach is given by

$$D_Q^H(z) = N \frac{1}{z^{1+bm_Q^2}} (1-z)^\alpha \exp\left(\frac{bm_\perp^2}{z}\right), \tag{1.37}$$

where a and b are free parameters which have to be determined experimentally. The transverse mass $m_\perp$ of a heavy quark with transverse momentum $p_\perp$ is defined by $m_\perp = \sqrt{p_\perp^2 + m_Q^2}$. Considering the transverse mass should lead to better description of the fragmentation in comparison to other models [39].

The charm fragmentation function has been measured at H1 [40] using inclusive D^* meson production. The Kartvelishvili fragmentation function according Eq. 1.36 is used. The parameter values corresponding to the programs used in the present analysis have been measured there and are used here. They depend on the centre of mass energy squared of the hard process, $\hat{s}$.

1.3.3 Properties of the D^* Meson

The charged D^{*+} (D^{*-}) meson with quark content $c\bar{d}$ ($\bar{c}d$) is the lowest excited state of the charged D meson. With its quantum numbers $I(J^P) = 1/2(1^-)$ (I: isospin, J: angular momentum and P: parity) the $D^{*\pm}$ meson belongs to the vector mesons. The mass amounts to $2010.0 \pm 0.4\,\mathrm{MeV}$ [41] which differs from the mass of the D^0 meson with $1864.5 \pm 0.4\,\mathrm{MeV}$ by approximately one pion mass.

The D^* meson decays under emission of a neutral pion or photon in a $D^\pm$ or via emission of a charged pion in a D^0. The total decay width Γ of the D^* amounts to be $\Gamma = 96 \pm 22\,\mathrm{keV}$. The decay channels with their branching ratios are summarized in Tab. 1.1. In this analysis only the decay of the D^* in $D^0\pi^\pm$ is used since the pion is charged. Due to the small mass difference between the D^* and the D^0 meson the pion is produced in the decay with a very small momentum in the D^* rest frame. It is therefore denoted "slow pion" (π_{slow}).

decay channel	fraction
$D^0\pi^\pm$	$(67.7 \pm 0.5)\%$
$D^\pm\pi^0$	$(30.7 \pm 0.5)\%$
$D^\pm\gamma$	$(1.6 \pm 0.4)\%$

Table 1.1: Decay channels of the charged D^* meson according to [41].

The D^0 decays via the weak interaction with a mean lifetime of $\tau = (410.1 \pm 1.5) \cdot 10^{-15}$s. The decay channels relevant for this analysis together with their branching fractions are listed in table 1.2. For the charm analysis the decay of the D^0 meson in the two charged particles $K^\pm\pi^\mp$ is used. Therefore the complete decay chain of the D^* meson selected has only charged particles in the final state, which can be detected with track detectors. For the reconstruction of D^* mesons a strong background suppression is achieved due to the small phase space of the π_{slow}. Due to its advantages this decay chain is called the "golden channel". When selecting the "golden channel" there are however certain contributions from the other decay channels listed in Tab. 1.2, so-called reflections, which have to be taken into account.

decay channel	fraction
$K^\pm\pi^\mp$	$(3.80 \pm 0.07)\%$
$K^\pm K^\mp$	$(3.84 \pm 0.10) \cdot 10^{-3}$
$\pi^\pm\pi^\mp$	$(1.364 \pm 0.032) \cdot 10^{-3}$
$K^\pm l^\mp \nu_l$	$(6.7 \pm 0.4)\%$
$\pi^\pm\pi^\mp\pi^0$	$(1.31 \pm 0.06)\%$

Table 1.2: Selection of decay modes of the D^0 relevant for this analysis [41].

1.4 Event Generators and Detector Simulation

A measurement of physical quantities like cross sections requires corrections due to the detector response on the final result. This includes the limited acceptance and efficiency as well as the influence of the resolution and bias of the detector components. The treatment of these aspects constitutes the main task for Monte Carlo simulations since it is difficult to determine these corrections for a complete physics analysis directly from the data. Monte Carlo simulations are also used in developing the data selection criteria. The simulations help to determine which

variables are particularly useful for separating signal from background. For these issues the Monte Carlo has to describe the data. Where simulation and data disagree the MC simulation is tuned to model the data behavior in several ways. If detector response is concerned the relevant parts, for example the material distributions, can often be determined directly from data, and then implemented in MC. If the discrepancy between data and MC arise from simulation of the underlying physical processes on the generator level one can either try to vary the parameters (for example fragmentation) or change the physical input for the simulation. When using a MC for correction of measured quantities to the detector response it is common practise to reweight the MC with respect to the generated distributions in order to describe the data.

The Monte Carlo generators RAPGAP [42] and CASCADE [20, 43] perform calculations of charm production in ep-scattering in the massive scheme (see sec. 1.3.1) in leading order pQCD. Higher order corrections within the hard interaction part are implemented via initial state (proton side) and final state (heavy quark side) parton showers. For the parton evolution RAPGAP uses the DGLAP formalism where the PDF-sets CTEQ65m [44] or CTEQ6ll [22] at the starting scale are used within this analysis. CASCADE implies the intrinsic k_t factorisation and parton evolution according to the CCFM equations with the un-integrated parton density function sets A0 [45] or A2 [46]. The renormalisation and factorisation scale for RAPGAP and the renormalisation scale for CASCADE have been set to $\mu_R = \mu_F = \mu_0 = \sqrt{Q^2 + p_T^2}$. The charm quark mass is set to $m_c = 1.43\,\mathrm{GeV}$. Both Monte Carlo generators use the Lund-String-Model for the fragmentation of the light quarks and the Bowler-fragmentation function for the heavy quarks. In both MC simulations the longitudinal part of the fragmentation function is reweighted to the Kartvelishvili function as measured by H1 [40] (see Sec. 4.3.3). When events are generated with RAPGAP, initial and final state QED radiation in LO, i.e. single photon emission off the lepton line, as well as virtual electroweak corrections can be considered via an interface to HERACLES [47].

The detailed simulation of the detector response is contained in the H1SIM-package [48] which is based on the GEANT-program [49]. The simulation contains for example the generation of hits in the tracking chambers as well as showers in the calorimeters. Furthermore inflight decays of the instable hadrons and production of new particles by interactions with the material are considered. The parameters used in this program were determined in test beam measurements and optimised during the ep data taking. As an example for the latter case the description of the dead-material in the central tracking chambers can be cited, which influences the track reconstruction especially at low momenta. For the reconstruction data and simulated events pass through the same program H1REC [50].

1.5 NLO Calculations

In this analysis the HVQDIS program [51, 52] is used for the NLO calculation of D^* cross sections in the massive scheme. This calculation also utilizes the fixed flavour number scheme (FFNS), i.e. three active flavours (u,d,s) in the proton are assumed. Heavy quarks are produced in the hard process, where the BGF dominates. In addition, a small fraction of light quark induced processes with the emitted gluon splitting into a charm anti-charm pair is present. For the calculation the PDF-sets MRST2004FF3nlo [53] and CTEQ5F3 [54] are used. On top of the HVQDIS calculation, which yields complete four vectors of the charm quarks produced, the quarks are fragmented into D^* mesons according to the Kartvelishvili fragmentation function. To obtain the central values for the D^* cross sections, both scales are set to $\mu_R = \mu_F = \mu_0 = \sqrt{Q^2 + 4m_c^2}$ and the charm mass is set at $m_c = 1.43\,\mathrm{GeV}$. Furthermore the fragmentation is calculated with the parameter α (see Eq. 1.36) choosen according to the measurement [40]: $\alpha = 3.3^{+0.4}_{-0.4}$ for $\hat{s} > 70\,\mathrm{GeV}^2$ and $\alpha = 6.0^{+1.1}_{-1.3}$ otherwise. The quantity $\hat{s}$ denoted the centre of mass energy of the $c\bar{c}$-pair. To estimate the theoretical uncertainties the input parameters are varied as follows: The charm mass is varied from $m_c = 1.3\,\mathrm{GeV}$ to $m_c = 1.6\,\mathrm{GeV}$. The renormalisation and factorisation scales have been varied simultanously from $0.5\mu_0$ to $2\mu_0$. The fragmentation parameter is varied within its measurement error. The parton density set CTEQ5F3 [54] was used as an alternative to MRST2004FF3. The resulting uncertainties are added in quadrature and are correlated.

The data are also compared to a NLO prediction in the zero-mass variable-flavour-number scheme (ZMVFNS) [55, 56], where the charm quark is treated as a massless parton in the proton. This calculation has an intrinsic limitation on the transverse D^* momentum in the photon-proton center of mass frame, namely $p_T^*(D^*) > 2$ GeV. Therefore the same additional cut is applied to the data. For the ZMVFNS calculation a charm mass of 1.6 GeV, renormalisation and factorisation scales of $\mu_R = \mu_F = \mu_0 = \sqrt{Q^2 + 4m_c^2}$ and the parton densities CTEQ6.6M [57] are used. The perturbative fragmentation function [58] is evolved at the chosen scale of $p_T^*(D^*)$. The uncertainties on the prediction are estimated by variation of the renormalisation and factorisation scales simultaneously from $0.5\mu_0$ to $2\mu_0$.

Chapter 2

The HERA Storage Ring and the H1 Detector

The analysis presented in this thesis is based on data collected with the H1 experiment at the HERA *ep*-collider during the years 2004-2007. After a short introduction of the HERA accelerator and the H1 experiment the detector components relevant for this analysis will be described in more detail. The main focus lies on the tracking system including track reconstruction and the main calorimeters.

2.1 The HERA Storage Ring

The "Hadron-Electron Ring Anlage" HERA at DESY in Hamburg was the only facility worldwide providing colliding beams of electrons and protons at high energies. Electrons and protons were accelerated to an energy of 27.5 GeV and 920 GeV, respectively. Its operation ended in end of June 2007 after 15 years of successful data taking by the experiments H1 and ZEUS.

The HERA collider has a circumference of 6336 m and consists of two independent rings for the electrons and protons. In Fig. 2.1 a schematic view of the HERA accelerator with the corresponding pre-accelerators is shown. In the center of the four straight sections the experiments are located. At two points in the north and the south the two beam pipes merge into one and the beams are made to collide head-on to provide *ep* interactions for the multi purpose experiments H1 [59] and ZEUS [60]. At the two other points in the west and east the experiments HERMES [61] and HERA-B [62] were located which use only one of the beams respectively: in the HERMES-experiment the electron beam collides with a gas target for investigating the spin structure of the proton. The HERA-B experiment induced proton nucleon interactions at up to eight wire targets with the aim to study the CP-violation in the B-system.

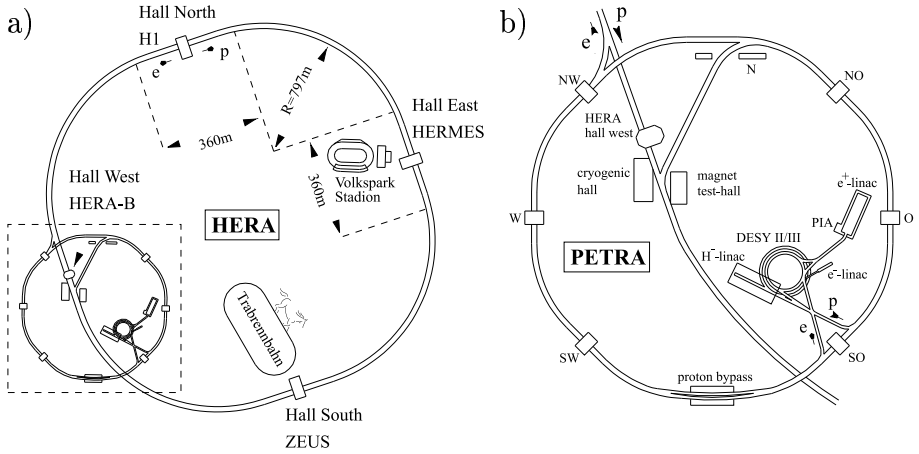

Figure 2.1: The HERA storage ring with the two collider experiments H1 and ZEUS and the two fixed target experiments HERA-B and HERMES (a). Further an enlarged view of the pre-acceleators for HERA (DESY II/III) and PETRA (b) is shown.

At HERA the electrons (positrons) and protons are held in their orbit by magnetic fields. The electron ring magnets operate at ambient temperatures whereas the proton ring magnets use superconducting coils. The strength of the magnetic fields is synchronously adapted to the corresponding energy of the particles during the acceleration process. The particles are accelerated by electrical high frequency fields. For acceleration and storage the beams are bunched. The filling scheme of HERA has in total 220 high frequency slots, called buckets, separated in time by 96 ns. These slots can be filled with particle bunches. The slots of both rings are synchronised in a way to provide bunch-crossings at H1 and ZEUS. Only 180 (or less) of the 220 buckets are filled with particles. The resulting time window is needed for the extraction of the beams.

The protons are accelerated in three steps before being injected from PETRA[1] at 40 GeV to HERA in terms of three bunch trains containing 60 bunches each. The protons are then accelerated to 920 GeV with a high frequency, 52 MHz field overlayed with a 208 MHz field to compress the length of the bunches. This results in a bunch length of typically 1 ns (FWHM) but also in side bunches, called satellites, at distances of 4.8 ns before and after the main bunch. The electrons pass three pre-accelerators in total and are injected from PETRA at an energy of 12 GeV to HERA and then accelerated to 27.6 GeV. The bunches are short enough with a gaussian

[1]Positron Electron Tandem Ring Anlage

profile in beam direction without taking further steps. At the beginning and the end of the PETRA-trains so called electron respectively proton pilot bunches are left unpaired and are used for the estimate of the beam induced background, which is especially important for the measurement of the luminosity.

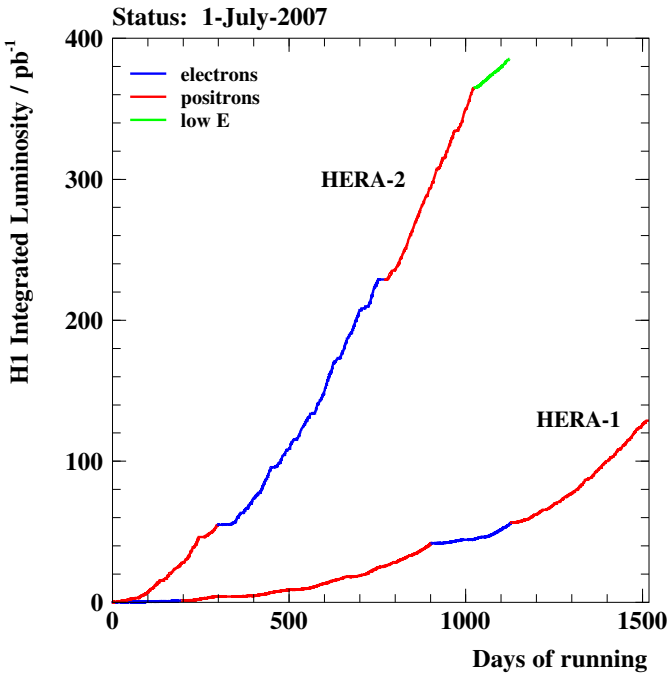

Figure 2.2: The H1 integrated luminosity as function of time for HERA I and HERA II periods, up to the end of HERA running (1st July 2007).

After a successful data taking 1992-2000 (HERAI) with a peak luminosity of the HERA ring of $1.79 \times 10^{31}\,\mathrm{cm}^{-2}\mathrm{s}^{-1}$ in the year 2000, the collider ring has been upgraded during the years 2000-2002 to reach higher luminosities (HERA II). The HERA upgrade project is described in detail in [59, 63]. The goals of this upgrade were an improved sensitivity for detecting non Standard Model physics and an extension of the range of physics experiments to higher Q^2 phenomena compared to HERA I. The luminosity increased approximately by a factor of three to about $4.80 \times 10^{31}\,\mathrm{cm}^{-2}\mathrm{s}^{-1}$. The integrated luminosity for HERA I and HERA II at H1 as a function of the days of running is shown in Fig. 2.2.

To reach the higher luminosities the beam profiles at the collision points have been reduced from $\sigma_x \times \sigma_y = 190\,\mu\mathrm{m} \times 50\,\mu\mathrm{m}$ for HERA I to $\sigma_x \times \sigma_y = 112\,\mu\mathrm{m} \times 30\,\mu\mathrm{m}$ for HERA II. This is achieved by installation of super-conducting focussing magnets inside the detector volume of H1 and ZEUS so that the inner parts of the

detectors had to be rebuild. HERA was further upgraded to be able to operate with higher beam currents but due to bad background conditions the currents were kept nearly the same as for HERA I. The background rates increased due to effects of synchroton radiation emitted by the electrons when bended in the new magnet structures for focussing. A more detailed description concerning the background situation at HERA II can be found in [64, 65]. The following description of the H1 detector refers to the case after the upgrade since this analysis is based on HERA II data.

2.2 The H1 Detector

The H1 detector [59] is build around the northern interaction point of the HERA ring. A three-dimensional representation of the H1 detector and the H1 coordinate system can be seen in Fig. 2.3. It is a general purpose detector designed to measure the direction, energy and charge of the particles originating from the ep collisions in the centre. The protons move through the H1 detector in the direction of the z-axis and the electrons in the opposite direction in the beampipe (1). The H1 detector is constructed to cover the full solid angle (4π) around the interaction point as well as possible. The detector is build asymmetric in the z-direction, reflecting the different energies of the electron and proton beams. The centre of mass of the ep collisions is boosted along the proton direction. Correspondingly, the instrumentation of the H1 detector is predominantly concentrated in the forward region. The backward region is less instrumented and dedicated mainly to the detection of the scattered electron.

The H1 detector (Fig. 2.3) has a typical shell structure. The beam pipe is surrounded by the central (2) and forward (3) tracking detectors. Situated around the trackers is the liquid argon calorimeter (LAr), which is made up of an electromagnetic section (4) and a hadronic section (5). The LAr is in turn surrounded by a superconducting coil (6) which provides an axial field of 1.15 T. The instrumented iron return yoke of the magnet (10) is used to detect muons and hadronic showers that escape the LAr. The forward muon detector (11) covers small angles in the direction of the outgoing protons. The very forward and backward directions are covered by the PLUG (13) and SPACAL (12) calorimeters, respectively, which are situated outside the trackers. Outside the detector region shown in the figure are further installations: The proton remnant tagger (PRT), a detector used in diffractive analysis, is situated 24 m downstream of the interaction point in the forward direction. The forward proton spectrometer (FPS), with sensitive parts reaching into the beam pipe is located between 50m and 100m in the forward direction. It is used to detect scattered final state protons. The electron tagger (ET) and photon detector (PD) are positioned upstream close to the beampipe in the backward direction for the determination of the luminosity by measuring the rate of Bethe-Heitler

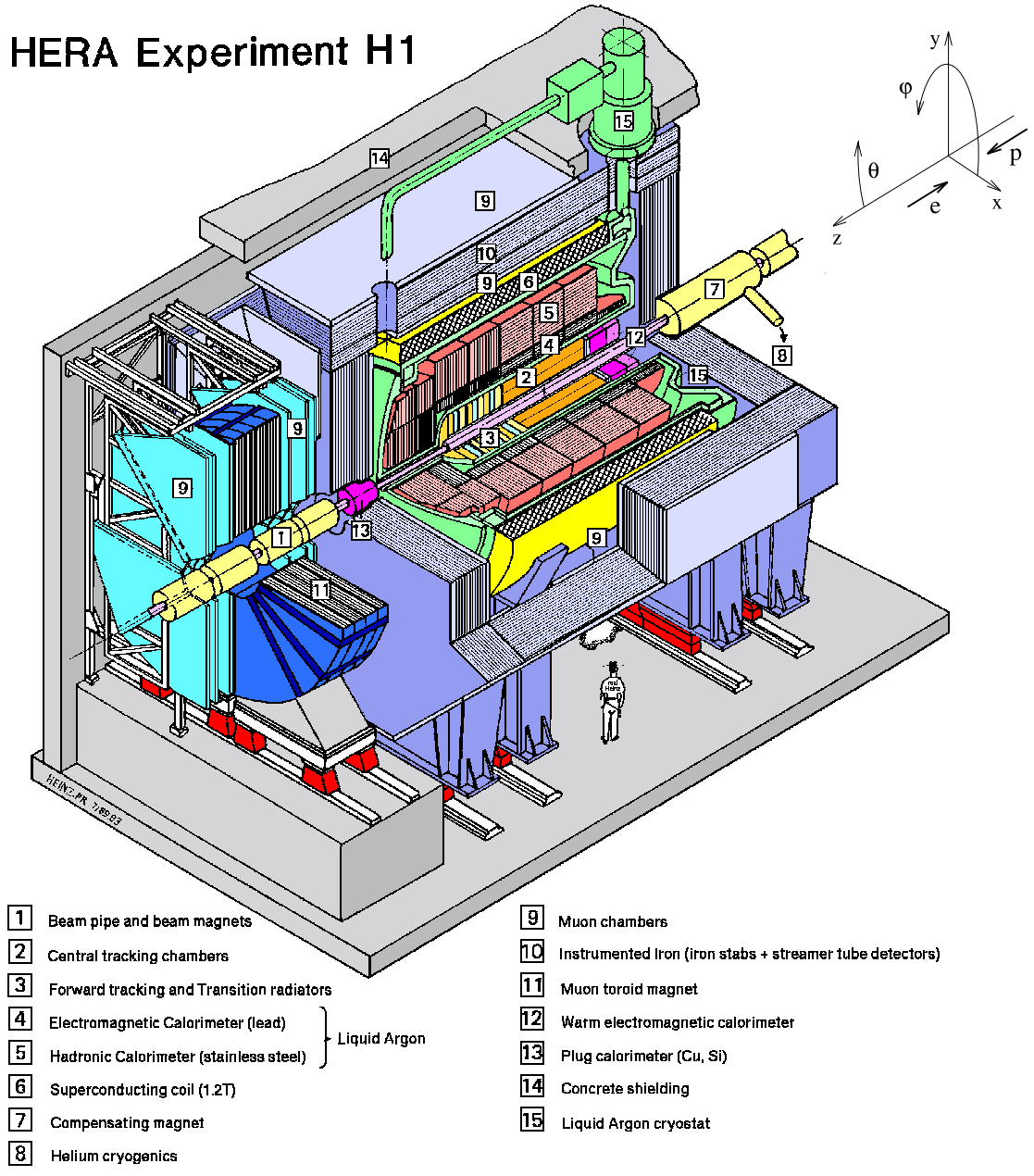

Figure 2.3: A schematic view of the H1 detector. The H1 coordinate system is indicated in the upper right corner.

($ep \rightarrow ep\gamma$) interactions. The ET is also used to tag photoproduction ($Q^2 \sim 0$) events. A more detailed description of the H1 detector can be found in [66,67]. The next sections deal only with the components relevant for this analysis.

The H1 coordinate system (Fig. 2.3) is described in the following: The positive z-direction points in direction of the incoming protons as mentioned above. The x-axis points towards the center of the HERA ring and the y-axis to the sky. The origin of the coordinate system is the nominal interaction point. The polar angle θ is the angle between a trajectory starting in the origin and the z-axis. The azimuth direction angle ϕ is defined in the xy-plane where $\phi = 0$ corresponds to the direction of the x-axis.

2.3 The Central Tracking System

The central tracking system of the H1 detector (see Fig. 2.3) measures the trajectories (tracks) of charged particles and the event vertex. The curvature of the tracks

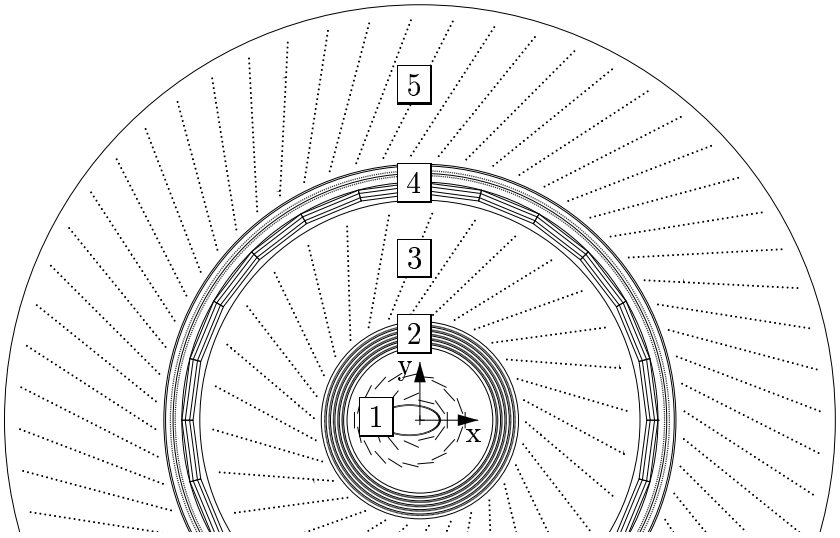

Figure 2.4: Radial view of the central tracking system at H1. The different parts indicated by the numbers are from inside out: beampipe/CST (1), CIP (2), CJC1(3), COZ (4) and CJC2 (5). In the CJC1 and CJC2 the sense wires stretched parallel to the beam direction are shown as points.

in the magnetic field allows determination of their momenta and sign of charge. Fig. 2.4 shows a radial view of the central tracking system. Directly following the

beampipe is the micro vertex detector Central Silicon Tracker (CST) (1) with its semi-conductor strip detectors. It is complemented by further silicon detectors in forward (FST) and backward (BST) direction not shown in the figure. The central inner proportional chamber CIP (2) is used for the online event-selection by measurement of the z-position of the tracks. The central jet chamber consists of two concentric chambers CJC1 (3) and CJC2 (5). It is the main component of the central tracking system providing an accurate reconstruction of the transverse momentum and the azimuthal angle of the tracks but has only a moderate resolution in z-direction. To improve the z-resolution the central outer z-chamber COZ (4) located between the two jet chambers was added. Further tracking detectors not shown in the radial view are the the backward proportional chamber BPC used to support the angular measurement of the scattered electron and the forward tracking detectors (FTD) shown in Fig. 2.3.

The central jet chambers CJC1 and CJC2 are described in more detail in the next section followed by a brief introduction to the CST, CIP and COZ. The reconstruction of tracks to physics analysis level is described in the last section.

2.3.1 The Central Jet Chambers

The main component of the tracking system CJC [68] consists of two larger cylindrical drift chambers CJC1 and CJC2. Both chambers have a total length in z from

Parameter	**CJC1**	**CJC2**
Total length in z	2500 mm	
Active length in z	2200 mm	
Inner radius R_i	203 mm	530 mm
Outer radius R_o	451 mm	844 mm
Number of cells	30	60
Number of signal wires	720	1920
Max. drift distance at R_i	22.9 mm	28.5 mm
Max. drift distance at R_o	44.5 mm	43.1 mm
Drift speed	$\approx 50\,\mathrm{mm}/\mu s$	
Resolution in $r\phi$	170 μm	
Resolution in z	22 mm	
Double hit resolution	2 mm	

Table 2.1: Parameters of the CJC [67].

-112.5 cm to $+107.5$ cm enclosing the CIP with an inner radius of 20.3 cm and an outer radius of 84.4 cm. The material between the CJC1 and CJC2 (COZ) has a

thickness of 1.5% X_0 for perpendicular crossing particles. The interactions of the particles with the material (energy loss, multiple scattering) are especially relevant for the reconstruction of low momentum tracks (see App. B). With the requirement that a track from the primary vertex should be at least completely visible in CJC1 the angular coverage is limited to $20° < \theta < 160°$. The main parameters of the CJC are summarized in Tab. 2.1.

The CJC1 consists of 30 cells with 24 sense wires parallel to the z-axis and the CJC2 has 60 cells with 32 wires each. The cells extend over the full radial span of CJC1 and CJC2 each with no further subdivision as shown in Fig. 2.4. This reduces the disturbing influence of field shaping wires at the inner and outer end. From the drift time measured by the anode wires, single hits are reconstructed with a spatial resolution in the $r\phi$-plane of about 170 μm whereas along the anode wires a resolution of about 22 mm is achieved by charge division. The event timing can be determined with an accuracy of about 1 ns from the drift times. The transverse momentum resolution from the track reconstruction in the $r\phi$-plane has been determined to $\sigma(p_T)/p_T \simeq 0.005\, p_T/\text{GeV} \oplus 0.015$ [69].

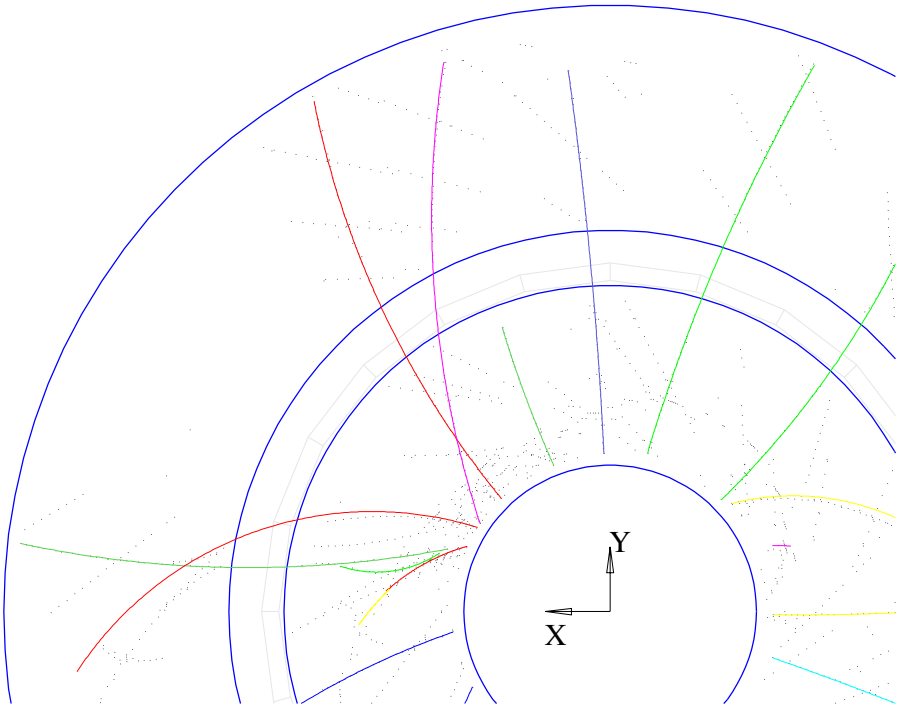

Figure 2.5: Hits and reconstructed tracks in the CJC of an event taken by H1. The mirror tracks are identified and rejected within the track reconstruction procedure.

The cells of the CJC1 and CJC2 are tilted by about 30° such that in the presence of the magnetic field the secondary electrons drift approximately perpendicular to "stiff" tracks (high momentum tracks from the center) which gives not only an optimal track resolution but also leads to further advantages: In Fig. 2.5 the hits and reconstructed tracks are shown from one event taken by H1. In a drift chamber it is a priori not clear if the particle passes the signal wire on the left or on the right. Therefore there are two solutions possible with the same distance to the signal wire. The wrong solution is called mirror hit. From these mirror hits so called mirror track segments are reconstructed. Due to the tilted cells the wrong mirror track segments in neighbouring drift cells do not match as well as they do not point to the event vertex. Therefore the usual drift chamber ambiguity is easily resolved [2]. Each "stiff" track crosses the sense wire plane at least once in CJC1 and in CJC2. From the fine match at crossing, the passing time of a particle can be determined to an accuracy of about 0.5 ns. This allows an easy separation of tracks coming from a different bunch crossing.

2.3.2 Complementary Trackers

The **central silicon tracker (CST)** [70] provides precise vertex and track information near the interaction point. It consists of two layers which are located around the beam pipe at a distance of 5 cm and 10 cm respectively. Due to the elliptic form of the beam pipe, the sensors of the CST are arranged on two concentric ellipses too. The CST is not able to measure tracks by itself since it has only two layers providing two space points but is used to improve tracks reconstructed in CJC1 and CJC2. The strip detectors are double-sided providing points in $r\phi$ and z. With the p-doped side the position in the $r\phi$-plane is measured where in combination with the CJC measurement a track resolution of $\sim 40\,\mu$m with respect to the vertex is achieved. With the n-side the z-position of the track is measured with a resolution of $\sim 70\,\mu$m.

The **central inner proportional chamber (CIP)** [71, 72] consists of 5 active detector layers. It is a multiwire proportional chamber with pad readout whose wires are stretched parallel to the beam. The CIP encloses the CST circularly with an inner radius of 15.7 cm and an outer radius of 19.3 cm. The CIP covers in z-direction a region from $z = -112.7$ cm to $z = +104.3$ cm corresponding to an angular acceptance in θ from $11° - 169°$. Due to the fast response time of the detector of ~ 75 ns this chamber is used for the online event selection and also allows for a determination of time of the interaction (event t_0). For triggering, tracks are reconstructed using masks and especially their z-position is used.

[2] It will be shown in App. B that in some cases the track reconstruction takes the mirror hits instead of the right ones.

The **central outer z-chamber (COZ)** [67] is located between the CJC1 and CJC2 with an an angular acceptance in θ of $25° - 155°$. The COZ is a drift chamber with signal wires stretched perpendicular to the **z**-direction providing an accurate measurement of the z-position of a passing charged particle via the drift time. The chamber achieves a resolution in z of $\sigma_z \approx 350\,\mu$m. Due to the much better resolution in z in comparison to the central jet chambers, the COZ hits are linked to the CJC tracks.

2.3.3 Track Reconstruction

The helical trajectory of the charged particles is described by the five parameters κ, dca, ϕ, θ and z_0. The curvature of the track κ is related to the transverse momentum p_t of the particle as:

$$p_t[GeV] = -Q[e] \cdot 0.29979 B_z[T] \cdot \frac{1}{\kappa[m^{-1}]}, \tag{2.1}$$

where B_z is the strength of the magnetic field in z-direction and Q the charge of the particle. The quantity dca (distance of closest approach) is the smallest distance in the $r\phi$-plane between the trajectory and the origin of the (H1) coordinate system. The azimuthal angle ϕ is the angle of the track in the $r\phi$ plane at dca. The polar angle θ is the angle between the track and the z-axis. The last parameter z_0 is the distance in z to the origin at dca.

The track reconstruction at H1 is described in detail in [73, 74]. It starts with the reconstruction of tracks in the CJC. The tracks are first fitted in the $r\phi$-plane. The algorithm starts with fitting of hit triplets to obtain so called track seeds. Then further hits which are matching the extrapolated trajectory are assigned to the track. The track residuals from the newly found hits and the original ones enter the new fit. These steps are repeated until the whole track is reconstructed. The circle fit in the $r\phi$-plane is combined with the fit of the helix in z, i.e. a fit to a straight line in the zS-plane, where S is the arc length of the helix in $r\phi$. After reconstructing the tracks using CJC information alone, information from other track detectors, e.g. COZ for better z measurement, are added successively and the track fit is repeated.

Due to non uniformities of the magnetic field and interactions of the particles with the detector material (e.g. energy loss, multiple scattering) the real trajectory differs more or less from an ideal helix. Such effects are considered by the fit algorithms as well as routines applying corrections to the helix parameters after the fit. For the corrections detailed material discriptions of the detectors are used.

Based on the reconstructed tracks the primary event vertex can be determined, which is first done in the $r\phi$-plane. With the tracks pointing to the vertex in the $r\phi$-plane the z-position is then determined. Whereas the vertex position in the $r\phi$-plane can vary only some $100\,\mu m$ due to the small radial dimension of the beams,

the z-vertex position varies up to $\pm 35\,cm$. For tracks which are compatible with the event vertex and are not coming from a secondary decay, the track fit in $r\phi$ and z is repeated with the helix constrained on the event vertex. With similar procedures secondary vertices are reconstructed too which originate from particle decays, photon conversions and nuclear interactions. For the D^* analysis only primary vertex fitted tracks are used whereas in the track efficiency studies with K_s^0 (see App. B) with decay length of several cm tracks from secondary vertex fits are used.

2.4 The Liquid Argon Calorimeter

The liquid argon calorimeter (LAr) [75] provides the measurement of the scattered electron at high Q^2 and the measurement of the hadronic final state (together with the tracker and the SpaCal). This detector covers the polar angle range of $4^\circ \leq \theta \leq 153^\circ$. The LAr calorimeter is a sampling calorimeter which consists of an inner, fine granulated electromagnetic section and an outer hadronic part with coarser segmentation. Fig. 2.6 shows the longitudinal cross section of the LAr calorimeter. In z-direction the calorimeter is partitioned into eight distinct wheels, named according to their position in z: backward barrel (BB), central barrel (CB1,CB2,CB3), forward barrel (FB1,FB2), outer forward (OF) and inner forward (IF). The BB consists of an electromagnetic section (BBE) only whereas the OF only of two hadronic sections (OF1H,OF2H). The wheels are divided in ϕ into eight octants. Fig. 2.7 shows the structure of a central barrel wheel in the $r\phi$-plane. The insensitive areas between the wheels are called "z-cracks" and the ones between octants "ϕ-cracks".

The LAr calorimeter is build up of absorber plates consisting of lead in the electromagnetic section and stainless steel in the hadronic section. To obtain a uniform energy resolution, the orientation of the plates is arranged such that the angle of incidence of particles originating from the nominal interaction point is always larger than 45°. The space between the plates is filled with liquid argon as active medium. The thickness of the electromagnetic section corresponds to $20-30$ radiation lengths and that of the hadronic section $4.7-7$ hadronic interaction lengths. The LAr calorimeter is segmented into about 45000 read-out cells to enable a good spatial resolution of the deposited energies. The segmentation is coarse in the backward part and becomes finer towards the forward direction (see bottom part of Fig. 2.6). In terms of the Moliere radius R_M [41] which is a measure of the transverse extension of electromagnetic showers, the typical size of the cells varies between $2.5\,R_M$ in the backward region and $1.0\,R_M$ in the forward part. The fine granularity allows a clean separation of electromagnetic and hadronic showers providing the basis for an efficient electron identification.

The energies deposited by incident particles in the electromagnetic and hadronic

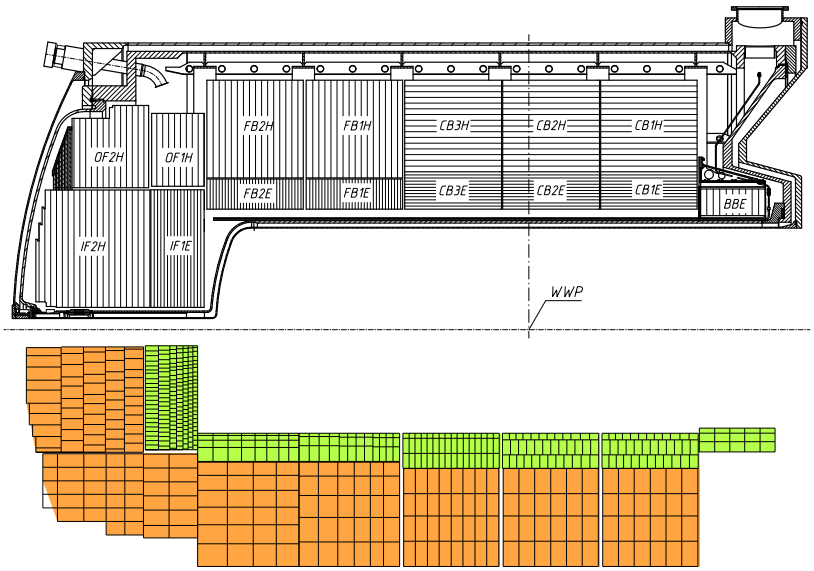

Figure 2.6: Longitudinal cross section of the LAr calorimeter. The upper picture shows the sampling structure with the orientation of the absorber plates. Below is shown the read-out cell structure. "WWP" denotes the nominal interaction point.

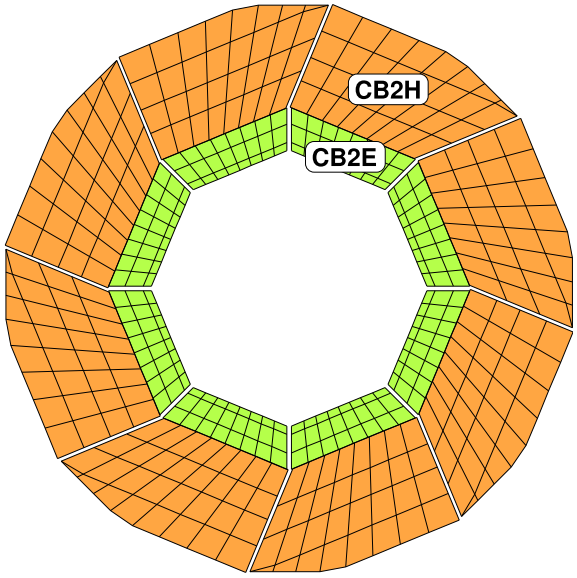

Figure 2.7: Read-out cell structure in the transverse view of a central barrel (CB2) wheel of the LAr calorimeter.

cells are reconstructed in several steps by the LAr reconstruction software [76]. Within the reconstruction charges collected with charge sensitive amplifiers from the read-out pads are converted to energies in the calorimeter cells for both hadronic and electromagnetic showers. For the reconstruction of the energy a charge to energy calibration factor is needed, which was measured for each stack geometry at test-beam experiments. In addition charge collection efficiencies and corrections for local variations of the gap and absorber thickness are considered. Only cells with absolute values of the collected charge two to three standard deviations above the electronic noise are recorded (so-called "zero-suppression").

Using the energy measured in the cells clusters are formed by the reconstruction software, which contain groups of cells which are likely to belong to a shower of the same incident particle [77, 78]. The algorithm works very well for electromagnetic showers where $95-97\%$ of electromagnetic showers are reconstructed as a single cluster. It works less well for hadronic showers due to the broader and more fluctuating shower shape. Hadronic showers induced by single hadrons are often reconstructed as several clusters. Identified hadronic objects are subjected to an energy weighting algorithm [78], which has been developed to equalise the response of the LAr calorimeter to electromagnetic and hadronic showers. The energy resolution of the LAr calorimeter has been determined in test beam measurements to be $\sigma^{em}(E)/E = 12\%/\sqrt{E/\mathrm{GeV}} \oplus 1\%$ for electrons [75] and $\sigma^{had}(E)/E = 50\%/\sqrt{E/\mathrm{GeV}} \oplus 2\%$ for charged pions [79].

2.5 The Spaghetti Calorimeter

The "spaghetti" calorimeter (SpaCal) [80] is installed in the backward region of the H1 detector and covers the polar angular range $153^\circ < \theta < 174^\circ$. It is designed to detect electrons scattered through small angles. Further it allows for the measurement of backward scattered hadrons. Like the LAr calorimeter the SpaCal is a sampling calorimeter and consists of an electromagnetic and a hadronic section. It uses lead as absorber material and scintillating fibres as active material. In Fig. 2.8 a $r\phi$ view of the electromagnetic part is shown.

The electromagnetic section consists of ~ 1150 cells with an active volume of $(40.5 \times 40.5 \times 250)\,\mathrm{mm}^2$ each. These cells are arranged in pairs in submodules. Such a submodule shown in Fig. 2.9 consists of 52 stacked lead plates with 4680 fibres each. The ratio of lead to fibres is $2.27 : 1$. The fibres guide the light to the end of the active material in z-direction where the fibres of one cell are bundled on a light mixer before the photomultiplier. The depth of the active material in z-direction corresponds to 27.47 radiation lengths to ensure that electrons deposit almost their full energy in the electromagnetic section. Eight of the submodules are grouped to a module (thick lines in Fig. 2.8). The energy resolution of the electromagnetic part

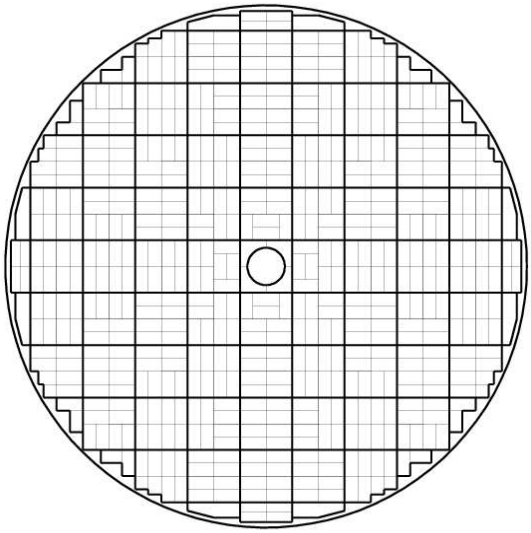

Figure 2.8: Drawing of the backward spaghetti calorimeter (SpaCal). The thin lines indicates the sub modules where eight of them are grouped to modules each (thick lines)

has been measured to be $\sigma^{em}(E)/E = 7\%/\sqrt{E/GeV} \oplus 1\%$ [81].

The hadronic section is build very similar. The cells are four times larger in $r\phi$ than in the electromagnetic section and the ratio between absorber to scintillator is $3.4 : 1$. The depth is also 250 mm corresponding to only one hadronic interaction length. The hadronic section is mainly used as veto against hadrons for the electron identification.

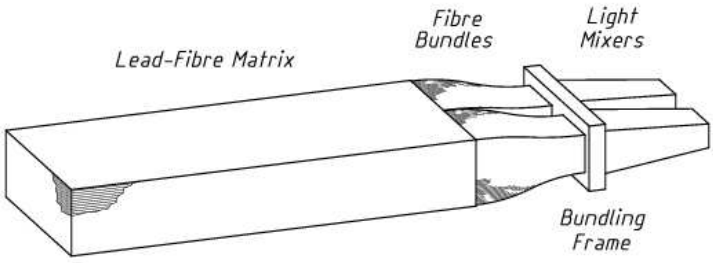

Figure 2.9: Schematic view of a sub module of the electromagnetic SpaCal calorimeter

2.6 Luminosity Measurement

The luminosity measurement at H1 [82] is based on the rate measurement of the Bethe-Heitler-process $ep \rightarrow ep\gamma$ [83]. This process is calculable in QED and therefore suitable for determination of the luminosity. The produced photon is identified in the photon detector at $z = -101.8\,\mathrm{m}$. The detector is a sampling calorimeter consisting of silica fibres and tungsten absorber. For suppressing background a beryllium filter and a water cherenkov counter are mounted in front of the detector. The scattered electrons from the ep process do not reach the detector since they are swept away by the HERA magnets. However the beam optics directs the scattered electrons into the acceptance of the electron tagger, installed at $z = -5.4\,\mathrm{m}$. This detector is a calorimeter used to measure the energies of the scattered electron e.g. from low Q^2 photoproduction processes. For the luminosity measurement this electron measurement serves only as a check of the photon detector.

2.7 Trigger

As mentioned in Sec. 2.1 the HERA bunch crossing interval is 96 ns corresponding to a bunch crossing frequency of $\sim$ 10 MHz and is about four orders of magnitude smaller than the time needed by the H1 detector to write out information from its various components. However the background processes have a rate of about 10^4 times higher than the electron-proton collisions. The background is mostly caused by

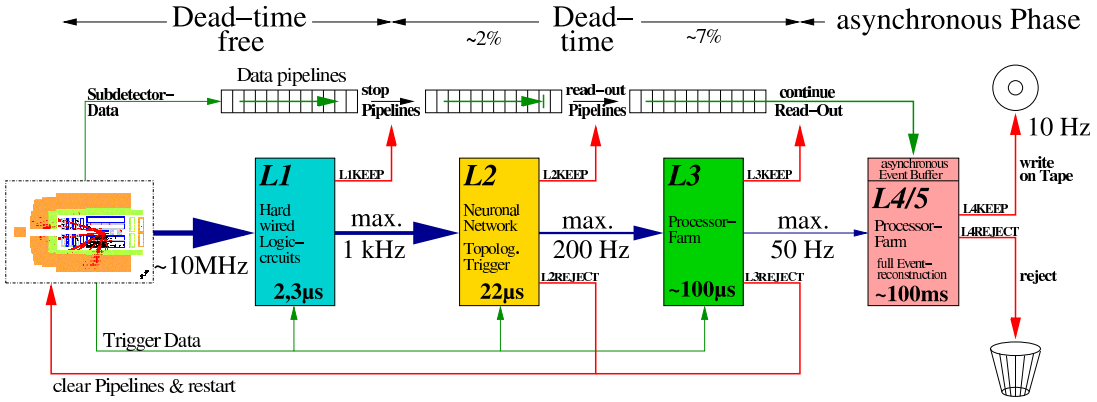

Figure 2.10: The four-level triggersystem of the H1 experiment. The first three trigger levels are synchronized to the bunch crossings, but only the first level is dead time free. The fourth level selects the events after a complete event reconstruction.

interactions of the proton beam with the beam pipe (proton-beam-wall interactions)

or residual gas (proton-beam-gas interactions) as well as particles from beam halo and cosmic muons. It is therefore essential to design a trigger that selects interesting collisions in a manner that minimises the dead-time of the detector.

For this purpose, the H1 detector uses a pipelined, multi-layered trigger system consisting of four levels [84]. The trigger system is shown in Fig. 2.10. At each level the input rate is sucessively reduced and the time available for analysis of the event increases. Thus with increasing trigger level more complex algorithms using more detector information for the decision are possible. The fourth trigger level selects events after the complete readout of the detector and has no influence on the dead time. Altogether a reduction of the rates from 10 MHz to ca. 10 Hz, at which the data are permanentely saved, is reached.

Chapter 3

D* Sample

This chapter addresses the reconstruction of the D* sample in DIS on which the analysis is based. After a short description of the run selection and the triggers used, the reconstruction of the scattered electron in LAr and SpaCal is explained. Special attention is given to the quality of the electron reconstruction in the overlap region between SpaCal and LAr. Subsequently the trigger efficiencies for the electron sample will be described. The last part of the chapter is devoted to the reconstruction of the D* mesons from the decay particles using tracks in the central detector. The background suppression will be illustrated and invariant mass distributions of the D^* and D^0 as well as control distributions will be presented.

3.1 General Event Selection

The H1 data used in this analysis cover the complete HERAII period from 2004 until the end of the high energy running in spring of 2007. During a data taking run most of the controllable conditions like the number of detector components in the readout as well as the prescale factors of the triggers are kept constant. Due to the changing beam conditions within a HERA fill a run normally covers a time interval of less than one hour. The runs used in the analysis have to fulfill the following conditions:

- Each run is classified as good, medium or bad depending on the conditions of the subdetectors and the quality of the beams. Bad runs, in which an important detector component like the CJC or the luminosity system were not working are discarded from the analysis.

- The following detector components had to be switched on and included in the readout: The tracking chambers CJC1, CJC2 and CIP, the calorimeters LAr

and SpaCal, the luminosity system and the time of flight TOF and VETO systems [85].

- A minimum luminosity of $0.1\,\mathrm{nb}^{-1}$ for a single run is required.

- The trigger mix used during a run depends on the trigger phase, which is choosen on the basis of the actual HERA status. For this analysis trigger phase 2 (luminosity run) is required. Both of the subtriggers s67 and s61 which are used in the analysis and are sensitive to the detection of a scattered electron in the LAr or the SpaCal calorimeters respectively (see Sec. 3.2), have to be online and in the readout.

The high voltage of the track chambers, especially CJC1 and CJC2, can be switched off during a run to protect the chambers against large currents due to increasing background. Such periods within a run are rejected. The z position of the primary vertex z_{vtx} has to fulfill the condition $|z_{vtx}| < 35\,cm$ to select the processes originating from ep scattering at the interaction point. The data set selected by the criteria mentioned above corresponds to an integrated luminosity of $\mathcal{L} = 351 \pm 11\,\mathrm{pb}^{-1}$. The error on the luminosity is discussed in Sec. 4.6.

3.2 Trigger Selection

For the online triggering of the scattered electron the subtriggers s67 (for LAr) and s61 (for SpaCal) were used. Both triggers have only L1 conditions. The main component of the subtrigger s67 [9] is the trigger element LAr_electron_1 which is set if the electromagnetic energy deposited in a "big tower" (group of cells where the energy is deposited) exceeds a certain threshold value. The threshold for the LAr_electron_1 trigger element range from 5 GeV in the backward region to 25 GeV in the forward region. This subtrigger contains further elements like veto conditions using the CIP and the time of flight (ToF) system. They mainly reject background from beam-gas and beam-wall interactions. The subtrigger s61 uses trigger informations from two detector components. First an energy deposition of at least 9 GeV in the SpaCal is required. The second condition is the detection of at least one track in the CJC with a transverse momentum above 0.9 GeV for which the H1 fast track trigger (FTT) is used [86].

When accepted by one of the two subtriggers (s67 or s61 actual) the event has to pass the final trigger level (L4). Since the photon virtuality Q^2 is larger than $5\,\mathrm{GeV}^2$ the events are generally accepted at L4 with a prescale of 1.

3.3 Interaction Vertex

For an adequate reconstruction of the event kinematics the precise knowledge of the ep interaction position is needed. In particular the z position of the vertex is directly used in the measurement of the polar angle of the scattered electron θ_e based on calorimeter information. Therefore the vertex position distribution has to be well modelled in the Monte Carlo (MC) simulation.

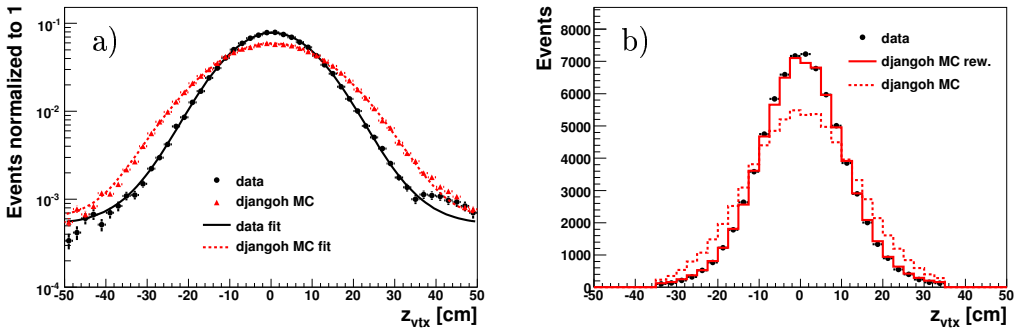

Figure 3.1: Distributions of z_{vtx} for data and MC with double gaussian fit (a) and comparison of the z_{vtx} distributions from data with MC before and after reweighting (b).

The primary interaction vertex is distributed in z around the nominal interaction point (z=0) due to the longitudinal size of the beam bunches with $\sigma_z(p) \approx 13\,\mathrm{cm}$ for the proton bunches and $\sigma_z(e) \approx 2\,\mathrm{cm}$ for the electron bunches. The mean value of z_{vtx} depends on the beam settings of the accelerator and therefore is different for each HERA fill. For fixed beam parameters the z_{vtx} distribution is approximately gaussian.

Monte Carlo events are simulated using a gaussian z_{vtx} distribution with a mean $\langle z_{vtx} \rangle = 0$ and a width $\sigma(MC) = 13\,\mathrm{cm}$. To model the z vertex distribution of the data the simulated events are reweighted in z preserving the overall normalisation. To get the z vertex distributions for reweighting the DIS selection criteria described in the next section are applied. To avoid biases due to the geometrical acceptance of the LAr and SpaCal calorimeters in the backward region, the polar angle of the scattered electron is required to be $\theta_e < 145°$. For the reweighting first the z_{vtx} distributions in data and MC (each normalized to 1) are fitted by $f_{fit,data}(z_{vtx})$ and $f_{fit,MC}(z_{vtx})$ defined as a sum of two gaussian distributions plus a constant in case of data. The z vertex distributions together with the fit functions are shown in Fig. 3.1 (a) with a reasonable description of the distributions by the fitted functions. However the z vertex distribution for data shows a bump at the right tail caused by

nuclear interactions in the beam pipe [9]. This excess of events is not described by the fit but negligible.

The ratio

$$w_{rew}\left(z_{vtx,gen}\right) = \frac{f_{fit,data}\left(z_{vtx,gen}\right)}{f_{fit,MC}\left(z_{vtx,gen}\right)} \tag{3.1}$$

is used to reweight the MC as a function of the generated z position of the vertex $z_{vtx,gen}$. Fig. 3.1 (b) shows the comparison of the z_{vtx} distributions from data with MC before and after reweighting. The reweighted distribution describes the data well which is not obvious since the reweighting function applied on the generated quantity $z_{vtx,gen}$ is determined from distributions at the reconstruction level.

3.4 Reconstruction of DIS Events

3.4.1 Reconstruction of the Kinematics

The DIS kinematics as described in Sec. 1.1 is reconstructed by using information from the measurement of the scattered electron as well as the hadronic final state. Due to the momentum balance between the scattered electron and the hadronic final state there are different ways to combine the redundant information for reconstructing the kinematics. In this analysis the electron-Σ method [87] is applied where the kinematics is calculated as follows:

$$Q_e^2 = E_e E_e'(1 + \cos\theta_e) \tag{3.2}$$

$$y_\Sigma = \frac{2y_h \cdot E_e'}{2y_h E_e' + E_e \cdot (1 - \cos\theta_e)} \tag{3.3}$$

$$Q_\Sigma^2 = \frac{E_e^2 \cdot \sin^2\theta_e}{1 - y_\Sigma} \tag{3.4}$$

$$x_\Sigma = \frac{Q_\Sigma^2}{y_\Sigma \cdot s} \tag{3.5}$$

$$y_{e\Sigma} = \frac{Q_e^2}{x_\Sigma \cdot s} \tag{3.6}$$

Here $E_e \approx 27.6\,GeV$ is the energy of the incoming electron, s the center of mass energy of the electron-proton system and E_e', θ_e are the energy and the polar angle of the scattered electron. In Eq. 3.3 the information of the hadronic final state is used via y_h which is given by:

$$y_h = \frac{\Sigma}{2 \cdot E_e}, \text{ with } \Sigma = \sum_i \left(E_i - P_{z,i}\right) \tag{3.7}$$

where the sum runs over the hadronic final state objects with energy E_i and momentum components along beam direction $P_{z,i}$. The reconstruction of the hadronic final state objects from the tracks and clusters is described in detail in [88,89]. If all particles are reconstructed the longitudinal momentum balance of the event $E - p_z$ given by:

$$(E - p_z) \equiv \Sigma + E'_e(1 - \cos\theta_e) \text{ with } \Sigma = \sum_i (E_i - P_{z,i}) \tag{3.8}$$

peaks at $E - p_z \approx 55\,\mathrm{GeV}^2$. It has been shown in [86] that the $e\Sigma$ method provides the optimal resolution in the measurement of the kinematic variables in the kinematic range $100 < Q^2 < 1000\,\mathrm{GeV}^2$ and $0.02 < y < 0.7$.

3.4.2 Scattered Electron Selection

The scattered electron is reconstructed either in the LAr or in the SpaCal calorimeter. There are no mixed clusters with cells from both calorimeters[1]. To minimize the misidentification of hadrons as electrons the fraction of the total energy of the cluster stored in the electromagnetic part of the calorimeter has to be > 0.85 for SpaCal clusters and $> 0.94 + 0.05\cos(2\theta)$ in the case of LAr. For the same reason an upper cut on the energy weighted cluster radius is applied ($< 4\,\mathrm{cm}$) since hadronic showers are normally broader than electromagnetic showers. The chance to misidentify a hadron as an electron is smaller than 1% for $E'_e > 11\,\mathrm{GeV}$ [9]. However, an electron in a jet may still fake a scattered electron. The isolation of the identified electromagnetic particle against other calorimeter deposits is tested by examining the total calorimetric energy not belonging to the electron, E_{cone}, in a cone of radius $R_{\eta-\phi} = \sqrt{(\Delta\eta)^2 + (\Delta\phi)^2} = 0.5$ in the $\eta - \phi$ space [2]. Electrons are treated as isolated if $E_{cone}/E_{tot} < 5\,\%$. The detailed description of the electron reconstruction can be found in [9]. Finally if more than one candidate fulfills the conditions for the scattered electron, the one with the highest transverse momentum is choosen.

In this analysis the energy of the scattered electron E'_e is required to be $E'_e > 8\,\mathrm{GeV}$, as the LAr trigger efficiency becomes low at small energies [90]. The acceptance of the electron reconstruction in LAr or SpaCal in the backward region is defined by the two variables: z_{impact} in case of the LAr which is defined as the z position where the electron track, approximated by a straight line[3] between the center of the cluster and the primary interaction vertex, crosses the inner surface of the LAr calorimeter. In the case of the SpaCal the distance of the cluster from the origin in the $r\phi$ plane $d_{\perp,clus}$ is used. The cuts $z_{impact} < -190\,\mathrm{cm}$ and $d_{\perp,clus} < 74\,\mathrm{cm}$

[1] For electron candidates propagating at the outer edge of the SpaCal additional clusters in the LAr (BBE) may be formed from the shower tails.

[2] $\eta = -\ln(\tan(\theta/2))$ is the pseudo rapidity

[3] At the typical energies of the scattered electron the curvature of the track due to the magnetic field can be neglected

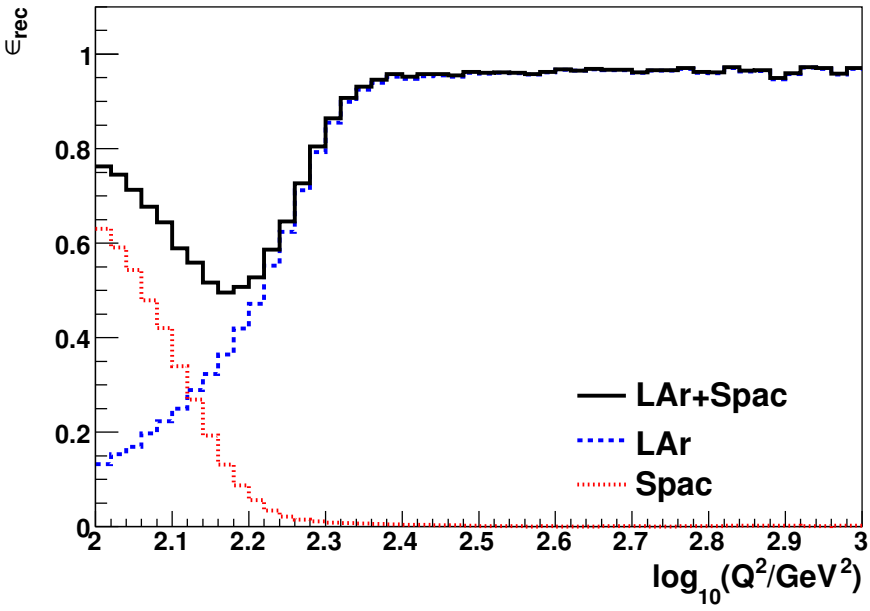

Figure 3.2: Reconstruction efficiency for the scattered electron estimated with DJANGO MC for the cuts described above (black line). Further shown the efficiencies for the LAr sample (blue) and SpaCal sample (red) alone.

are choosen on the basis of the two criteria: constant high reconstruction efficiency as a function of these variables and good quality of the measurement of E'_e and θ_e (see Sec. 3.4.4). Furthermore a non vertex fitted CJC track is required to match the electron cluster[4] with $DCA_{track-cluster} < 12\,\text{cm}$ where $DCA_{track-cluster}$ is the distance of closest approach between the extrapolation of the CJC track and the center of gravity of the cluster.

Fig. 3.2 shows the electron reconstruction efficiency for the cuts described above as a function of $\log_{10}(Q^2)$ for the visible range estimated with DJANGO inclusive MC. On the generator level only electrons with an energy of more than 8 GeV are taken into account. The efficiency using either the LAr or the SpaCal is also indicated. The efficiency is very high ($> 95\%$) for $log_{10}(Q^2/\text{GeV}^2) > 2.4$ and decreases to $\approx$ 50 % at lower Q^2 due to the acceptance gap in the overlap region between SpaCal and LAr.

Fig. 3.3 shows the distribution of the events in the Q^2/x-plane for the electron sample and the influence of the cuts on z_{impact} and $d_{\perp,clus}$ for the nominal z position

[4] The reason why not a vertex fitted track is matched will be explained in Sec. 4.6.3.

of the vertex $z_{vtx} = 0\,\mathrm{cm}$. The contributions between the borders of the cut-offs arise from smearing due to different z positions of the primary vertex.

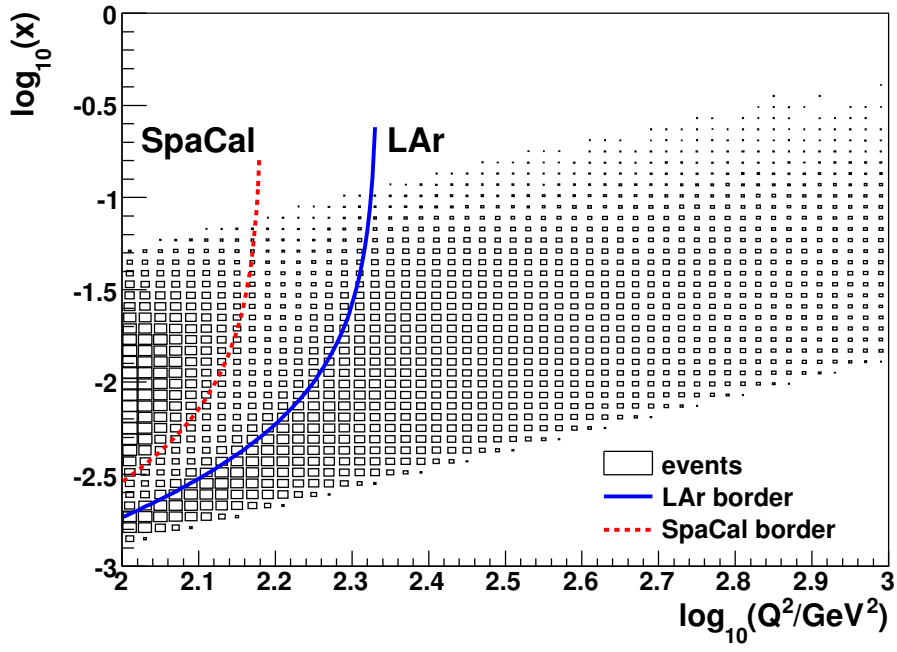

Figure 3.3: Distribution of the events in the Q^2/x-plane for the cuts described above. The lines indicate the cuts on z_{impact} and $d_{\perp,clus}$ for the nominal z position of the Vertex ($z_{vtx} = 0\,\mathrm{cm}$)

3.4.3 Control Plots

In Fig. 3.4 the control distributions for the measurement of the scattered electron in the LAr (left) and SpaCal (right) are shown. The data distributions (filled symbols) are compared with the results from MC simulation where the MC generator DJANGO [91] for the simulation of inclusive DIS events is used. The energy of the electron E'_e reconstructed in the SpaCal and the scattering angle θ_e of the electron measured in both calorimeters as well as the impact positions z_{impact} and $d_{\perp,clus}$ are well described by the MC simulation. The MC prediction differs slightly from data

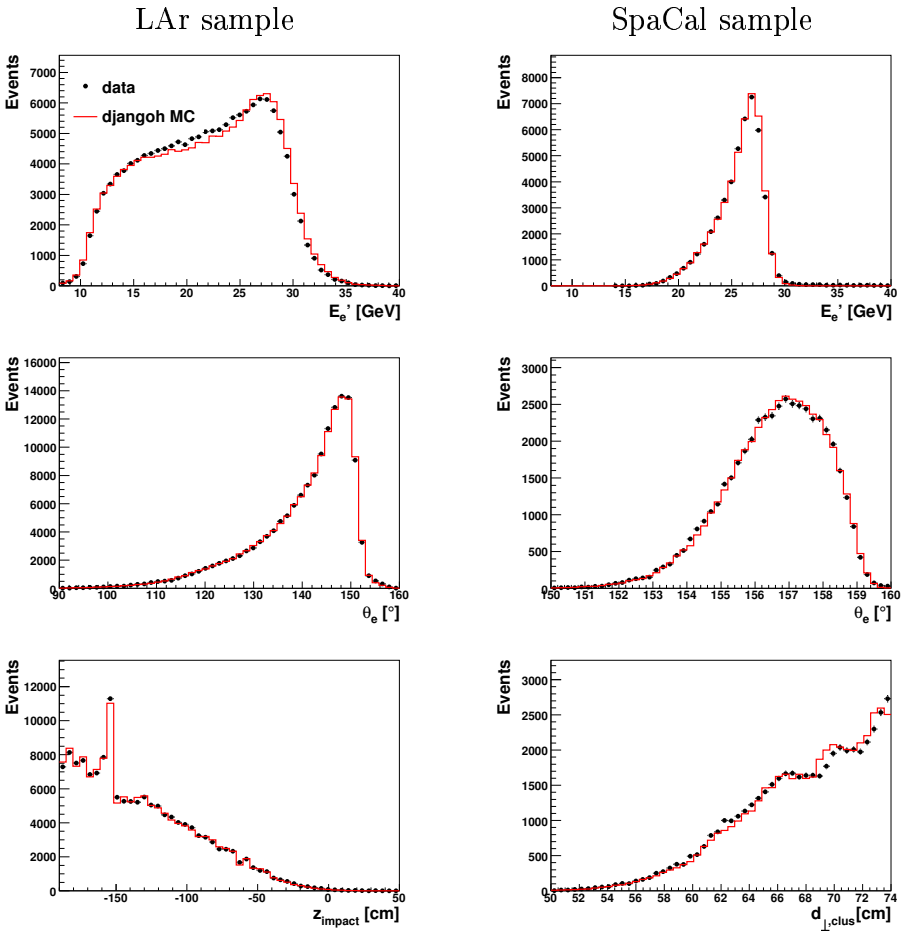

Figure 3.4: Control distributions for the electron reconstruction in LAr (left) and SpaCal (right). Shown are the reconstructed energy E'_e, the scattering angle θ_e and the impact positions z_{impact} and $d_{\perp,clus}$.

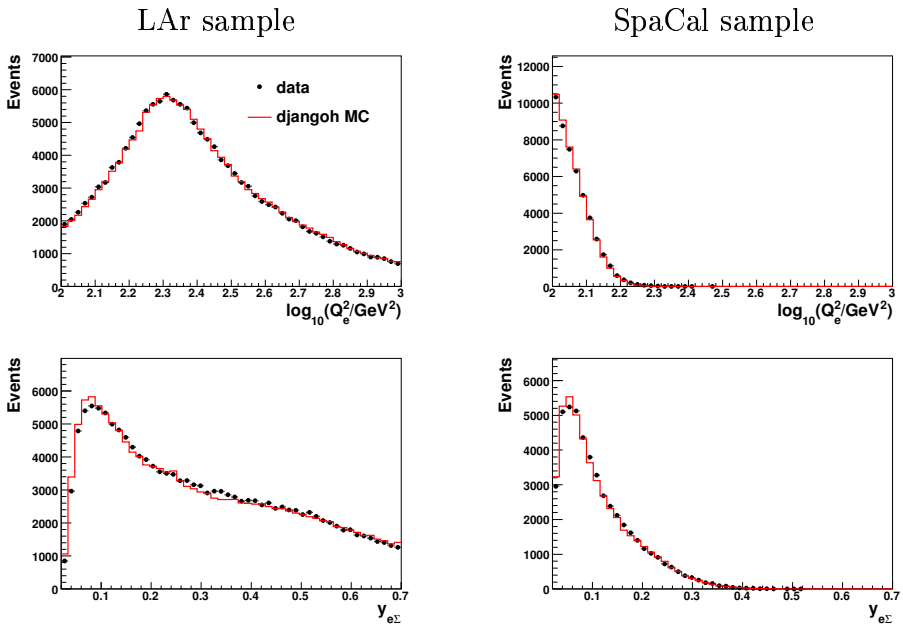

Figure 3.5: Control distributions for the reconstruction of the kinematic variables Q_e^2 and $y_{e\Sigma}$ for the LAr sample (left) and the SpaCal sample (right).

in the distribution of the electron energy reconstructed in LAr. In the SpaCal, the mean energy of the scattered electron is much higher than in LAr. The peak in the z_{impact} distribution corresponds to events where the electron track enters the front face of the BBE wheel at $z_{impact} = -152.5\,\mathrm{cm}$ without passing the CB1 wheel (see Sec. 2.4).

In Fig. 3.5 the control distributions of the kinematic variables Q_e^2 and $y_{e\Sigma}$ used in this analysis are shown. The distributions are well described by the MC simulation in both LAr and SpaCal.

3.4.4 Calibration of the Electron and HFS Measurement

To check the LAr and SpaCal energy calibration the energy from the double angle method [9] is used as an independent reference scale. This method is based on the measurement of the electron scattering angle and the inclusive hadron angle γ_h which is defined as:

$$\gamma_h = 2 \cdot \arctan\left(\frac{\Sigma}{P_{T,h}}\right), \text{ with } \Sigma = E_h - P_{z,h} \tag{3.9}$$

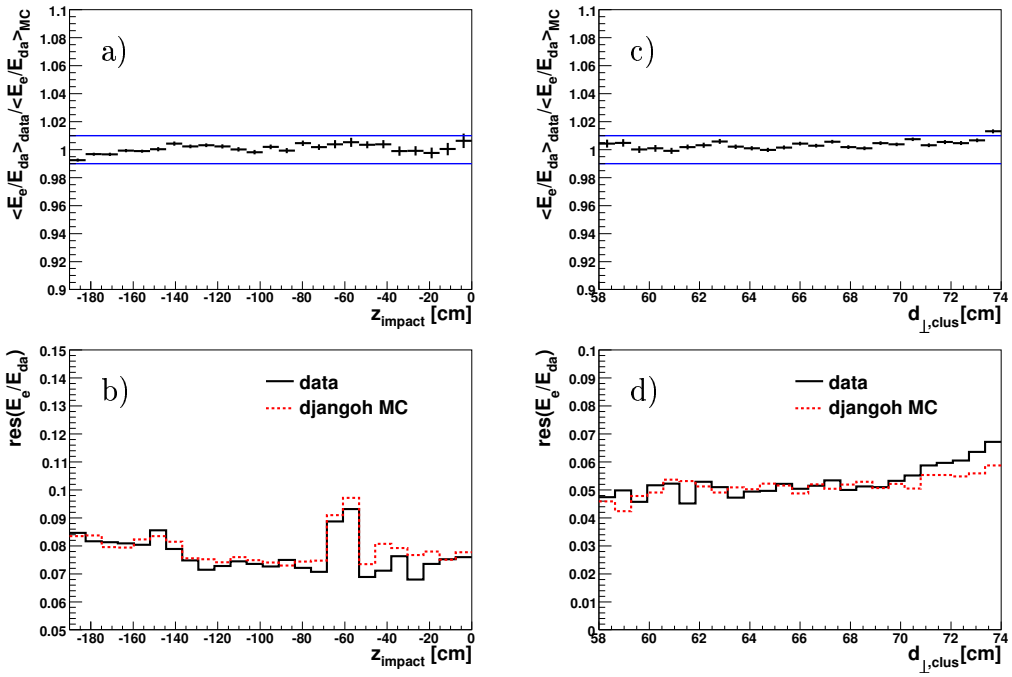

Figure 3.6: Double ratios $\langle E_e/E_{da}\rangle_{data}/\langle E_e/E_{da}\rangle_{MC}$ and resolutions in E_e/E_{da} for the LAr sample in bins of z_{impact} (left) and for the SpaCal sample in bins of $d_{\perp,clus}$ (right)

where E_h,$P_{z,h}$ and $P_{T,h}$ are the energy and the longitudinal and transversal components of the hadronic final state (HFS), respectively. The energy of the scattered electron determined with this method is given by:

$$E_{da} = \frac{2E_e \sin(\gamma_h)}{\sin(\gamma_h) + \sin(\theta_e) - \sin(\gamma_h + \theta_e)}. \tag{3.10}$$

To provide the correct reconstruction of the hadronic final state, the following selection criteria are applied in addition: $10^\circ < \gamma_h < 170^\circ$, $y_\Sigma < 0.3$ and $44 < E - p_z < 66\,\text{GeV}$ [9].

In Fig. 3.6 the double ratios $\langle E_e/E_{da}\rangle_{data}/\langle E_e/E_{da}\rangle_{MC}$ and the energy resolution for data and MC are shown. Figures 3.6 a) and b) show both quantities for the LAr sample in bins of z_{impact}. Figures 3.6 a) shows that the energy measurement is described by the MC within 1% in the full range. The energy resolution varies typically between 7% and 10%. The resolution is significantly worse at the crack at $z_{impact} \simeq -60\,\text{cm}$ (see Sec. 2.4). The resolution is well described by the MC simulation. Figures 3.6 c) and d) shows both quantities for the SpaCal sample

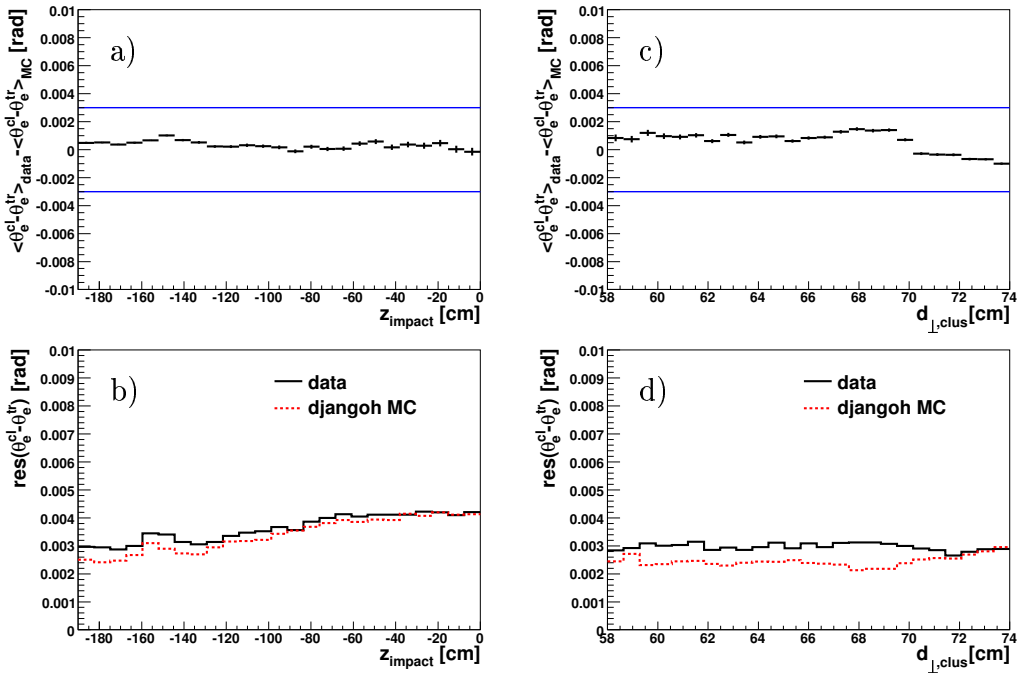

Figure 3.7: Double differences $\langle\theta_e^{cl} - \theta_e^{tr}\rangle_{data} - \langle\theta_e^{cl} - \theta_e^{tr}\rangle_{MC}$ and resolutions in $\theta_e^{cl} - \theta_e^{tr}$ for the LAr sample in bins of z_{impact} (left) and for the SpaCal sample in bins of $d_{\perp,clus}$ (right)

in bins of $d_{\perp,clus}$. The energy measurement is described by the MC within 1 %. The resolutions slightly increase from 5 % to 6.5 % towards the SpaCal edge at $d_{\perp,clus} = 74\,\text{cm}$. The resolution is described by the MC also at the edge of the SpaCal.

For the check of the θ_e measurement a vertex fitted track is matched to the calorimeter cluster with $DCA_{track-cluster} < 12\,\text{cm}$. In Fig. 3.7 the double differences $\langle\theta_e^{cl} - \theta_e^{tr}\rangle_{data} - \langle\theta_e^{cl} - \theta_e^{tr}\rangle_{MC}$ and the resolution in the difference $\theta_e^{cl} - \theta_e^{tr}$ for data and MC are shown. On the left side both quantities are shown for the LAr sample in bins of z_{impact}. The upper plot shows that the angle measurement is described by the MC within 3 mrad in the full range. The resolution (lower plot) varies typically between 2.5 mrad and 5 mrad and is well described by the MC simulation. Figure 3.7 c) and d) shows both quantities for the SpaCal sample in bins of $d_{\perp,clus}$. The θ_e measurement is described by the MC within 3 mrad. The resolution varies between 2 mrad and 3 mrad with differences between data and MC of up to ~ 30 %. There is no significant degradation in the resolution at large $d_{\perp,clus}$.

The momentum balance $p_{T,h}/p_{T,e}$ is evaluated for the inclusive selection de-

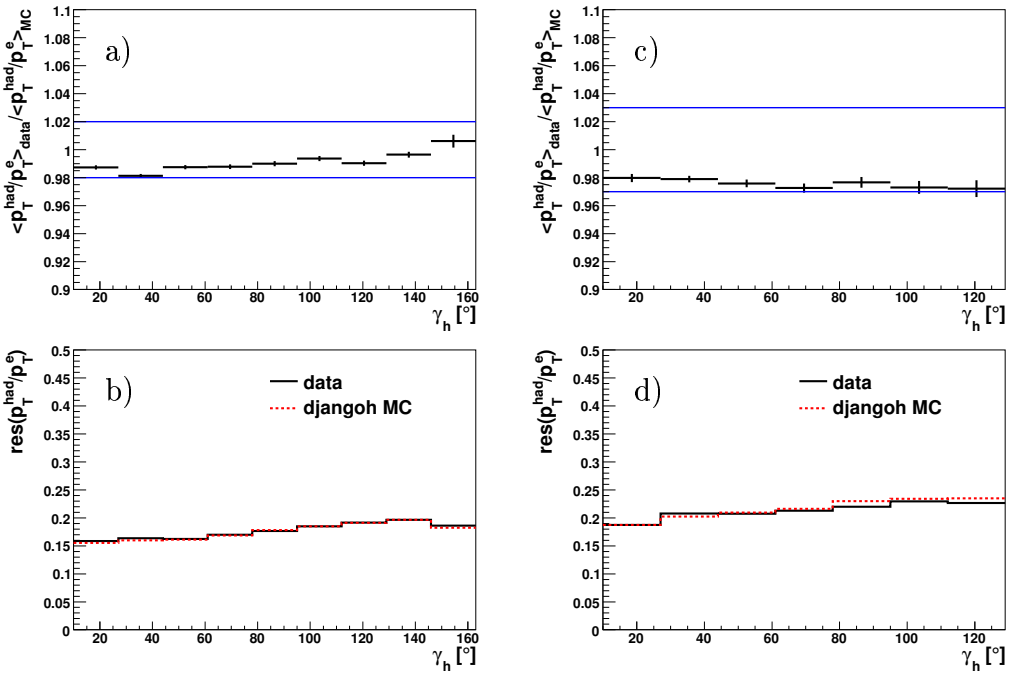

Figure 3.8: Double ratios $\langle p_{T,h}/p_{T,e}\rangle_{data}/\langle p_{T,h}/p_{T,e}\rangle_{MC}$ and resolutions in $p_{T,h}/p_{T,e}$ in bins of γ_h left for the LAr sample and right for the SpaCal sample.

scribed above to check the hadron energy calibration. In Fig. 3.8 the double ratios $\langle p_{T,h}/p_{T,e}\rangle_{data}/\langle p_{T,h}/p_{T,e}\rangle_{MC}$ and resolution in $p_{T,h}/p_{T,e}$ in bins of γ_h (see Eq. 3.9) for data and MC are shown. Fig. 3.8 a) and b) shows both quantities for the LAr sample: the hadronic energy measurement is described by the MC within 2 %; the energy resolution is nearly constant in γ_h at $\sim 15\%$ and well described by the MC. For the SpaCal sample (Fig. 3.8 c) and d)) the double ratio of the momentum balance between electron and hadronic final state is consistent with unity within an error band of 3%.

3.4.5 Trigger Efficiencies

For the determination of the trigger efficiency the analysis cuts concerning the scattered electron and the kinematics (Q^2,y) are applied as described above. Based on this sample two subsamples are defined. The analysis sample (AS), whose events are triggered by the subtrigger to be investigated and the reference sample (RS) whose events are triggered by one or more other subtriggers, which are independent

with respect to the subtrigger of interest. The trigger efficiency is then estimated as follows:

$$\epsilon_{trigg} = \frac{N(AS \wedge RS)}{N(RS)} \tag{3.11}$$

where $N(AS \wedge RS)$ is the number of events shared by both samples and $N(RS)$ the number of events in the reference sample.

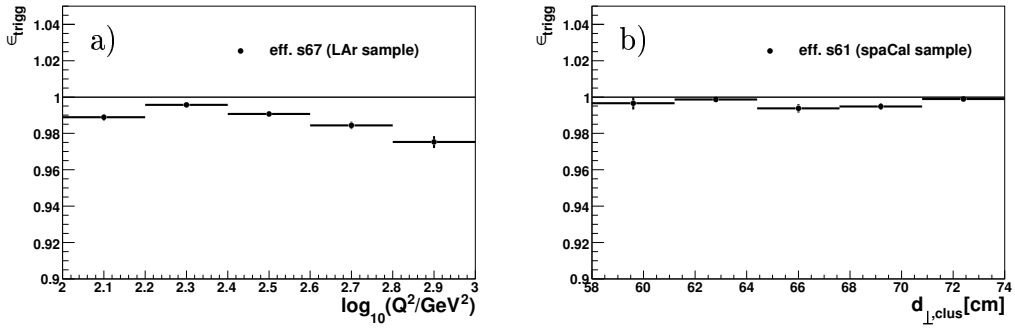

Figure 3.9: Trigger efficiency for the LAr trigger s67 in bins of $\log_{10}(Q^2)$ (a) and for the SpaCal trigger s61 in bins of $d_{\perp,clus}$ (b).

For the estimation of the trigger efficiency of s67 the subtriggers s52, s53, s55, s60, s81, s117 and s122 [92] are taken as reference since they have no LAr conditions. The efficiency is shown in bins of Q^2 in Fig. 3.9 a). The efficiency is very high ($\approx 98\%$). In the analysis, a mean efficiency of 98 % has been used.

The trigger efficiency for s61 has been estimated with the reference trigger s81 [92]. The result is shown in Fig. 3.9 b) in bins of the transverse distance of the cluster from the origin $d_{\perp,clus}$. The efficiency is larger than 99 %.

3.5 D* Selection

3.5.1 D* Reconstruction

After the inclusive DIS selection applied, as defined in the last sections, D^* mesons are reconstructed in the golden decay channel: $D^{*\pm} \rightarrow D^0\pi^{\pm}_{slow} \rightarrow K^{\mp}\pi^{\pm}\pi^{\pm}_{slow}$ (see Sec. 1.3.3). The tracks of the decay particles are reconstructed in the central tracking chambers CJC1 and CJC2. For this analysis the vertex fitted CJC tracks are used. The tracks are required to have a sufficient quality to ensure a good reconstruction of the D^* meson and background reduction. The minimum acceptable transverse momentum of the slow pion (π_s) is restricted by the magnetic field to 70 MeV. Tracks

with momenta below this value cannot be properly reconstructed in the CJC since they can hardly reach the CJC due to their high curvature as well as their interaction with the material. For the background reduction the transverse momenta of the decay particles from the D^0 candidate have to be larger than 500 MeV. Furthermore the tracks from the kaon and the pion from the D^0 candidate must have a mimimum track length of 15 cm and at least 10 CJC hits. To ensure a sufficient quality of the vertex fit for the selected tracks the cut $|dca' \cdot \sin(\theta)| < 1.5\,\mathrm{cm}$ is applied where dca' is the distance of closest approach of the corresponding non vertex fitted track with respect to the primary vertex and θ is the polar angle of the track.

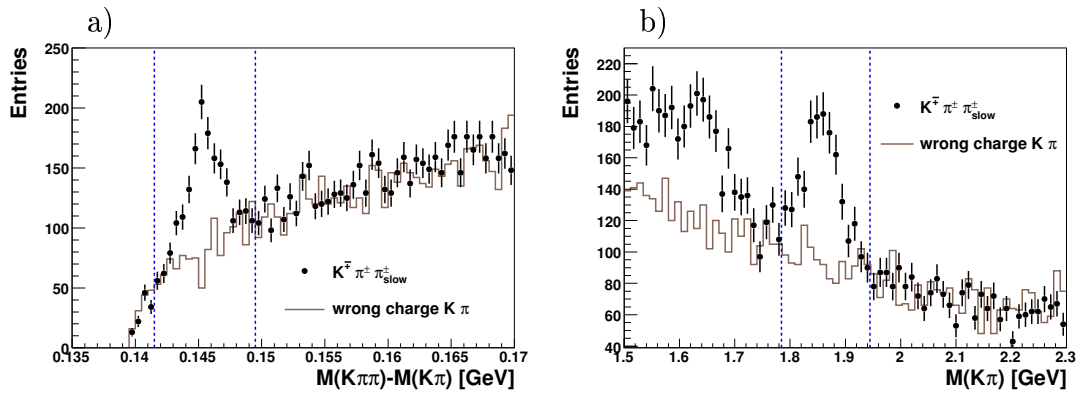

Figure 3.10: Distribution of Δm (a) and the invariant $K\,\pi$ mass (b) for the final D^* data sample. In addition the wrong charge background is plotted. The dashed lines indicate the signal regions.

The reconstruction of the D^* from the decay tracks starts with the search for the D^0 decays in a kaon and an oppositely charged pion. For this purpose the invariant mass of all combinations of two selected tracks with the mass hypothesis of a kaon and a pion respectively is estimated. The invariant mass is required to lie in a signal region of $\pm 400\,\mathrm{MeV}$ around the nominal D^0 mass $M(D^0) = 1864.5 \pm 0.4\,\mathrm{MeV}$ [41]. Under the remaining tracks the slow pion is searched for where all possible three particle combinations are taken into account and the resulting four vector of the D^* candidate is calculated. The two relevant observables deduced from the D^* meson four vector are the transverse momentum $p_t(D^*)$ and the pseudorapidity $\eta(D^*)$ given by:

$$\eta(D^*) = -\ln\left(\tan\left(\frac{\theta(D^*)}{2}\right)\right) \tag{3.12}$$

where $\theta(D^*)$ is the polar angle of the D^*. The pseudorapidity of the D^* is restricted to $|\eta(D^*)| < 1.5$ (see Sec. 3.6).

Description	Cut
Pseudo rapidity of D^*	$-1.5 < \eta < 1.5$
Transverse momentum of K,π	$p_t(K), p_t(\pi) > 0.5$ GeV
Transverse momentum of slow π	$p_t(\pi_{slow}) > 0.07$ GeV
Track type	central primary vertex fitted tracks
Track length	$l_{track}(K,\pi) > 15$ cm
Number of CJC hits	$N_{hits}(K,\pi) > 10$
Distance to vertex	$\lvert dca' \cdot sin(\theta)(K,\pi,\pi_s)\rvert < 1.5$ cm
D^0 mass window	$m(K,\pi) \in [m_{D0} \pm 0.08]$ GeV

Table 3.1: D^* selection criteria in the golden channel

A further relevant quantity is the inelasticity $z(D^*)$, which corresponds to the fraction of the photon momentum, carried by the D^* meson. The inelasticity is determined as:

$$z(D^*) = \frac{\mathbf{P} \cdot \mathbf{p_{D^*}}}{\mathbf{P} \cdot \mathbf{q}} = \frac{(E - p_z)_{D^*}}{2yE_e}, \tag{3.13}$$

where E_e is the energy of the incoming electron, P, q and p_{D^*} denote the four-momenta of the incoming proton, the exchanged photon and the observed D^* meson, respectively.

To extract the D^* signal the difference between the D^* and D^0 invariant masses is calculated:

$$\Delta M = M\left(K\pi\pi_{slow}\right) - M\left(K\pi\right). \tag{3.14}$$

The advantage of using this quantity in contrast to the invariant mass $M(K\pi\pi_{slow})$ is that the reconstruction uncertainties of the tracks of the D^0 decay particles are mostly cancelled out, so that the resolution in ΔM is almost given only by the measurement of the slow pion track. The nominal value of ΔM is 145.421 ± 0.010 MeV [41].

In Fig. 3.10 the ΔM distribution (a) and the invariant mass $M(K\pi)$ of the daughter particles of the D^0 candidates (b) are shown for the final sample including two further selection cuts as given in Sec. 3.5.2. To select D^* candidates a cut of ± 80 MeV around the nominal D^0 mass, indicated by the lines in Fig. 3.10 b), is applied. This reduces the background significantly. For the distribution of $M(K\pi)$ only D^* candidates are accepted with ΔM values in a window of ± 4 MeV around the nominal ΔM mass (lines in Fig. 3.10 a)). In the ΔM distribution the phase space threshold at the pion mass $m_\pi = 0.1395$ GeV is visible. The D^* signal is located close to the threshold at $m_{D^*} - m_{D^0} \approx 0.145$ GeV. In the $M(K\pi)$ distribution the D^0 signal is clearly visible around the nominal D^0 mass $M(D^0) = 1864.5 \pm 0.4$ MeV.

To the left of the D^0 signal a second peak is visible. This signal originates from

D^0 mesons which decay in more than two particles, but only two are reconstructed assuming the decay $D^0 \to K\pi$ for the calculation of the invariant mass.

The light-flavour background is mimicked by "wrong D" combinations $K^{\pm}\pi^{\pm}\pi^{\mp}_{slow}$, which otherwise fulfil the selection criteria. Since the kaon and the pion candidate have the same charge they do not arise from a D^0 decay. In the following this data set is referred to as "wrong charge $K\pi$" background. The background is also shown in Fig. 3.10 for both $M(D^0)$ and $\Delta M(D^*)$. The wrong charge background has the same shape in the invariant mass distributions as the combinatorial background.

All cuts concerning the selection of D^* candidates in the golden decay channel mentioned above are summarized in Tab. 3.1.

3.5.2 Background Reduction

For the background reduction the properties of the signal and the background samples are compared. For the background, the wrong charge D candidates in data are used. The signal sample is represented by a sufficient amount of MC events with at least one D^* in the golden decay channel. The MC events are reweighted in a way that the luminosity of the simulated sample corresponds to the luminosity of the data. For both samples the cuts described above are applied including the restrictions to the ΔM and $M(K,\pi)$ mass windows (see Fig. 3.10). A minimum requirement on the transverse momentum of the D^* meson $p_T(D^*) > 1.5\,\mathrm{GeV}$ is applied.

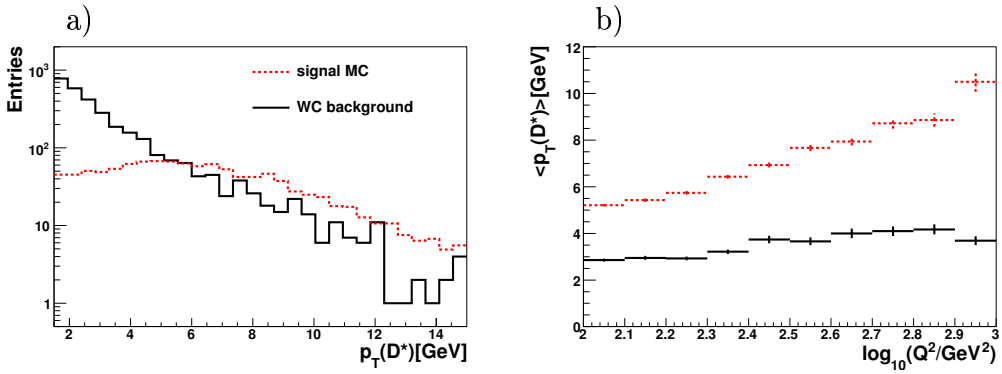

Figure 3.11: Distributions of $p_T(D^*)$ for the signal MC and the WC background sample (left) and $< p_t(D^*) >$ for signal and background in bins of $\log_{10}(Q^2)$ (right).

The $p_T(D^*)$ distributions for the signal and the background sample are shown in Fig. 3.11 a). Towards lower $p_T(D^*)$ the background increases strongly whereas the

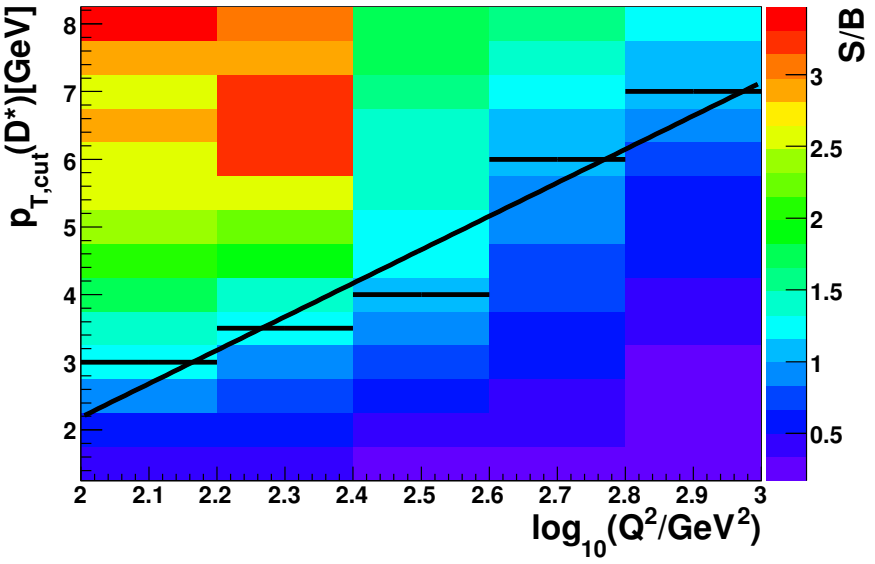

Figure 3.12: Signal to background ratio (S/B) in bins of $\log_{10}(Q^2)$ for different cuts on $p_T(D^*)$. The horizontal lines indicate for each $\log_{10}(Q^2)$ bin the minimum cut on $p_T(D^*)$ needed for $S/B > 1$. The straight line represents the fit to these values of the cut. The color code is indicated on the right.

signal distribution stays almost flat. At higher Q^2 the $p_T(D^*)$ spectra become harder due to the higher transverse boost of the event. This is apparent from Fig. 3.11 b where the mean of $p_T(D^*)$ in bins of $\log_{10}(Q^2)$ is shown. For the signal sample $< p_T(D^*) >$ increases by a factor of two towards higher Q^2. The superposition of $p_T(D^*)$ spectra from different Q^2 subranges leads to the maximum of the integrated signal distribution in Fig. 3.11 a. As a consequence of these observations a Q^2-dependent cut on $p_T(D^*)$ is applied.

For the treatment of the Q^2 dependence of the $p_T(D^*)$ cut the signal over background ratio S/B is calculated in bins of $\log_{10}(Q^2)$. Minimal values, for which the cut on the transverse momentum of the D^* meson $p_{T,cut}(D^*)$ leads to acceptable values of S/B are determined. The result is shown in Fig. 3.12. It is clear that that the cut on $p_T(D^*)$ needed for a constant S/B increases with $\log_{10}(Q^2)$. As a starting point for the optimisation of this cut a signal to background ratio $S/B = 1$ is aimed for. To the values of $p_{T,cut}(D^*)$ thus obtained a straight line is fitted to define the cut:

$$\frac{p_t(D^*)}{GeV} > A \log\left(\frac{Q^2}{100\,\mathrm{GeV}^2}\right) + B. \tag{3.15}$$

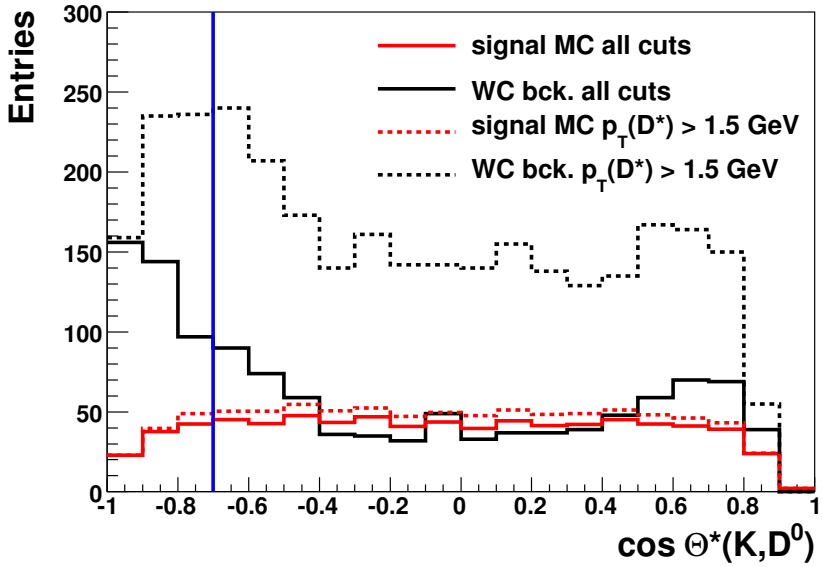

Figure 3.13: Distributions of $cos\Theta^*(K, D^0)$ for the signal and background sample. Shown are the distributions obtained with all other cuts applied (solid lines) as well as for $p_T(D^*) > 1.5\,\mathrm{GeV}$ (dashed lines). The vertical line indicates the cut $cos\Theta^*(K, D^0) > -0.7$ applied in the analysis.

The cut is optimised such that a minimal fraction of the signal is lost due to the cut, since for the definition of the visible range a lower cut namely $p_T(D^*) > 1.5\,\mathrm{GeV}$ was defined (see Sec. 3.6). A cut according to Eq. 3.15 with $B = 2$ but a lower slope $A = 3$ instead has been chosen, which results in less than 20% events lost within the visible range for all $\log_{10}(Q^2)$ bins.

A further background rejection is achieved by a restriction on $\cos\Theta^*(K, D^0)$ where $\Theta^*(K, D^0)$ is the angle between the kaon candidate and the D^0 flight direction in the D^0 rest frame. The distribution of $\cos\Theta^*(K, D^0)$ for both samples is shown in Fig. 3.13. The solid lines show the distributions of $\cos\Theta^*(K, D^0)$ of the selected D^* candidates after the Q^2-dependent $p_t(D^*)$ cut. For the signal sample the distribution is almost flat since the D^0 is a pseudoscalar decaying isotropically. The drop of the distribution at $|cos\,\Theta^*(K, D^0)| > 0.8$ is due to the p_t cuts on the decay tracks which is obvious since in this region one decay particle moves nearly opposite to the D^0 flight direction with a lower transverse momentum in the laboratory frame. For the background sample a strong increase of the $cos\,\Theta^*(K, D^0)$ distribution to low values is visible. In this region the kaon moves opposite to the D^0

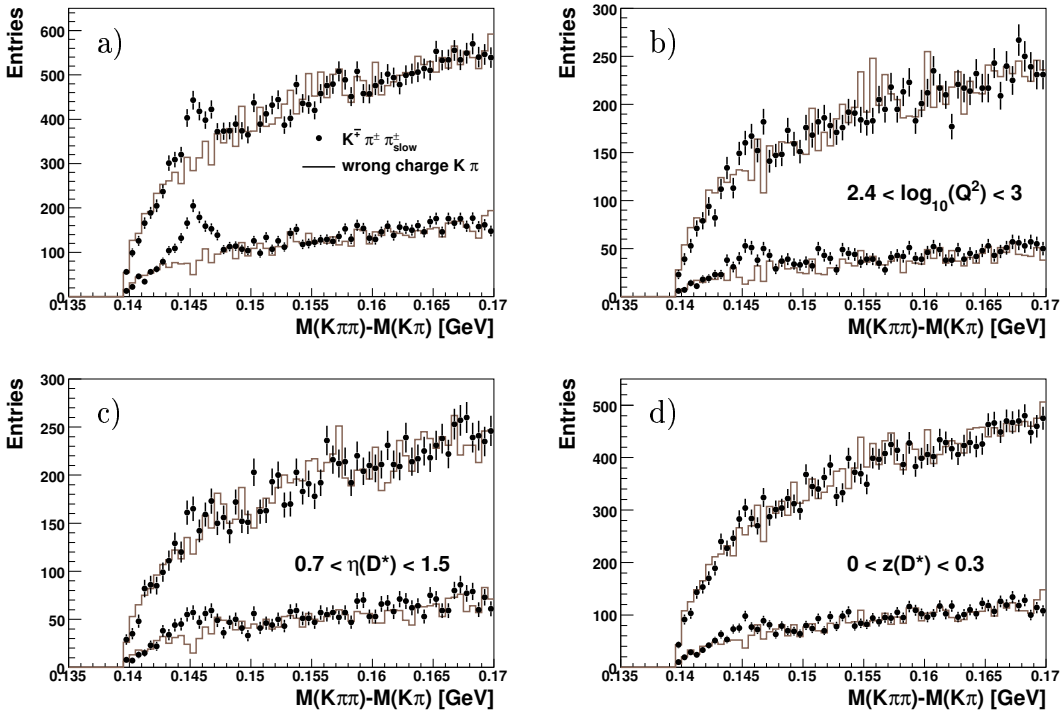

Figure 3.14: Comparison of the ΔM spectra with and without the two background rejection cuts discussed in this chapter. In a) the spectra for the total sample are shown. In b)-d) the same comparison is made for selected kinematical bins where the background is expected to be higher.

with lower $p_t(K)$ compared to the central region of $cos\,\Theta^*(K, D^0)$, and hence more pions are misidentified as kaons. Consequently $cos\,\Theta^*(K, D^0) > -0.7$ is required in this analysis.

Fig. 3.13 also shows the distributions of $cos\,\Theta^*(K, D^0)$ for both samples with $p_t(D^*) > 1.5\,\mathrm{GeV}$ (dashed lines). Whereas the signal distribution changes only slightly, the background increases significantly up to a factor of four in the central region. These distributions show that the cut on $cos\,\Theta^*(K, D^0)$ is useful, but cannot replace the requirement on $p_t(D^*)$ used for background rejection.

The effect of the selection criteria described above is shown in Fig. 3.14 where the ΔM distributions (right and wrong charge) with and without the two cuts are plotted. The reduction of the background is clearly visible. In Fig. 3.14 a) the total sample is shown. In Fig. 3.14 b)-d) the data are compared for some subregions of the phase space where in general the combinatorial background is expected to

be higher. Fig. 3.14 b) shows the distributions for higher Q^2, $2.4 < \log_{10}(Q^2) < 3$. Without the requirement on $cos\Theta^*(K, D^0)$ and the Q^2-dependent $p_t(D^*)$ cut a signal at $\Delta M \approx 0.145\,\text{GeV}$ is hardly visible, while after applying the cuts a clear signal can be identified. Fig. 3.14 c) shows the distributions for the forward region of the detector $0.7 < \eta(D^*) < 1.5$. Only after applying the background rejection cuts a signal extraction is possible. The same holds for low D^* inelasticities $z(D^*)$ $0 < z(D^*) < 0.3$ (Fig. 3.14 d)).

3.5.3 Control Distributions

In order to ensure that the MC samples used to correct the data for detector effects, describe the data sample, different physics observables in data and MC are compared in detail. The final selection criteria are applied, in addition only events in a window of $\pm 2.5\,\text{MeV}$ around the nominal ΔM position are taken into account to assure background suppression.

In the differential distributions for D^* meson production in the data the wrong charge background is statistically subtracted from the right charge distributions. In contrast to the wrong charge background, the right charge background contains a contribution of real D^0 mesons, not originating from D^*. Therefore the wrong charge background is slightly lower in normalization than the right charge background. To take this effect into account the wrong charge distributions are normalized by a factor which is determined using all D^* candidates above the signal region ($0.152 < \Delta M < 0.17\,\text{GeV}$). This factor is 1.04.

The data are compared with the predictions from RAPGAP and CASCADE on the reconstruction level. The MC events are reweighted for the z-vertex (Sec. 3.3) and normalized to the data according to the luminosity. In order to describe the data both MC samples have to be further reweighted. The simulated events from RAPGAP are reweighted in Q^2 whereas the CASCADE predictions are reweighted in $p_t(D^*)$. Further details are given in Sec. 4.3.3.

Fig. 3.15 shows the data/MC comparison of the variables characterizing the DIS event. The data distributions of $\log_{10}(Q_e^2)$ and $y_{e\Sigma}$ are described well by both predictions except for some outliers in the $y_{e\Sigma}$ distribution which could be statistical fluctuations. Negative values of the $N(D^*)$ in some kinematic bins e.g. in the $\log_{10}(Q_e^2)$ distribution occur due to the statistical subtraction of the wrong charge background. A good description of the data is also obtained for the electron energy E'_e, the polar angle of the electron θ_e, the z-vertex distribution and the longitudinal momentum balance of the event $E - p_z$. The latter distribution peaks at nearly $55\,\text{GeV}$ but is asymmetric to lower values due to loss of hadrons in the forward direction.

Fig. 3.16 shows the control distributions for the D^* kinematic variables $p_t(D^*)$, $\eta(D^*)$ and $z(D^*)$. All distributions of the data are reasonably well described by the

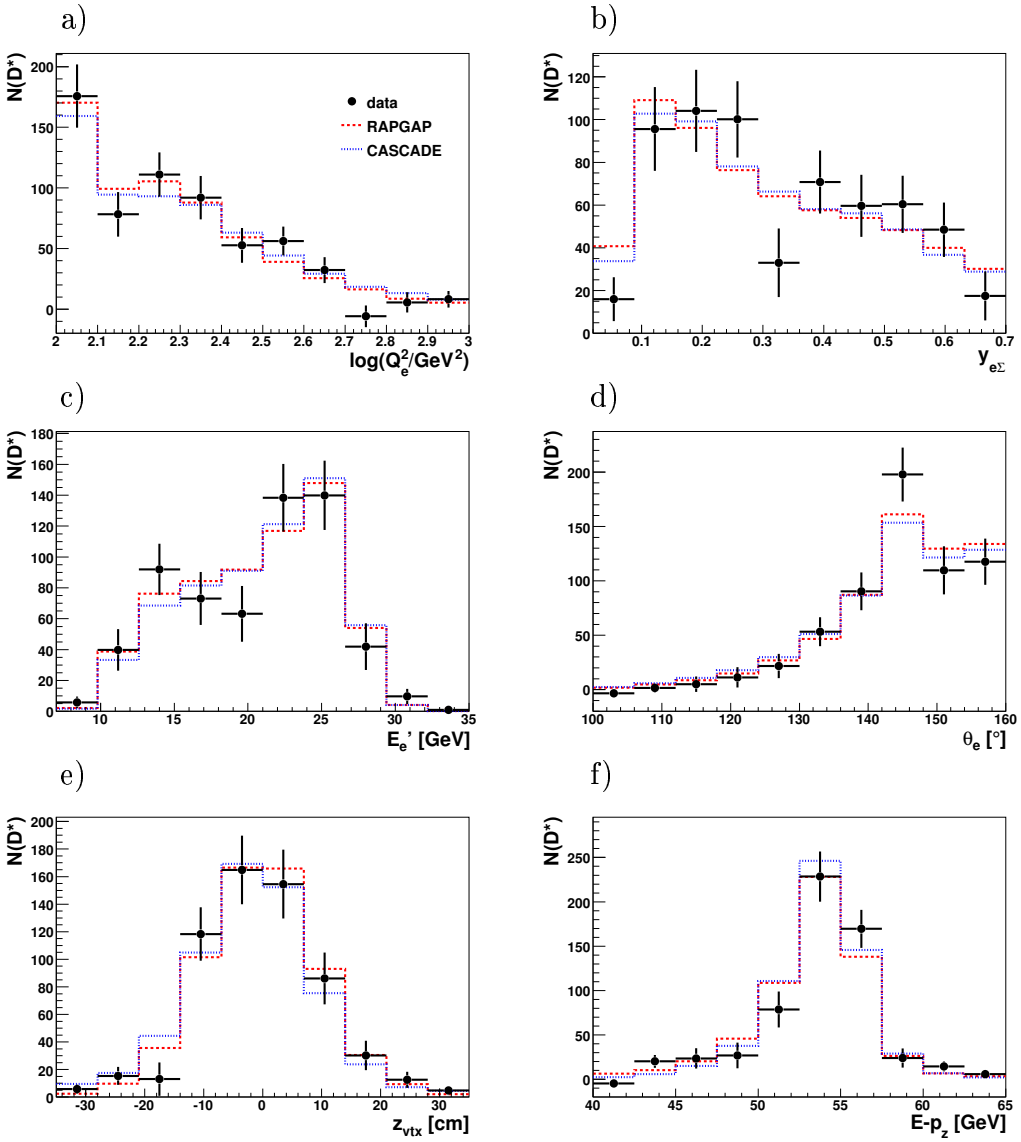

Figure 3.15: Control distributions of the quantities $\log_{10}(Q_e^2)$, $y_{e\Sigma}$, E'_e, θ_e, z_{vtx} and $E - p_z$. For the data the wrong charge background has been subtracted statistically. The simulated events from RAPGAP are reweighted in Q^2 whereas the CASCADE predictions are reweighted in $p_t(D^*)$ as described in Sec. 4.3.3.

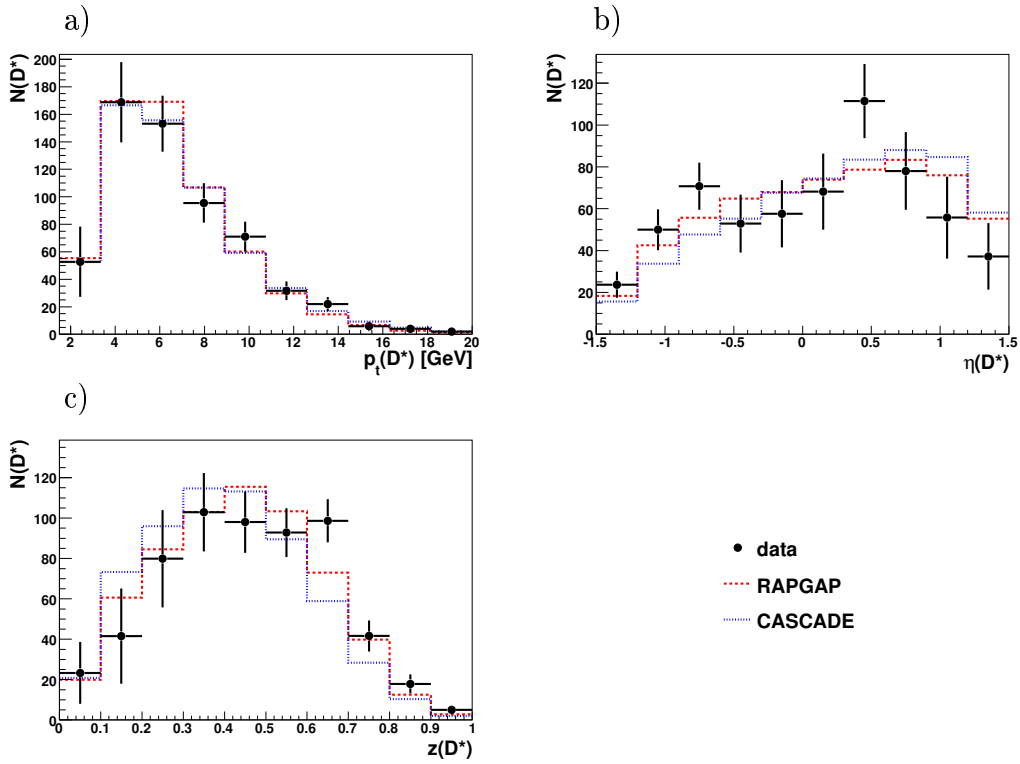

Figure 3.16: Control distributions of the D^* related quantities $p_t(D^*)$, $\eta(D^*)$ and $z(D^*)$. For the data the wrong charge background has been subtracted statistically. The simulated events from RAPGAP are reweighted in Q^2 whereas the CASCADE predictions are reweighted in $p_t(D^*)$ as described in Sec. 4.3.3.

MC predictions except $z(D^*)$ where the predicted spectra especially in case of CASCADE tend to be softer than in the data. The decrease of the $p_t(D^*)$ distributions to low values is due to the Q^2 dependent $p_t(D^*)$ cut. The $\eta(D^*)$ spectrum indicates that for the phase space covered by this analysis the sample is dominated by events with most activity in the forward direction.

Fig. 3.17 shows control distributions for the transverse momenta $p_t(K, \pi, \pi_{slow})$ and polar angles $\theta(K, \pi, \pi_{slow})$ of the decay particles. All data distributions are well described by the predictions. Note that the typical transverse momenta of the slow pion are lower by an order of magnitude in comparison to the D^0 daughter particles. Since the transverse momenta of the slow pion and the D^* are strongly correlated due to the small mass difference between the D^* and D^0, the $p_t(D^*)$ cut causes also a decrease in the $p_t(\pi_{slow})$ spectrum towards lower transverse momenta. The difference in the slope of the p_t-spectra for K and π at low values arises from the

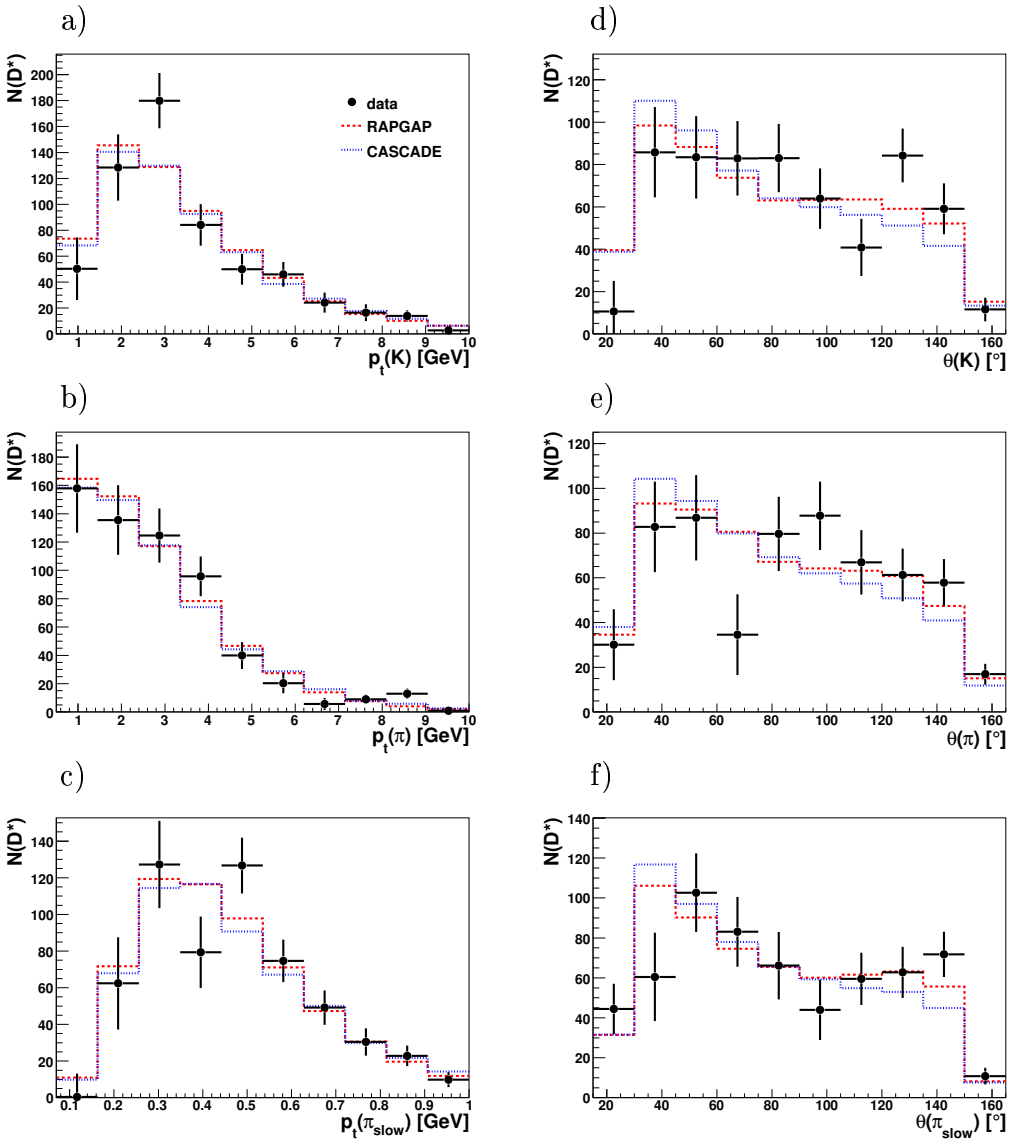

Figure 3.17: Control distributions for the transverse momenta $p_t(K, \pi, \pi_{slow})$ and polar angles $\theta(K, \pi, \pi_{slow})$ of the decay tracks. For the data the wrong charge background has been subtracted statistically. The simulated events from RAPGAP are reweighted in Q^2 whereas the CASCADE predictions are reweighted in $p_t(D^*)$ as described in Sec. 4.3.3.

$\cos\theta^*(K, D^0)$ cut which affects mostly D^0 mesons with kaons at lower transverse momenta. The distributions of the polar angles of the decay tracks $\theta(K, \pi, \pi_{slow})$ tend to the forward direction and show the limited acceptance of the CJC at small and large polar angles.

3.6 Definition of the Visible Range

The measurement of the cross sections for D^*-meson production is restricted to a certain region of the kinematic phase space. The measurement is performed in the range of the photon virtuality of $100\,\mathrm{GeV}^2 < Q^2 < 1000\,\mathrm{GeV}^2$. Thus, the test of theory models of charm production at high Q^2 is possible. Above Q^2 of 1000 the statistics of D^* production becomes too insignificant.

Description	Cut
photon virtuality	$100 < Q^2 < 1000$ GeV^2
inelasticity	$0.02 < y < 0.7$
pseudorapidity of D^*	$-1.5 < \eta(D^*) < 1.5$
transverse momentum of D^*	$p_t(D^*) > 1.5$

Table 3.2: Definition of the visible range of the measurement

Further restrictions on the kinematic phase space are necessary due to the limited acceptance of the H1 detector and to ensure reasonable reconstruction properties. The restrictions are chosen to be consistent with the D^* analysis [86] at medium Q^2:

- The inelasticity y is restricted to a region of $0.02 < y < 0.7$ to ensure a good quality of of the reconstruction of the kinematic variables. The upper boundary on y is consistent with the restriction on the energy of the scattered electron $E'_e > 8\,\mathrm{GeV}^2$.

- The range of the pseudorapidity $\eta(D^*)$ is defined by $-1.5 < \eta(D^*) < 1.5$ to account for the limited acceptance of the central tracking chambers in η for the reconstruction of the tracks of the decay particles.

- The transverse momentum $p_t(D^*)$ of the D^* has to be larger than 1.5 GeV. For smaller $p_t(D^*)$ the mean transverse momentum of the slow pion is too small for an efficient reconstruction in the central tracking detector[5]. Since a harder cut on $p_t(D^*)$ according Eq. 3.15 is applied within this analysis an extrapolation in $p_t(D^*)$ for the calculation of the cross sections in the visible range has to be

[5]Extensions of the phase space to lower $p_t(D^*)$ have been studied in Ref. [86]

done. This is considered, during the calculation of the reconstruction efficiency (see Sec. 4.3).

The visible range for the present analysis is summarized in Tab. 3.2.

Chapter 4

D* Cross Section Measurement

This chapter is devoted to the D^* cross section measurement[1]. To determine the cross section the number of D^* mesons in the different kinematic bins is extracted from the fit to the ΔM distributions. The reconstruction efficiencies are estimated using the MC. The radiative corrections are applied to correct the measured cross sections to the Born level. Contributions of other D^* decay channels to the signal distributions have been investigated and are corrected for. The last part of this chapter describes the systematic uncertainties.

4.1 Determination of the Cross section

The visible D^* production cross section is calculated as follows:

$$\sigma^{vis} = \frac{N(D^*)\,(1-R)}{\mathcal{L}\,\mathcal{B}(D^* \rightarrow K\pi\pi_s)\,\epsilon_{rec}\,\epsilon_{trigg}\,(1+\delta_r)}\ . \tag{4.1}$$

Here $N(D^*)$ is the number of D^* in a certain kinematic bin, $\mathcal{L} = 351 \pm 11\,\mathrm{pb}^{-1}$ is the luminosity, $\mathcal{B} = 2.63 \pm 0.04\%$ [93] the branching ratio for the studied decay and ϵ_{rec} is the total reconstruction efficiency. For the estimation of $N(D^*)$ and ϵ_{rec} the cuts according chapter 3 like the cut around the nominal D^0 mass are applied on reconstruction level. The efficiency ϵ_{rec} is calculated in the visible range of the analysis as given in Sec. 3.6. The trigger efficiency ϵ_{trigg} has been extracted from data as described in Sec. 3.4.5. The contributions of other decay channels than the one studied amount to $R = (4.4 \pm 0.5)\%$ (see Sec. 4.5). Finally, in order to correct the measured visible cross sections to the Born level, corrections for initial and final state QED radiation have to be applied. The corresponding correction δ_r, varying between 2 and 5%, is evaluated using the MC with and without radiative corrections.

[1] In the following D^* is used to denote both D^{*+} and D^{*-}.

The single differential cross sections are measured as a function of the observables Q^2, x, $p_t(D^*)$, $\eta(D^*)$, $z(D^*)$ and $p_t^*(D^*)$. For the comparison with the ZMVFNS calculation an additional cut on the transverse momentum of the D^* in the photon-proton centre of mass frame, $p_t^*(D^*)$, is applied.

4.2 Signal Extraction

The number of D^* mesons in each kinematic bin is determined from the fit of the ΔM distribution. The number of D^* is then extracted via integration of the signal function. The natural linewidth of the D^* is $\Gamma_{tot}(D^*) = 96 \pm 22\,\mathrm{keV}$ [93]. The width of the ΔM peak is determined by the detector resolution. As the mass difference method is applied, the resolution is dominated by the measurement of the π_s track in the detector. Different effects contribute to the resolution of the π_s track. Multiple scattering and the limited number of z measurements of the tracks are the dominant contributions. Concerning the z measurement the resolution varies with the number of hits in the track chambers. The presence of a precise z measurement from the COZ plays an important role. It has been shown [94] that the superposition of the contributions of the mentioned effects results in a ΔM signal distribution with a small asymmetric tail on the right side. The same effect can be seen in Fig. 4.1 for the simulated D^* mesons. At high Q^2, in data this tail is not clearly visible due to the limited statistics. For both data and MC the asymmetric "Crystal Ball" function [94, 95] is used to describe the signal:

$$f_{sig}(\Delta M) = N \cdot \begin{cases} \exp\left(-\frac{1}{2}\left(\frac{\Delta M-\mu}{\sigma}\right)^2\right) & if\ \frac{\Delta M-\mu}{\sigma} \leq -\alpha \\ \frac{\left(\frac{n}{|\alpha|}\right)^n \exp\left(-\frac{1}{2}\alpha^2\right)}{\left(\frac{n}{|\alpha|}-|\alpha|+\frac{\Delta M-\mu}{\sigma}\right)^n} & if\ \frac{\Delta M-\mu}{\sigma} > -\alpha \end{cases} \tag{4.2}$$

It consists of a gaussian distribution with the peak position μ and width σ and a power law on the right, with the parameters α and n. The asymmetry parameter α is choosen as $\alpha < 0$ and $|\alpha|$ denotes the position in ΔM relative to μ in multiples of σ where the power law starts. At the transition point the function itself and its first derivative are both continuous. N denotes the normalisation factor. The parameter n is fixed to 120 for the data and to 10 for the MC to optimize the convergence speed of the fit [94]. This optimal values are different for data and MC since the background in MC has a completely different shape (see Fig. 4.1) than in data and therefore a different background parametrisation for the fit is used which on the other hand changes the convergence behavior of the fit. But it has been shown in [94] that the number of D^* mesons obtained from the fit changes only within 0.2% for different values of n below a critical value of $n_{cr} = 145$. For $n > n_{cr}$ the fit does not converge anymore.

For the description of the background shape the Granet-Parametrisation [96] has been used:

$$f_{bck,da}(\Delta M) = p_0 \cdot (\Delta M - m_\pi)^{p_1} \cdot \exp\left(-p_2 \Delta M - p_3 (\Delta M)^2\right). \qquad (4.3)$$

Here m_π is the mass of the charged pion which determines the phase space threshold, the parameter p_0 is the normalisation and $p_1 - p_3$ describe the shape of the background. It turned out that the first exponential damping factor in Eq. 4.3 can be used alone to describe the background behavior at large ΔM. Therefore p_3 is set to zero.

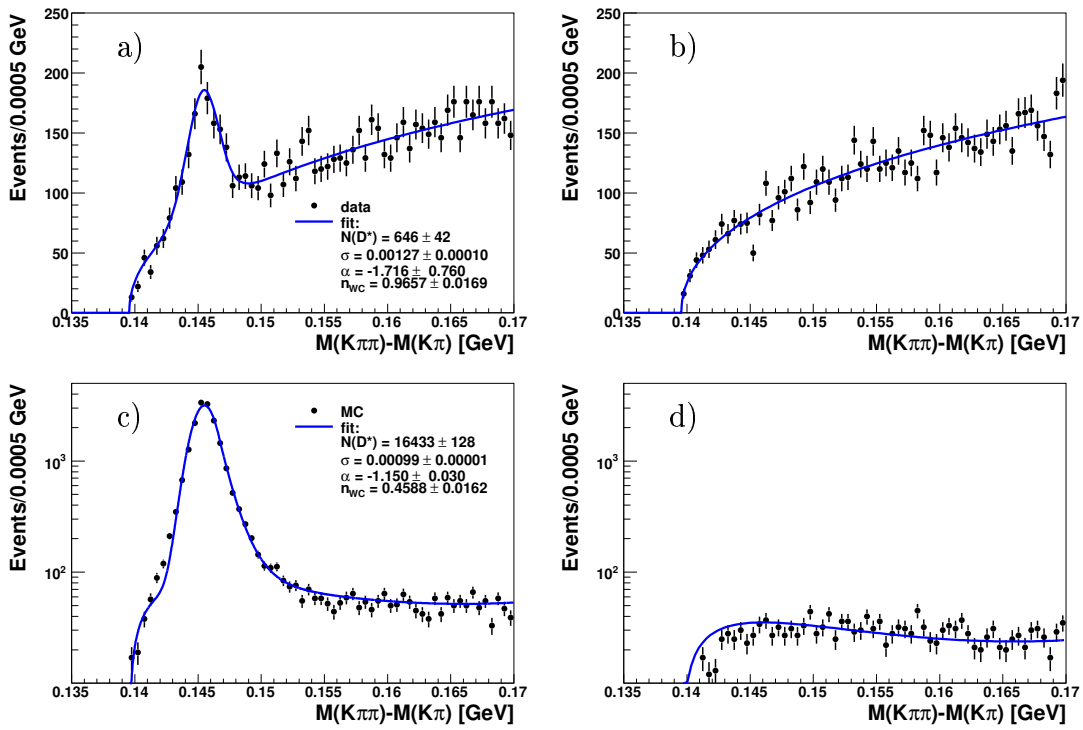

Figure 4.1: Fitted ΔM spectra for right and wrong charge. Shown are the distributions for data (a,b) and MC (c,d) for the complete phase space each. The MC spectra are displayed with a logarithmic scaling.

The shape of the background in the case of the signal MC is completely different in comparison to the data (see Fig. 4.1). Since in each event at least one generated D^* meson is required, the background is much lower than in data as well as the increase of the background at large ΔM is less distinct. Therefore a different parametrisation of the background is used in case of the signal MC [94]:

$$f_{bck,MC}(\Delta M) = p_0 \cdot (\Delta M - m_\pi)^{p_1} \cdot \exp\left(-p_2 (\Delta M - m_\pi) - p_3 (\Delta M - m_\pi)^2\right) \quad (4.4)$$

This expression is similar to Eq. 4.3 except for the shift of the exponential function to the right by m_π. Here all three parameters p_1, p_2 and p_3 (and p_0) are kept free.

The fit to the data is performed simultanously to the right and wrong charge data set with the function:

$$f_{fit}(\Delta M, \Delta M') = f_{sig}(\Delta M) + f_{bck}(\Delta M) + n_{WC} \cdot f_{bck}(\Delta M') \tag{4.5}$$

where ΔM and $\Delta M'$ are the mass difference values of the right and wrong charge distributions respectively. The parameters of the background functions for the right and wrong charge sample are the same. The relative normalisation factor n_{WC} between right and wrong charge distributions is kept free during the fit. This procedure has been choosen to use all available information for determining the background shape.

Fig. 4.1 shows the result of the fit to the inclusive sample for the data (a,b) and MC (c,d). The wrong charge sample is shown on the same scale as right charge data. The MC-data in Fig. 4.1 *c)* and *d)* are displayed on a logarithmic scale since the background is about two orders of magnitude smaller than the signal. The wrong charge background in MC is nearly a factor of two smaller than the right charge background ($n_{WC} = 0.46 \pm 0.01$) since in the MC at least one real D^0 exists in each event.

For fitting the distributions the software package "RooFit" [97] is used. The parameters are determined by a negative Log-Likelihood (NLL) fit to the values of the unbinned distribution. For the minimization MINUIT [98] is used. For comparison a NLL fit to the binned distributions has been performed. The difference in $N(D^*)$ between the binned and the unbinned fit results is smaller than 0.3%.

Since the analysis sample is statistically limited, the fit parameters σ and α are fixed in the kinematic bins. In this way, the fit is more stable and the statistical error on $N(D^*)$, which is in the most bins the dominant uncertainty of the measurement, is reduced. The latter is achieved since the normalisation and other parameters especially the width are correlated with each other. An additional systematic error on the cross sections is calculated to account for the fixing of the fit parameters.

For a fit to the data in the individual bin i the parameters σ and α are fixed to values $\sigma_{i,fix} = c_\sigma \sigma_{i,MC}$ and $\alpha_{i,fix} = c_\alpha \alpha_{i,MC}$. Here $\sigma_{i,MC}$ and $\alpha_{i,MC}$ are the values obtained from fit to the MC distributions with much higher statistics. The global correction factors $c_\sigma = \sigma_{tot,data}/\sigma_{tot,MC}$ and $c_\alpha = \alpha_{tot,data}/\alpha_{tot,MC}$ are calculated as the ratio of the parameters obtained from the fit to the inclusive sample in data and MC respectively. Hence by applying these both global correction factors a first order correction of the MC prediction used for fixing is applied. In Fig. 4.1 the fitted width and tail parameter for the total sample are given: $\sigma_{tot,data} = 1.26 \pm 0.10\,\text{MeV}$, $\sigma_{tot,MC} = 0.99 \pm 0.01\,\text{MeV}$, $\alpha_{tot,data} = -1.71 \pm 0.76$ and $\alpha_{tot,MC} = -1.15 \pm 0.03$. The global correction factors are therefore: $c_\sigma = 1.27 \pm 0.10$ and $c_\alpha = 1.49 \pm 0.66$.

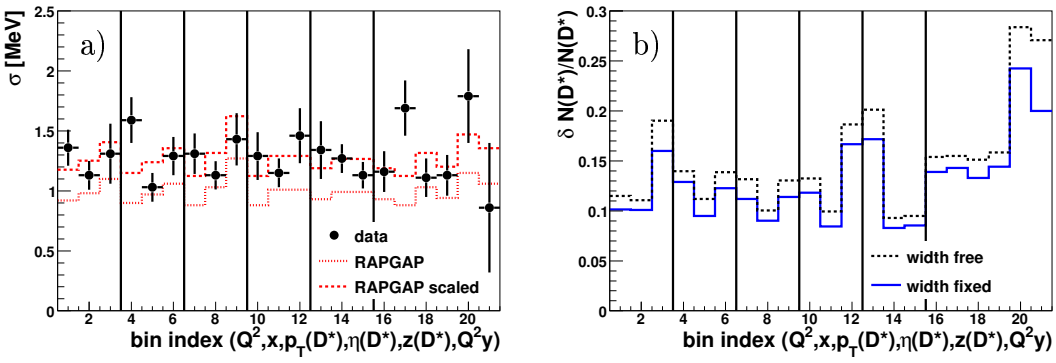

Figure 4.2: Fitted widths in the data and MC as well as the global shifted widths used for fixing. In b) the relative statistical errors in the number of D^* in each bin in comparison with and without fixing the width are shown.

In Fig. 4.2 a) the measured widths in the individual bins for data $\sigma_{i,data}$, MC $\sigma_{i,MC}$ and the fixed values $\sigma_{i,fix}$ are shown. The x-axis represents the bin numbers where the horizontal slices group the bins belonging to the same kinematical distribution. The cross sections are measured single differential in Q^2, x, $p_t(D^*)$, $\eta(D^*)$ and $z(D^*)$ with three bins each. The last slice in Fig. 4.2 corresponds to the bins for the double differential cross section measurement in Q^2 and y with three bins in Q^2 and two in y. The fitted values in MC (dotted line) vary from bin to bin especially in the case of $p_T(D^*)$ with a change of about 40% from the first to the last bin. The widths obtained from data are in most of the bins compatible with the fixed values $\sigma_{i,fix}$ with some outliers especially the first x bin and the second Q^2, y bin. Fig. 4.2 b) shows the relative statistical errors $\delta N(D^*)/N(D^*)$ for each bin in comparison with and without fixing the width. Due to the fixing of the width the relative statistical error decreases by $10\% - 25\%$. The largest relative errors appear in the phase space with high background contribution, e.g. high Q^2, high η and low z.

4.3 Reconstruction Efficiencies

For the calculation of the cross sections according to Eq. 4.1 the total reconstruction efficiency ϵ_{rec} has to be estimated for each kinematical bin. The geometric acceptance, the efficiency and the resolutions of the relevant detector components are considered. The efficiencies are calculated using the MC simulations RAPGAP and CASCADE by comparing the events on generator level (gen) with the events on the reconstruction level (rec) after passing through the detector simulation and applying the same reconstruction software as for the data. The efficiencies and migrations

are to be taken into account properly, therefore a good description of the data by the simulation is mandatory. For this purpose the MC samples are reweighted.

4.3.1 Unfolding of Detector Effects

In general a measured distribution y in N bins is related to the true distribution x by applying the response matrix

$$y_i = \sum_{j=1}^{N} \mathbf{A}_{ij} \cdot x_j \ , \tag{4.6}$$

In this matrix the detector effects are taken into account. For simplicity, for the true and the reconstructed distribution the same binning is assumed. The matrix can be determined from MC using the reconstructed and the generated quantities. Under the assumption that the MC describes the detector response correctly, the true distribution from the data can be estimated according Eq. 4.6 using the inverted response matrix. Matrix inversion has well known general problems and is therefore called mathematically and statistically "ill-posed" since a small perturbation of the data can cause an arbitrary large perturbation of the solution [99]. The true distribution x_j can be obtained with different mathematically sophisticated methods [99] that overcome inversion problems. These methods are not really applicable for distributions with a small number of bins like in this analysis. Here the so called bin-by-bin unfolding is used assuming that the response matrix $\mathbf{A}$ is almost diagonal with the migrations between the bins being small enough.

In the bin-by-bin unfolding the true D^* distribution is therefore calculated according Eq. 4.1 for each bin by dividing the measured number of D^*-mesons by the reconstruction efficiency ϵ_{rec} in that particular bin. For the efficiency calculations with the MC two samples are considered. In the generated sample the visibility cuts according Sec. 3.6 are applied. In the reconstructed sample the same selection criteria as in the data are applied. The efficiency in a bin i is then calculated as follows:

$$\epsilon_{i,rec} = \frac{N_{i,rec}}{N_{i,gen}} \tag{4.7}$$

where $N_{i,gen}$ is the number of the generated D^* mesons in the bin and accordingly $N_{i,rec}$ the number of the reconstructed D^* candidates. The number of generated D^* is determined by counting, the number of the reconstructed D^* is determined from the fit to the ΔM distribution as shown in Fig. 4.1.

For each bin the purity P is calculated as follows:

$$P_i = \frac{N_{i,gen \wedge rec}}{N_{i,rec}} \tag{4.8}$$

where $N_{i,gen \wedge rec}$ is the number of reconstructed D^* in a bin i where the D^* meson was generated. In case of no migrations the purity is 1 otherwise the value is lower.

4.3.2 Estimated Efficiencies and Purities

The reconstruction efficiency for the total sample amounts to 29% for RAPGAP and to 31% for CASCADE. The values for the individual bins are shown in Fig. 4.3 a). The efficiency varies from 25% to 40% from bin to bin. In the first Q^2 bin, the efficiency is lower due to the acceptance gap between LAr and SpaCal calorimeters. The lower efficiency at low $p_t(D^*)$ can be explained by the p_t requirement for the decay tracks of the D^0 and the correlation of $p_t(D^*)$ with Q^2. For the cross section determination the average of the efficiencies obtained with RAPGAP and CASCADE is taken.

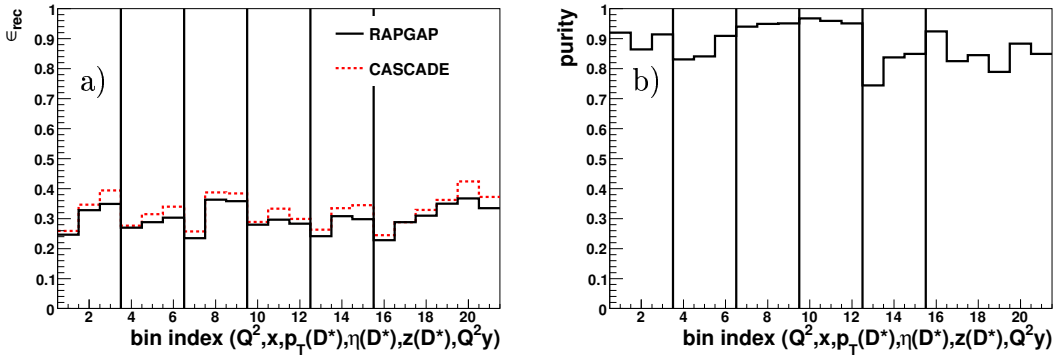

Figure 4.3: Reconstruction efficiencies ϵ_{rec} (a) and purities (b) for the individual bins.

In Fig. 4.3 b) the purities for the individual bins are shown. The lowest value in the first $z(D^*)$ bin is larger than 70%. In all other bins the purities exceed 80%. In the $p_t(D^*)$ and $\eta(D^*)$ bins the purity is $> 95\%$.

4.3.3 Monte Carlo Reweighting

For an accurate efficiency estimation the MC samples has to describe the data. In addition to the z-vertex reweighting as described in Sec. 3.3 further reweighting in kinematics has to be done.

For the MC samples the Bowler fragmentation function (Eq. 1.37) is used with parameters adopted from e^+e^- measurements of the fragmentation function [100]. The fragmentation function in $ep \to eD^*X$ processes was measured at H1 [40]. According to this measurement the value of the extracted Kartvelishvili fragmentation

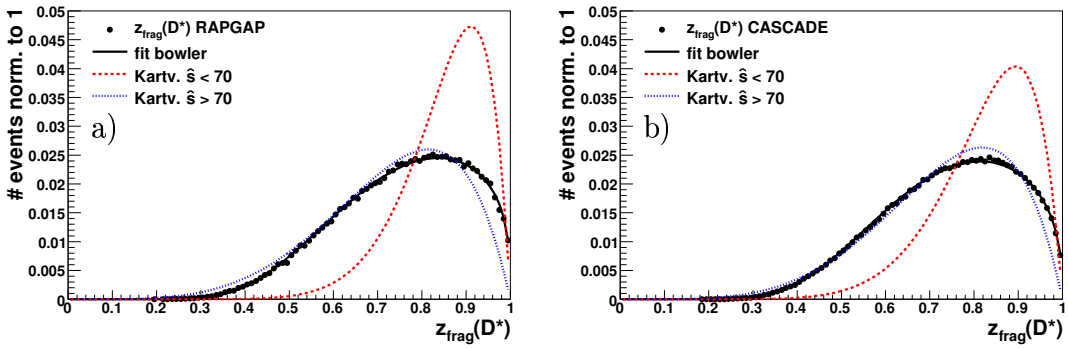

Figure 4.4: Spectrum of z_{frag} for RAPGAP (a) and CASCADE (b) according the standard Bowler fragmentation together with the measured Kartvelishvili spectra for the two $\hat{s}$ regions.

parameter depends strongly on the photon-gluon centre-of-mass energy $\hat{s}$. There are two regions distinguished in the analysis: the region where the D^* mesons are produced close to the production threshold (low $\hat{s}$) or far above the threshold (high $\hat{s}$). In the measurement [40] the two regions are distinguished by demanding or rejecting the presence of a jet containing a D^* with a transverse momentum above a certain threshold which corresponds to $\hat{s} \approx 70\,\mathrm{GeV}^2$. The measured fragmentation parameter α depends also on the QCD models used for comparison of the fragmentation distribution with the data. The values obtained for RAPGAP and CASCADE in the different $\hat{s}$ regions are given in Tab. 4.1.

Model	α Kartvelishvili	
	$\hat{s} < 70\,\mathrm{GeV}^2$	$\hat{s} > 70\,\mathrm{GeV}^2$
RAPGAP	$\alpha = 10.3^{+1.9}_{-1.6}$	$\alpha = 4.4^{+0.6}_{-0.5}$
CASCADE	$\alpha = 8.4^{+1.3}_{-1.1}$	$\alpha = 4.5^{+0.6}_{-0.6}$

Table 4.1: Kartvelishvili fragmentation parameters for RAPGAP and CASCADE measured by H1.

In Fig. 4.4 the distributions of the fragmentation variable z_{frag} for RAPGAP (a) and CASCADE (b) are shown. A fit using a Bowler parametrisation according Eq. 1.37 f_{bowler} is also shown. In addition the Kartvelishvili parametrisation f_{meas} using parameters α according Tab. 4.1 (central values) for both $\hat{s}$ regions are shown. The longitudinal part of the fragmentation function is reweighted according to the Kartvelishvili parametrisation by weighting the generated fragmentation variable

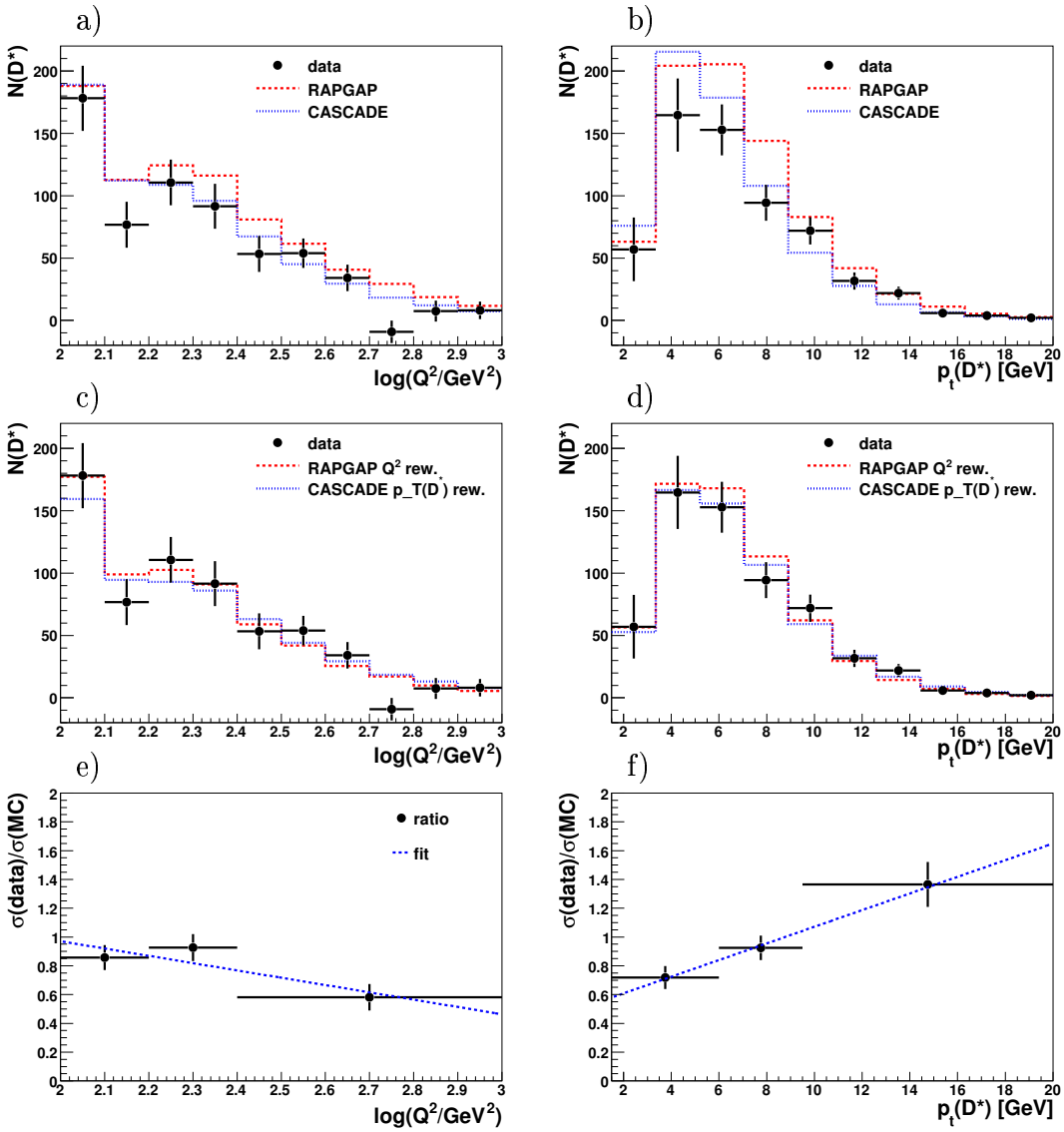

Figure 4.5: Comparison of the control distributions for Q^2 and $p_t(D^*)$ with the original MC simulations (a,b) and with the reweighted MC simulations (c,d). The ratio of the number of D^* in data vs. RAPGAP in bins of $\log_{10}(Q^2)$ and vs. CASCADE in bins of $p_t(D^*)$ is shown in (e) and (f), respectively. The straight line fit to these ratios is used as the reweighting function.

$z_{frag,gen}$ with a weight:

$$w_{frag}(z_{frag,gen}) = \frac{f_{meas}}{f_{bowler}}. \tag{4.9}$$

For each generated event f_{meas} is chosen according to the value of $\hat{s}$. The reweighting in the low $\hat{s}$ region, where both MC samples contain $\sim 30\%$ of all events, is stronger than in the high $\hat{s}$ region. The effect on the reconstruction efficiencies due to the reweighting is small ($< 3\%$).

In Fig. 4.5 a),b) the control distributions in Q^2 and $p_t(D^*)$ are shown where the wrong charge-subtracted data distributions are compared with the MC predictions on the reconstruction level. The Q^2 distribution in RAPGAP is above the data, whereas CASCADE describes the Q^2 better. In case of the p_t spectrum neither RAPGAP nor CASCADE describe the slope correctly. Therefore RAPGAP is reweighted in Q^2 and CASCADE in $p_t(D^*)$. For the reweighting the ratio of the observed number of D^* candidates in the data and the MC in the corresponding bins are calculated as shown in Fig. 4.5 e),f). The reweighting function is then obtained from a straight line fit to these ratios. The events are weighted using this reweight functions in the generated variables Q^2 and $p_t(D^*)$. The control plots with the reweighted MC samples are shown in Fig. 4.5 c),d) where the distributions in data are described well by the MC predictions.

4.3.4 Extrapolation in $p_t(D^*)$ to 1.5 GeV

For the definition of the visible range $p_T(D^*)$ is restricted to be larger than 1.5 GeV and the cross sections are corrected to this range. Since a Q^2 dependent $p_T(D^*)$ cut is applied on the reconstruction level, an extrapolation in $p_t(D^*)$ to 1.5 GeV is necessary. To estimate an additional extrapolation for each bin the relative fraction of events E falling in this region is calculated using the generated information of the same MC as used for the efficiency determination:

$$E = \frac{N_{gen}^{p_t>1.5}(D^*) - N_{gen}^{p_t>3\log(Q^2/100)+2}(D^*)}{N_{gen}^{p_t>1.5}(D^*)} \tag{4.10}$$

The results for the Q^2 bins are shown in Fig. 4.6 where the extrapolation E is given in % for each Q^2 bin for the both RAPGAP and CASCADE with and without reweighting. The values for CASCADE decrease significantly after reweighting since lower p_t values are more suppressed as shown in Fig. 4.5. In case of RAPGAP the Q^2 reweighting nearly does not change the values of E. The extrapolation increases to higher Q^2 but is in all cases smaller than 20 %.

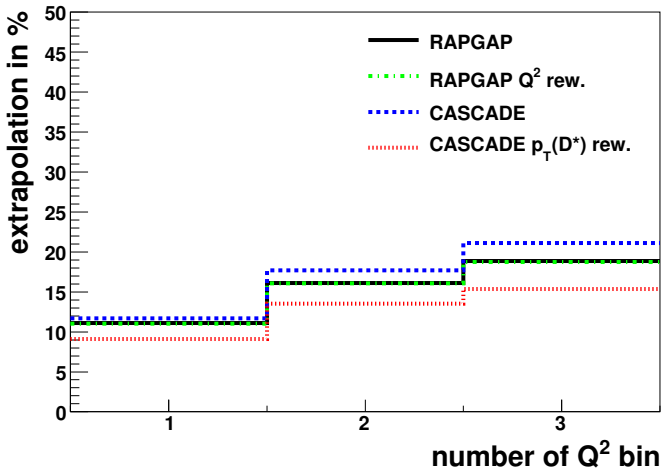

Figure 4.6: Extrapolation in $p_t(D^*)$ to the visible range of $p_t(D^*) > 1.5\,\text{GeV}$ for each Q^2 bin. Shown are the values vor RAPGAP,CASCADE and the $p_t(D^*)$ reweighted CASCADE.

4.4 Radiative Corrections

To correct the measured cross sections to the Born level (one photon exchange), contributions from NLO QED radiative processes have to be taken into account. These contributions are the initial state radiation (ISR) where a photon is radiated before the ep interaction, final state radiation (FSR) where the photon is radiated after the interaction and virtual loop corrections.

The difference to the Born level is usually expressed by $1+\delta_r$: $\sigma_{born+NLO} = (1+\delta_r)\cdot\sigma_{Born}$. Thus the correction of the cross sections to the Born Level is applied by a correction factor $c_{rad} = (1+\delta_r)^{-1}$ applied to the measured cross sections (see Eq.4.1). This correction factor is determined by comparing the cross sections predicted from the MC either with or without NLO radiative contributions:

$$c_{rad} = \frac{\sigma_{gen}^{non-rad}}{\sigma_{gen}^{rad}}. \tag{4.11}$$

The cross section σ_{gen}^{rad} is determined from a D^* sample generated by RAPGAP interfaced to HERACLES [47] as used for the determination of the reconstruction efficiency ϵ_{rec}. The cross section $\sigma_{gen}^{non-rad}$ has been calculated from a D^* sample where RAPGAP was used in a non-radiative mode. The correction factor for the full visible range amounts to 3%. This correction is calculated in each bin. In Fig. 4.7 the results are shown double differentially in bins of Q^2 and y. The correction varies from 2% to 5%.

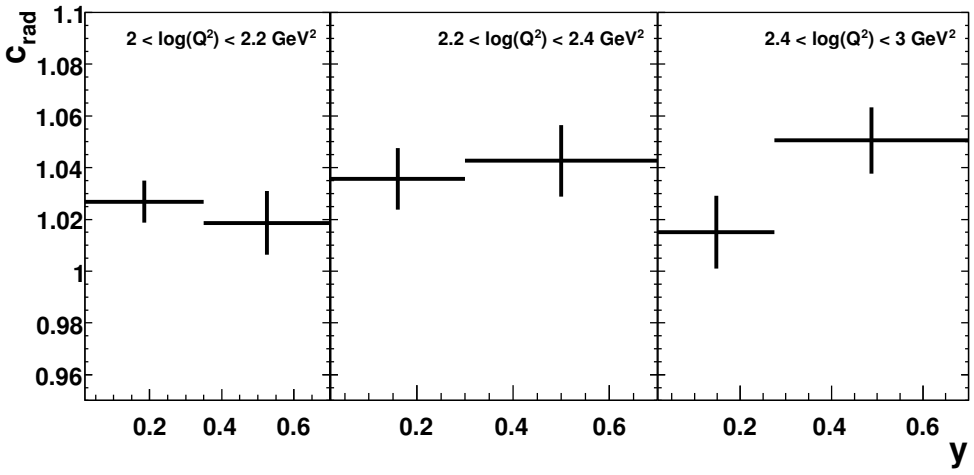

Figure 4.7: Correctionfactor c_{rad} in double differential Q^2y bins to get the measured cross sections at Born level.

4.5 Reflections

The contribution of other decay modes of the D^* to the signal in the ΔM distribution is studied. The decay modes of the D^* are:

$$D^{*\pm} \rightarrow (D^0\pi^{\pm}_{slow}, D^{\pm}\pi^0, D^{\pm}\gamma). \tag{4.12}$$

Only the first decay mode contributes to the golden channel since three charged tracks are required.

The following decay channels:

$$D^0 \rightarrow KK; K\pi\pi; \pi\pi; \pi\pi\pi; \pi\pi\pi\pi; Kl\nu_l; \pi l\nu_l \tag{4.13}$$

can contribute to the $\Delta M(D^*)$ distributions and are referred to as "reflections". Reflections can also occure if the D^0 is only partially reconstructed. The $M(K\pi)$ distribution is shown in Fig. 3.10. To the left from the D^0 peak corresponding to $D^0 \rightarrow K\pi$ a broad signal from other decay channels appears. The most of the decay channels are only partially reconstructed and the invariant mass is therefore lower. Although the reflections are suppressed by the restriction to a D^0 mass window of 80 MeV they can contribute to the signal and can not be separated in the data.

The contribution from reflections to the D^* signal is determined using the RAPGAP MC where on generator level the decay channels listed in Eq. 4.13 are also selected. The study was preformed on reconstruction level in bins of $p_t(D^*)$ since the resolution depends on the transverse momentum of the decay tracks. Fig. 4.8

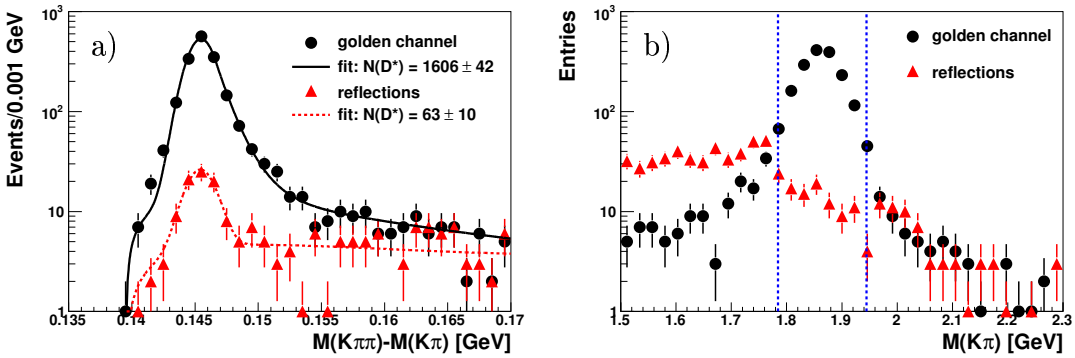

Figure 4.8: ΔM with fit (a) and $m(K,\pi)$ (b) spectra for two MC samples: one with at least one D^* decaying in the golden channel (black) and one with other decay channels selected (red).

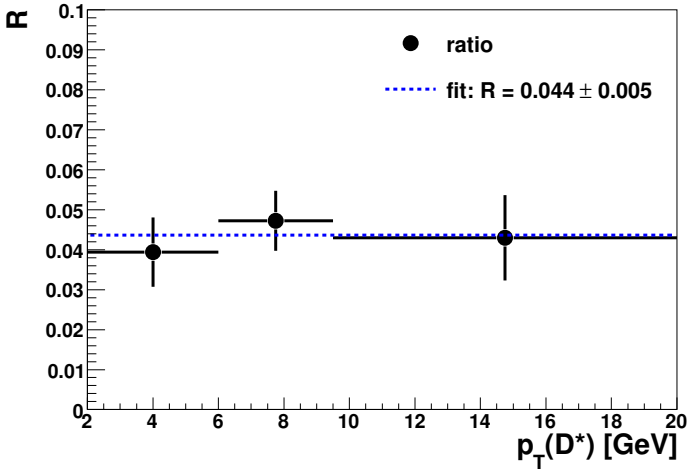

Figure 4.9: Relative contribution R of the reflections to the ΔM signal in bins of $p_t(D^*)$ with a mean fraction obtained from fit.

displays the ΔM and $M(K,\pi)$ distributions as an example for the $p_t(D^*)$ bin $6\,\mathrm{GeV} < p_t(D^*) < 9.5\,\mathrm{GeV}$ for the decay channel used in this analysis and for the reflections. To estimate the contribution of the reflections a gaussian fit has been used. The D^0 invariant mass distributions (b) demonstrate the behavior of the reflections as observed in data.

The relative contribution of the reflections to the D^* signal in bins of $p_t(D^*)$ is calculated as:

$$R = \frac{N_{\mathrm{rec}}^{\mathrm{refl.}}(D^*)}{N_{\mathrm{rec}}^{\mathrm{gol}}(D^*) + N_{\mathrm{rec}}^{\mathrm{refl}}(D^*)} \tag{4.14}$$

The result is shown in Fig. 4.9. Within the statistical error no significant $p_t(D^*)$ dependence of R is observed. Therefore a constant is fitted to the data with the result $R = 4.4\% \pm 0.5\%$, which is used as a correction for the cross section determination in each bin.

4.6 Experimental Systematic Errors

Statistical and systematic uncertainties give similar contribution to the total error on the cross section determination. The statistical error dominates in bins where the background is high (e.g. at high $\eta(D^*)$). In some cases (e.g. at large $z(D^*)$) where the background is low the systematic error dominates.

The systematic uncertainties are grouped into a bin to bin uncorrelated and a correlated part. Some of the errors are treated as partly correlated. The following uncorrelated systematic uncertainties are accounted for: The signal shape and the invariant mass resolutions of the data are not fully reproduced by the MC simulation. The errors on the D^* signal extraction are determined by varying the fit parameters within their uncertainties. The fraction of events outside the D^0 mass window is determined using the MC simulation. Half of this fraction is taken as a systematic error to account for the uncertainty on the D^0 mass resolution. An uncertainty of 0.5% is assigned to the contribution from reflections to account for a possible p_t dependence. The uncertainty of the QED radiative corrections is 1.5%.

The following correlated uncertainties are taken into account: The uncertainty on the hadronic energy scale is estimated by changing the hadronic energy by $\pm 2\%$ ($\pm 3\%$) for events where the scattered electron is detected in the LAr (SpaCal) calorimeter. The uncertainty due to the scattered electron measurement is estimated by varying the electron energy by $\pm 1\%$ and the polar angle by $\pm 3\,\mathrm{mrad}$, respectively. The trigger efficiency, luminosity and $D^* \to K\pi\pi$ branching ratio are known with uncertainties of 1%, 3.2% and 1.5%, respectively. An uncertainty of 1.2% on the cross-section measurement arises due to the uncertainty on the photoproduction background. The uncertainty on the reconstruction efficiency is taken as a half of the difference between the two simulations, RAPGAP and CASCADE. This also

Type of Error	total value
Uncorrelated errors	
Signal extraction	5%
D^0 mass window	4.4%
Radiative Corrections	1.5%
Reflections	0.5%
Correlated errors	
Model uncertainty CCFM vs. DGLAP	5.2%
Luminosity	3.2%
Electron scattering angle θ ± 3 mrad	2.2%
Electromagnetic energy scale $\pm 1\%$	1.9%
Branching ratio	1.5%
Photoprod. background	1.2%
Trigger efficiency	1%
Fragmentation	0.4%
Hadronic energy scale $\pm 2(3)\%$	0.2%
Part. correlated errors	
Track finding 2% per track	6%
Vertex fit efficiency	2.5%
Electron track efficiency	2%

Table 4.2: Summary of all systematic errors grouped into bin-to bin correlated, uncorrelated and partly correlated. For each source the error on the total cross section is given.

covers the uncertainty on the extrapolation to $p_T(D^*) = 1.5\,\mathrm{GeV}$. The uncertainty in the efficiency determination due to the charm fragmentation model is estimated by varying the Kartvelishvili parameter α within its error as given in Tab. 4.1.

The following uncertainties are treated as partly correlated: The uncertainty on the track reconstruction efficiency of 2% per track and the vertex fit efficiency of 2.5% per D^*-candidate translates to 6.5% per D^*-candidate. Further an uncertainty on the electron track-cluster matching of 2% is assigned.

Assuming that the individual systematic errors are uncorrelated they are added up in quadrature to get the total uncorrelated and correlated error. For this purpose the partly correlated errors are treated as 50% correlated and 50% uncorrelated since the correlations are not known. The total systematic uncertainty is given by the quadratic sum of the total uncorrelated and correlated errors.

A summary of the systematic errors on the measured cross sections is given in Tab. 4.2. For each source the error on the total cross section is given. The estimation

of the individual systematic errors is described in more detail in the following.

4.6.1 Uncorrelated Uncertainties

Uncertainty due to signal extraction

The systematic uncertainty due to fixing some of the fit parameters in the signal extraction is determined using the full D^* sample. The fixed parameters in the individual bins given by $\sigma_{i,fix} = c_\sigma \sigma_{i,MC}$ and $\alpha_{i,fix} = c_\alpha \alpha_{i,MC}$ (see Sec. 4.2) are varied according to the error of the global correction factors $c_\sigma = 1.27 \pm 0.10$ and $c_\alpha = 1.49 \pm 0.66$ respectively. These errors correspond to the statistical error on σ and α from the fit to the ΔM distribution of the full D^* sample. In Fig. 4.10 the relative deviations in the number of extracted D^* mesons in the data with respect to the varied values $\sigma_{i,fix}$ (a) and $\alpha_{i,fix}$ (b) are shown. The variation of $\sigma_{i,fix}$ leads to deviations within $\pm 5\%$. The deviations due to the varied $\alpha_{i,fix}$ are around $\pm 2\%$ in most of the bins. For the total uncertainty only the larger deviations are taken into account since both parameters are correlated. Therefore an uncertainty of 5% is assigned to the signal extraction.

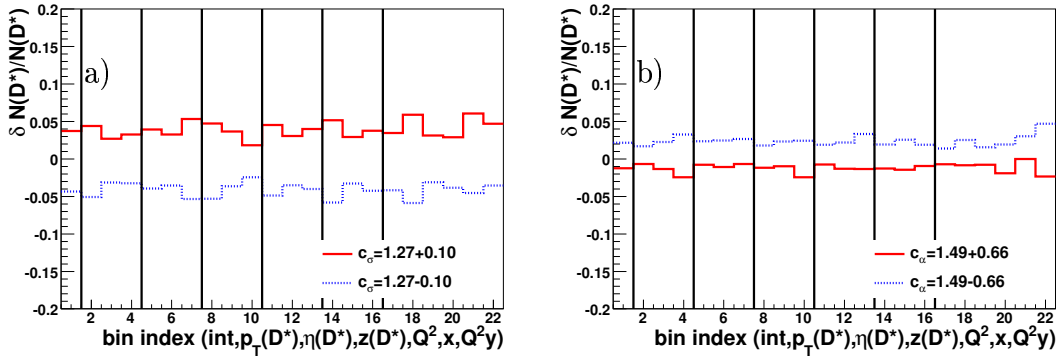

Figure 4.10: Relative deviations in the extracted number of D^* mesons in the data with respect to the variation of the fixed values $\sigma_{i,fix}$ (a) and $\alpha_{i,fix}$ (b) within the error of the global correction factors c_σ and c_α respectively.

Uncertainty due to the D^0 mass cut

At high $\langle p_t(D^*) \rangle$ the p_t dependence of the D^0 mass resolution becomes important. This can affect the efficiency of the selection applied on the D^0 mass window $|m(K\pi) - 1864| < 80\,\mathrm{MeV}$. In order to estimate the corresponding uncertainty of

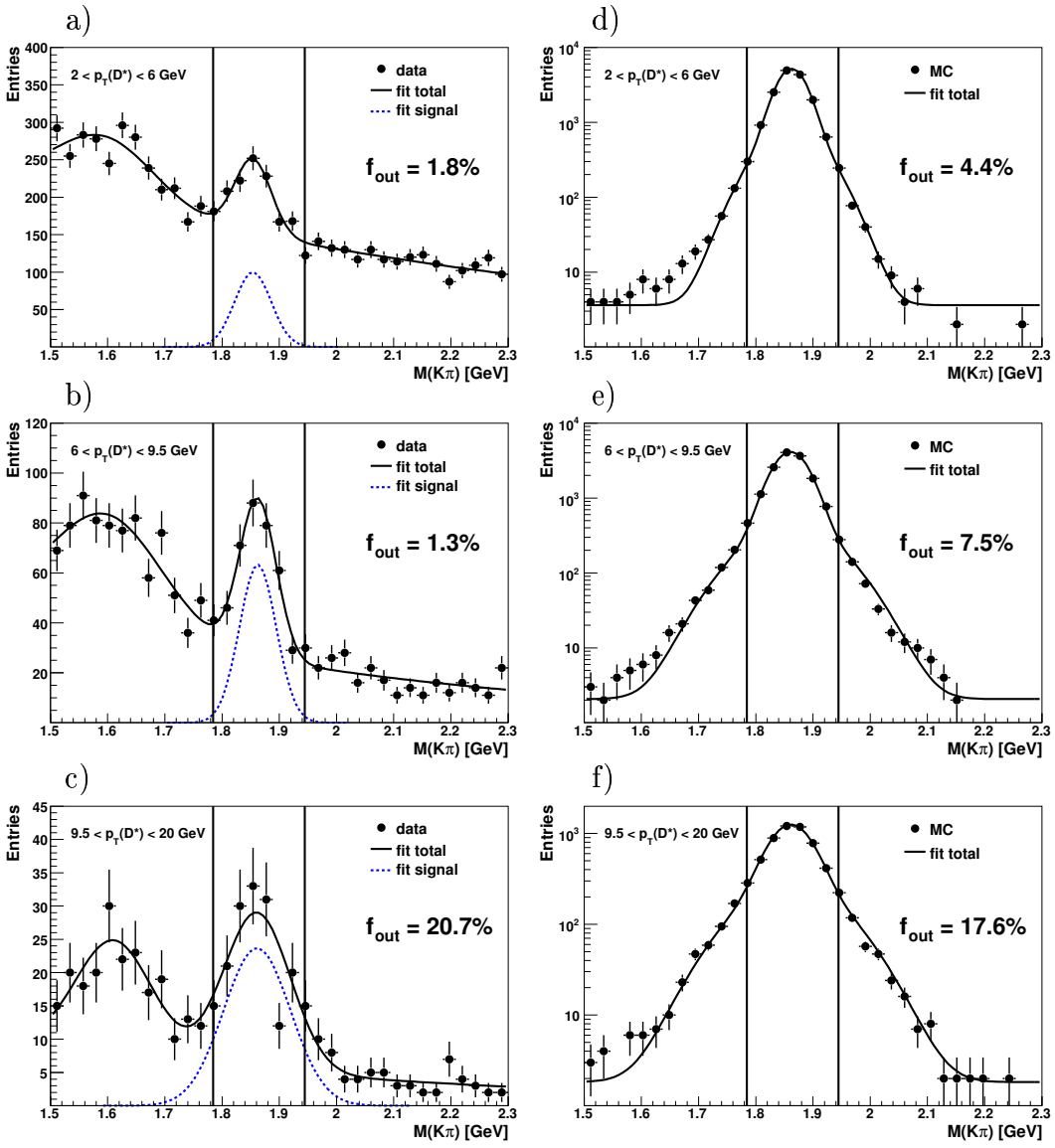

Figure 4.11: Invariant mass distributions $M(K\pi)$ of the D^0-meson candidates in bins of $p_t(D^*)$ for data (a-c) and MC (d-f) together with the fitted curves. Further shown are the signal function alone and the cut window used in this analysis. For MC only true D^0 are shown by matching with generator level information. The fractions of events outside the mass window are quoted.

this selection the invariant mass spectra of the D^0 for the data and MC are studied in bins of $p_t(D^*)$. In Fig. 4.11 the D^0 invariant mass spectra for the data and MC are shown in the bins of D^* transverse momentum. In the case of the MC, the reconstructed and a generated D^* are matched using the four vectors of the decay particles. In the data, a sum of two gaussians, one for the D^0 signal and one for the reflections on the left side, and an exponential function for the background is used for the fit. For the MC, a sum of two gaussians with a common mean is used.

The D^0 peak becomes broader with higher $p_t(D^*)$ (Fig. 4.11). In MC, the calculated fraction of events outside the D^0 mass window $f_{out} = N(D^*)_{out}/N(D^*)_{in}$ used for the error estimate increases from 4% in the lowest $p_t(D^*)$ bin to 18% in the highest bin. For the data the corresponding fraction varies from 2% to 21%. In the statistically limited data the sensitivity to the part of the signal outside the D^0 mass window is limited. Therefore only a single gauss is fitted to the D^0 signal. Hence, as a conservative error estimation, 50% of the fraction f_{out} in MC is taken as systematic uncertainty calculated in each bin.

In principle this uncertainty could be reduced by using a wider D^0 mass window. However it is not appropriate for this analysis because of significant increase of the combinatorial background in the $\Delta M(D^*)$ distribution.

Radiative correction uncertainty

The statistical error of the radiative correction factor c_{rad} calculated according Sec. 4.4 has to be taken into account as systematic uncertainty. This error does not exceed a value of 1.5% which is taken as overall systematic error.

Systematic uncertainties due to reflections

An uncertainty of 0.5% is assigned to the contribution from reflections to account for a possible p_t dependence.

4.6.2 Correlated Uncertainties

Model uncertainty

As mentioned in section 4.3.2 for the determination of the cross section σ the mean of the reconstruction efficiencies using the MC simulations RAPGAP and CASCADE is used. To estimate the model uncertainty, the cross sections σ_{rap} and σ_{cas} calculated using either RAPGAP or CASCADE for efficiency determination are compared with σ:

$$\frac{\delta\sigma}{\sigma} = \frac{1}{2}\frac{\sigma_{rap} - \sigma_{cas}}{\sigma} \tag{4.15}$$

In Fig. 4.12 the absolute values of the relative errors calculated for each bin and taken as model uncertainty are shown. This value amounts to 5% for the total cross section and varies between 1% and 8% in the individual bins.

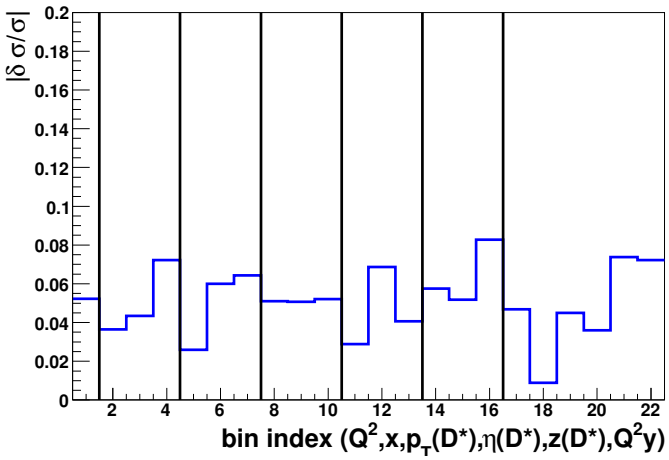

Figure 4.12: Calculated model uncertainty using RAPGAP or CASCADE for efficiency determination for each bin.

Uncertainty of luminosity measurement

The mean error of the luminosity measurement for the HERAII period is 3.2% as determined in [101].

Uncertainty from the electron measurement

The electron energy E'_e is known to $\pm 1\%$ and the polar angle of the electron θ_e to $\pm 3\,\mathrm{mrad}$ (Sec. 3.4.4). The influence of these uncertainties on the measured cross sections is calculated using the MC, i.e. on the reconstruction level the electron energy and polar angle are shifted separately by their uncertainty and the complete kinematics is recalculated. Then the analysis selection is applied and the reconstruction efficiencies are recalculated. The relative deviations with respect to the nominal cross section are shown for each bin in Fig. 4.13 for the electron energy (a) and the polar angle (b).

For the variation of the electron energy the systematic error amounts to 2% for the total cross sections and varies from 0.1% to 9% in the individual bins. The largest variation is observed in the last $z(D^*)$ bin, since large $z(D^*)$ corresponds to small y.

The variation of the electron polar angle leads to a shift of the cross section by 2% for the total sample and from 0% to 7% in the individual kinematic bins. The

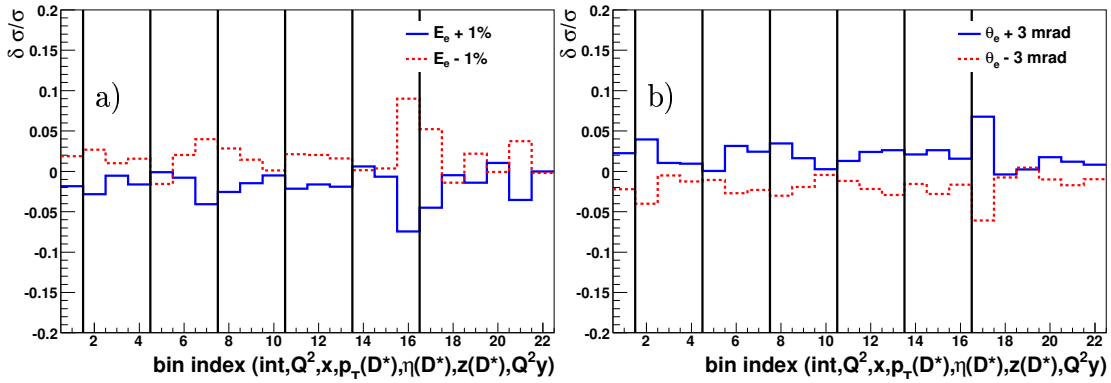

Figure 4.13: Variations in the cross sections for each bin when shifting E'_e (a) and θ_e (b) in the MC simulation used for efficiency estimation.

large variation in the lowest (Q^2, y) bin can be explained as follows: at low Q^2 and large x (small y) the population in the first double differential bin is dominated by the SpaCal sample (see Fig. 3.3). The corresponding Q^2 distribution for the SpaCal sample shown in Sec. 3.4.3 falls from the maximal value at $\log_{10}(Q^2/\mathrm{GeV}^2) = 2$ to nearly zero at $\log_{10}(Q^2/\mathrm{GeV}^2) = 2.2$, namely the right border in Q^2 of this bin. Therefore migrations in Q^2 due to variation of θ_e take place only at the left bin border, not compensating migrations on the right bin border.

Uncertainty on the branching ratio

The branching ratio for the decay of the D^* meson in the golden decay channel $\mathcal{B}(D^* \to K\pi\pi_s)$ has an error of 1.5% [93].

Uncertainty on the trigger efficiency

The trigger efficiency has been estimated separately for the LAr and the SpaCal samples (see Sec. 3.4.5). To estimate the systematic uncertainty on the trigger efficiency for the LAr sample different subsamples of the reference triggers used for efficiency determination has been considered. The calculated efficiencies for the different subsamples are shown in Fig. 4.14. The change is within 1% around the mean efficiency of 98% except for the last bin where the efficiency for the subsample with s52 or s60 is 96%. This deviation in the last bin is neglected.

For the SpaCal the trigger efficiency is $> 99\%$ and no further variations of the reference trigger sample has been tested. A total error of 1% is taken as uncertainty for trigger efficiency covering the SpaCal data sample.

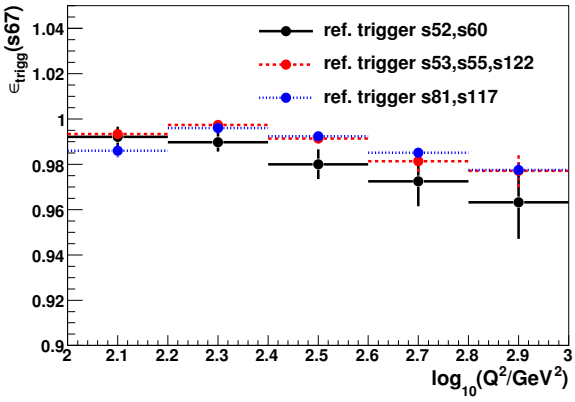

Figure 4.14: Trigger efficiency of s67 for different reference trigger subsets.

Uncertainty on the photoproduction background

The event sample used in this analysis contains photoproduction events where a particle from the hadronic final state is misidentified as a scattered electron. To estimate the photoproduction background the charge of the track matched to the electron cluster (see Sec. 3.4.2) is compared with the expected charge for the scattered electron/positron. The fraction of events with a wrong charged electron track amounts to 2.7% for the data and 1.5% for MC (RAPGAP) with a difference of 1.2% between data and MC. Assuming that in case of a photoproduction event the matched track has a probability of about 50% to have the expected charge, this difference is taken as systematic uncertainty for the photoproduction background.

Uncertainty due to fragmentation

As described in Sec. 4.3.3 the longitudinal part of the Bowler fragmentation is reweighted in the MC to the fragmentation according to the Kartvelishvili parametrisation, as function of $\hat{s}$. For the estimate of the systematic uncertainty the Kartvelishvili parameter α is varied within its experimental error $\delta\alpha$ given in Tab. 4.1. The reconstruction efficiencies are recalculated accordingly. The variations in α are done for both $\hat{s}$ regions in the same direction simultanously. The deviations in the cross sections estimated with the average efficiency from RAPGAP and CASCADE are shown in Fig. 4.15. The systematic error is in all bins smaller than 1.1%.

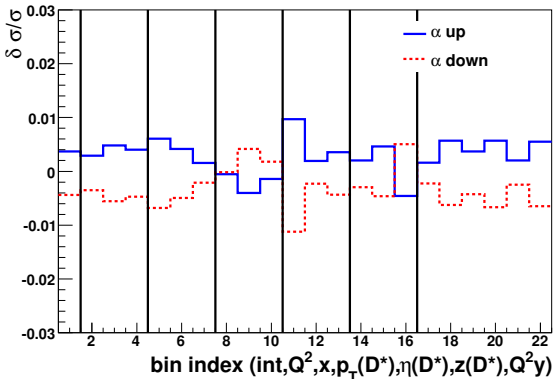

Figure 4.15: Variations in the cross sections for each bin when varying the parameter α within its experimental uncertainty in MC. The variations are calculated with respect to the mean efficiency obtained from RAPGAP and CASCADE.

Uncertainty due to the hadronic energy scale

The $e\Sigma$ method used for the reconstruction of the kinematics uses the four-vector of the hadronic final state. According to Sec. 3.4.4 the relative errors on the energy of the hadronic final state E_{had} amounts to 2% for the LAr sample and 3% for the SpaCal sample. E_{had} was varied according to its error in LAr and SpaCal, resulting

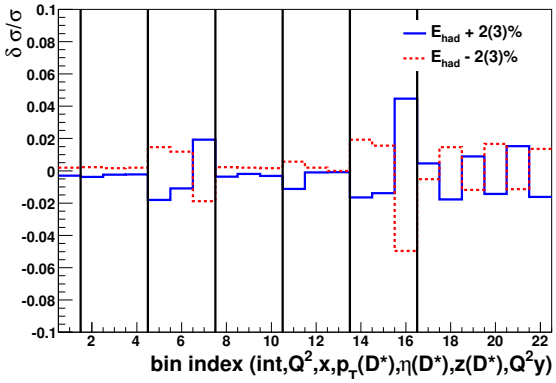

Figure 4.16: Variations in the cross sections for each bin when shifting E_{had} in the MC used for efficiency estimation.

in uncertainties shown in Fig. 4.16. The systematic error amounts to 0.3% for the total cross section and varies from 0.1% to 5% in the individual bins. Except for the last z bin the errors are smaller than 2%.

4.6.3 Partially Correlated Uncertainties

Uncertainty due to track finding

The uncertainty of the track reconstruction efficiency of 2% per track resulting in 6% per D^* is one of the dominant systematic errors in the analysis. In App. B a detailed description of this error is given. The uncertainty of 2% is deduced from the measurement of the track finding efficiencies for electrons using the measurement of the LAr calorimeter as a reference. The reconstruction of cosmic muons passing from above through the CJC where two tracks are expected [102] is used as well.

To account for this uncertainty the following has to be considered: the measurements are only done for tracks with transverse momenta of $p_t > 1\,\mathrm{GeV}$. Within this thesis the uncertainty in the track reconstruction efficiency at very low momenta $p_t < 140\,\mathrm{MeV}$ has been reduced to below 1%. Since the question of the uncertainty of the tracking efficiency in the intermediate momentum region is still not settled the uncertainty could not be reduced for this analysis. Furthermore it has to be taken into account that kaons and pions undergo nuclear interactions with the material. The treatment of the nuclear interactions is done in the dedicated analysis [103] from which a correction routine for the track reconstruction efficiency was derived and applied on the reconstruction level of MC simulations.

Uncertainty due to primary vertex fit

The uncertainty of the primary vertex fit has been estimated in [94] where the vertex fit efficiency per D^* meson candidate is estimated as the ratio of the number of D^* mesons reconstructed either with vertex fitted tracks or with non-vertex fitted tracks. A difference of the efficiencies between data and MC of 2.5% for the full sample has been observed. The difference has been analysed as function of the transverse momentum of the slow pion $p_t(\pi_{slow})$ with no dependence observed. Therefore 2.5% can be adopted here as primary vertex fit efficiency despite of the fact that at higher Q^2 the transverse momenta of the decay particles of the D^* are significantly higher than in the medium Q^2 analysis, where this efficiency has been calculated.

Uncertainty due to electron track matching

As described in Sec. 3.4.2 a matched non vertex fitted track with $DCA_{track-cluster} < 12\,\mathrm{cm}$ and the expected charge is required to reduce the photoproduction background. To test the matching, especially the angular acceptance of the CJC for the measurement of the electron track, the efficiency for matching at least one non vertex fitted track to the cluster ϵ_{match} is calculated. The result is shown in Fig. 4.17 a) for data and MC in bins of Q^2. At low Q^2 a discrepancy of 2% between data and MC is observed which decreases at higher Q^2 to $< 0.5\%$. Fig. 4.17 b) compares

the matching efficiencies for tracks which are required to be fitted to the primary vertex. The efficiencies are lower than for matching a non-vertex fitted track and the difference between data and MC increases up to 4% in some bins. This is due to a bias of the CJC for scattered electron tracks in the forward direction where the z measurement of the single hit is distorted in regions with high hit densities [104]. The tracks are still found but could not be fitted to the vertex. Due to this problem only a matched non vertex fitted electron track is required where according Fig. 4.17 a) an overall error of 2% can be taken as systematic uncertainty.

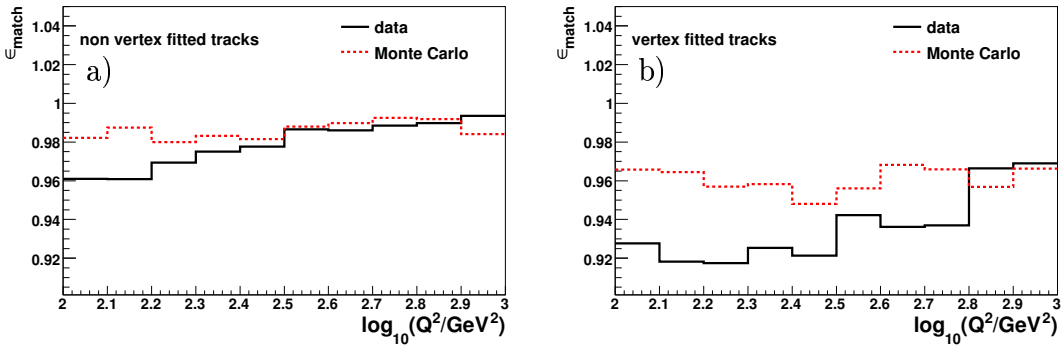

Figure 4.17: Electron track-cluster match efficiency in data and MC for non vertex fitted tracks (a) and vertex fitted tracks (b).

Chapter 5

Results and Discussion

The results of the analysis are discussed in this chapter. The inclusive differential cross sections of D^*-meson production are presented. The double-differential cross sections in bins of Q^2 and y are used to determine the charm contribution $F_2^{c\bar{c}}$ to the proton structure function F_2. Tables with the results of this analysis including all systematic uncertainties for each bin for the $F_2^{c\bar{c}}$ measurement can be found in Appendix A.

5.1 The Cross Section Measurements

The total inclusive cross section for D^* meson production in the phase space covered in this analysis (see Tab. 3.2) is measured to be

$$\sigma_{vis}(e^+p \to e^+D^{*\pm}X) = 225 \pm 14(stat) \pm 27(syst) \text{ pb}. \tag{5.1}$$

The corresponding predictions from RAPGAP, CASCADE and HVQDIS amount to 322 pb, 279 pb, and 241^{+14}_{-15} pb, respectively. A certain fraction of D^* mesons originate from beauty quarks produced in the hard scattering process, with their following weak decay into charm. The contribution of beauty is estimated in RAPGAP, CASCADE and HVQDIS to amount to 6%, 7% and 4%, respectively. In case of HVQDIS the hadronisation corrections determined with RAPGAP are applied.

The NLO prediction is in a good agreement with the measured cross section whereas the Monte Carlo predictions overestimate the measurement.

In Fig. 5.1 the single differential $D^{*\pm}$ cross sections are shown as a function of x and Q^2 as well as a function of the $D^{*\pm}$ observables $p_t(D^*)$, $\eta(D^*)$ and $z(D^*)$. The data are compared to the expectations from the HVQDIS calculation and predictions of the RAPGAP and CASCADE simulations. Also the ratios of the theoretical predictions to the data are shown. Neither Monte Carlo simulation describes the

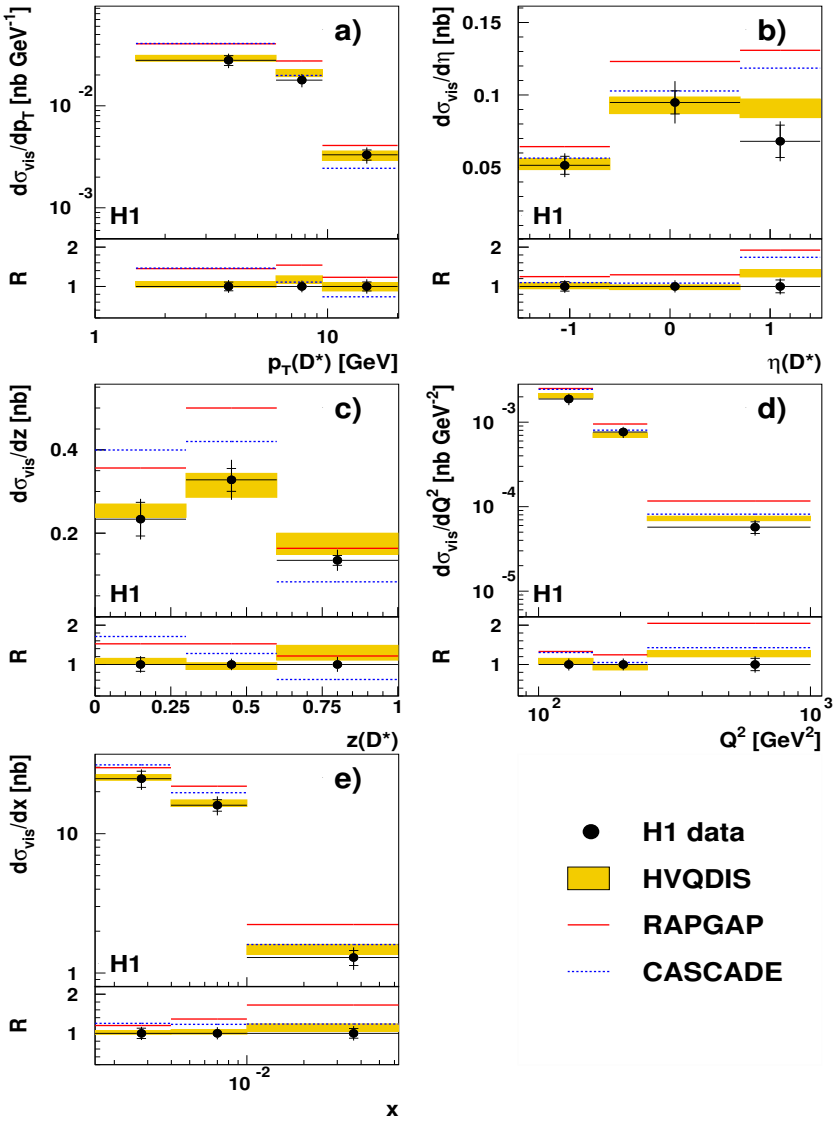

Figure 5.1: Differential cross sections for inclusive D^* meson production as a function of $p_t(D^*)$, $\eta(D^*)$, $z(D^*)$, Q^2 and x. The inner error bars indicate the statistical uncertainties, the outer error bars show the statistical and systematic uncertainties added in quadrature. The expectations of CASCADE (dashed line) and RAPGAP (solid line) are obtained using the parameters as described in section 1.4. The band of the HVQDIS prediction (shaded) is obtained using the parameter variation described in section 1.5. The ratio $R = \sigma_{theory}/\sigma_{data}$ is also shown. In the case of HVQDIS the theoretical uncertainties are taken into account. The inner error bars on the data points at $R = 1$ display the relative statistical errors, and the outer error bars show the relative statistical and systematic uncertainties added in quadrature.

shape and normalisation of the D^* kinematical distributions well. The HVQDIS calculation however agrees with the data within the theoretical uncertainties obtained by parameter variations as described in Sec. 1.5.

In Fig. 5.2 the double differential cross sections are shown as a function of y for different bins in Q^2. The data are compared to the expectations of the HVQDIS calculation as well as to the RAPGAP and CASCADE simulations. HVQDIS describes the data well. Except for the first (Q^2, y) bin, the same holds for CASCADE. RAPGAP significantly overestimates the visible cross section.

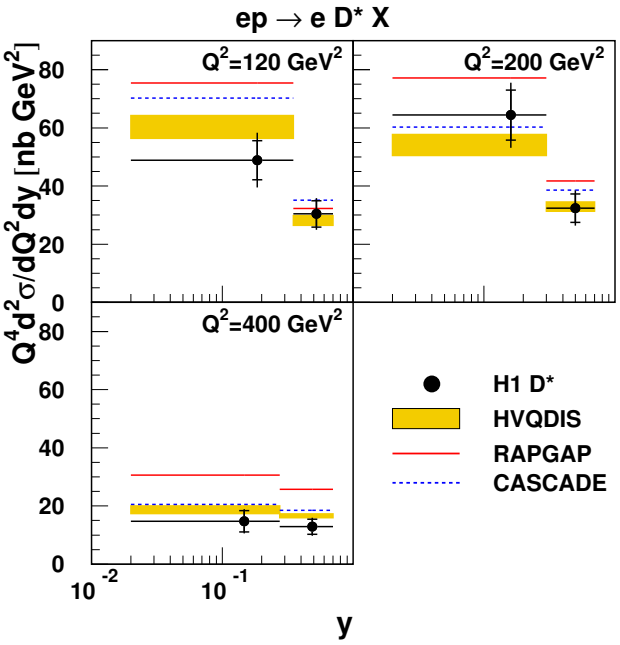

Figure 5.2: Double-differential cross sections for D^* meson production as a function of y in different Q^2 bins. For the purpose of presentation the cross sections are multiplied by Q^4. The data (closed symbols) are shown with the statistical (inner error bars) and total (full error bars) uncertainties. Predictions from the RAPGAP (solid line) and CASCADE (dashed line) Monte Carlo simulations and the HVQDIS NLO calculation (shaded area) are also shown.

One of the main goals of this analysis is to test the reliability of recent charm production models in the massive and the massless scheme at higher photon virtualities Q^2. In previous analyses of charmed meson production at H1 e.g. [86, 105] and ZEUS e.g. [106–109] at much smaller photon virtualities[1] the cross sections have also

[1]However at ZEUS the DIS phasespace ranges also up to $Q^2 = 1000\,\mathrm{GeV}^2$ but distributions in other kinematical variables than Q^2 are dominated by events at lower Q^2.

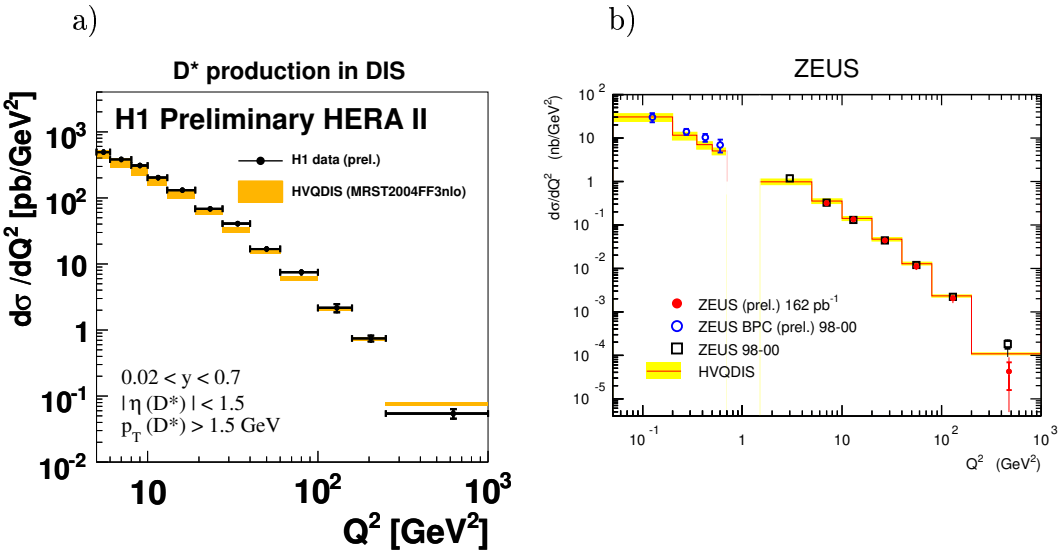

Figure 5.3: The D^* production cross section as a function of Q^2 in the kinematic region $0.02 < y < 0.7$, $p_t(D^*) > 1.5\,\text{GeV}$ and $|\eta(D^*)| < 1.5$ for different H1 and ZEUS measurements [86, 107–109] where the last three points in a) are from this analysis. The data are compared to the HVQDIS NLO prediction. The data are represented as points and squares. The inner error bars are statistical while the open error bars are the sum of statistical and systematic uncertainties added in quadrature. The shaded area indicates the theoretical uncertainties obtained by variations of the HVQDIS parameters.

been compared to predictions of massive NLO calculations in the FFNS. In general the massive predictions provide a good description of the measured cross sections except for the forward region where the NLO calculation tends to underestimate the data. According to [26] the massive calculation is expected to break down at a scale μ, usually choosen to be $\mu = Q^2$, $\mu >> m_c$. This is due to the fact that the Wilson coefficients C^i (see. Eq. 1.23) contain logaritmic terms of the form $\alpha_s^n \ln^m(Q/m_c)$, where $m = 1...n$, at order n of the pertubative expansion. The present measurement shows, that also at $100 < Q^2 < 1000\,\text{GeV}^2$ a good description of all kinematical distributions by the massive NLO calculation is achieved. The conclusion is that the massive NLO calculation is valid in the whole Q^2 range accessible for D^* measurements at HERA. In Fig. 5.3 D^* meson production cross sections are shown as a function of Q^2 measured by H1 (a) and ZEUS (b) [86, 107–109] over a wide range of Q^2 and compared to the HVQDIS NLO prediction. A good description is achieved over the whole Q^2 range.

On the other hand, the MC predictions disagree with the data at large Q^2

(Fig. 5.1) e.g. in case of RAPGAP by a factor of two in the last Q^2 bin. It has been shown [86] that the prediction of RAPGAP using the same PDF is $\sim 25\%$ below the measured cross section in data for $Q^2 < 100\,\mathrm{GeV}^2$. Different PDF sets have been studied and none was describing the data in the whole kinematic range. Unfortunately, no consistent PDF set is currently available for the existing RAPGAP MC generators of charm production in DIS: CTEQ65m is a NLO PDF meaning that it has been determined from a fit to inclusive data using a NLO calculation for the hard scattering amplitudes whereas RAPGAP implements calculations at LO and parton showers. Although for such MC it is recommended to use NLO PDFs [110] but the validity is not proven. The CASCADE Monte Carlo uses a consistent PDF set (A0) but predicts a much softer $p_t(D^*)$ and $z(D^*)$ spectrum. For $Q^2 < 100\,\mathrm{GeV}^2$ the CASCADE Monte Carlo provides better descriptions of the measured cross sections [86]. Since $p_t(D^*)$ and $z(D^*)$ are correlated, disagreement in both observables could be caused by a too soft simulated p_t spectrum. This could indicate inproper gluon k_t of the unintegrated gluon density at higher Q^2.

The data are also compared to predictions of calculations in the ZMVFNS prediction [55]. This calculation has an intrinsic limitation on the transverse D^* momentum in the photon-proton center of mass frame $p_t^*(D^*)$, namely $p_t^*(D^*) > 2\,\mathrm{GeV}$. Therefore the same additional cut is applied to the data and the cross section is determined for the corresponding phase space. In Fig. 5.4 the D^* cross sections are shown as a function of $p_t^*(D^*)$, $p_t(D^*)$, $\eta(D^*)$ and Q^2, together with ZMVFNS and HVQDIS calculations. The ZMVFNS prediction fails to describe the data, while HVQDIS agrees well with the data.

The massless scheme for charm production should be only valid for energy scales far above the charm quark mass threshold. According to [26] this clearly does not hold when μ/m_c is of order 1 where μ is the dominant energy scale. Previous comparisons of measured D^* meson production cross sections to the ZMVFNS predictions for $Q^2 < 100\,\mathrm{GeV}^2$ [86,105] show also fair description of the data especially in $\eta(D^*)$. In Fig. 5.5 the D^* meson production cross section as a function of Q^2 measured by H1 for HERAI data [105] is shown. At higher Q^2 the ZMVFNS prediction overestimates the cross section by almost $\sim 50\%$ (note the statistical error of data of $\sim 20\%$). The latter is consistent with the results from this analysis where the data are also strongly overestimated (see. Fig. 5.4). The description does not become better although the mean Q^2 is one order of magnitude higher. The results from this thesis (Fig. 5.4) show that the disagreement between the data and the ZMVFNS prediction is mostly at lower $p_t(D^*)$ whereas the corresponding distributions in bins of Q^2 disagree only in normalisation. Such, the possible conclusion could be that the photon virtuality Q can not be taken as the relevant energy scale but rather $p_t^*(D^*)$. In the kinematic range of D^* production at HERA, the average $p_t^*(D^*)$ is $2\,\mathrm{GeV}$, which is of the order of m_c.

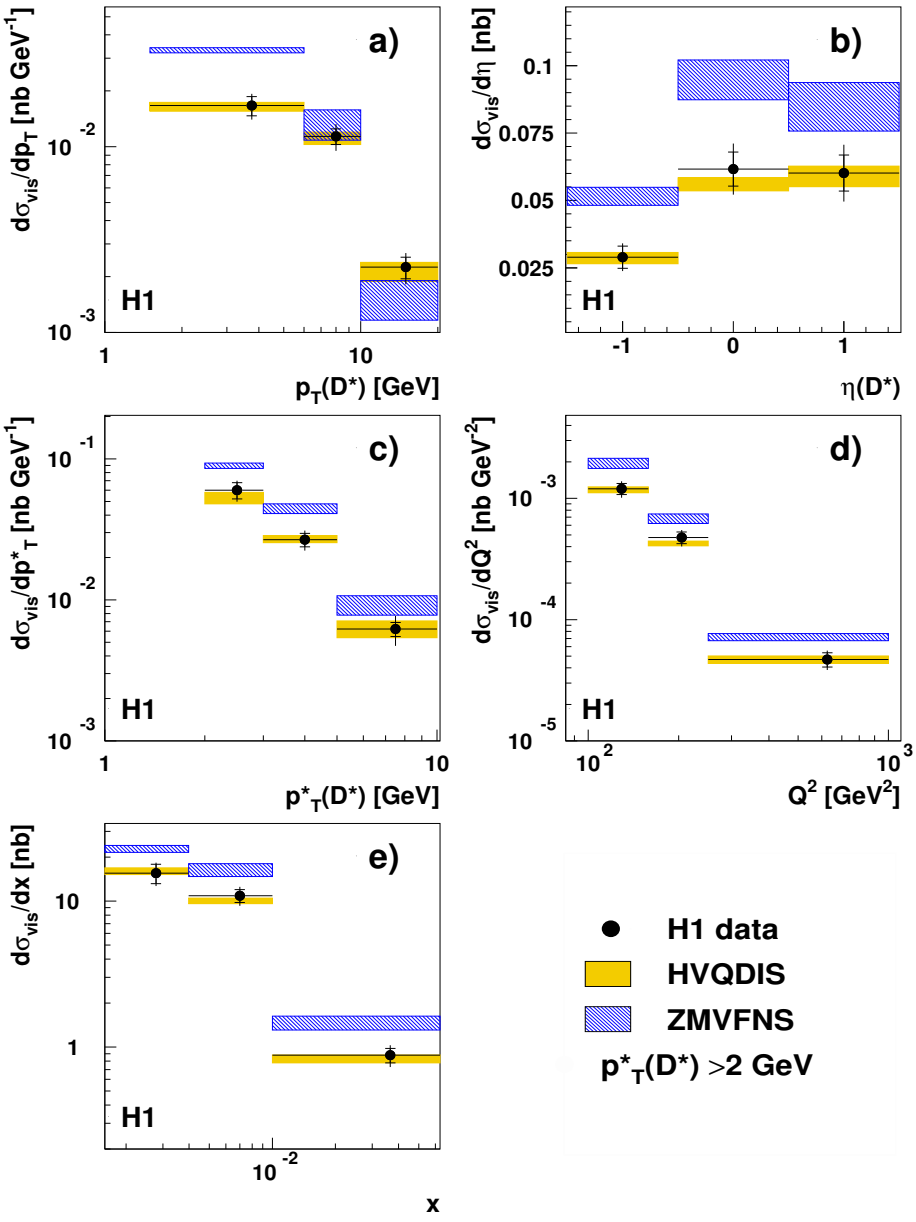

Figure 5.4: Differential cross sections for inclusive D^* meson production as a function of $p_t(D^*)$, $\eta(D^*)$, $p_t^*(D^*)$, Q^2 and x as measured for $p_t^*(D^*) > 2\,\mathrm{GeV}$. The inner error bars indicate the statistical uncertainties, the outer error bars show the statistical and systematic uncertainties added in quadrature. The expectation of HVQDIS (shaded band) is obtained using the parameter variation described in section 1.5. The prediction in ZMVFNS is represented by the hatched band where the uncertainty originates from the scale variation.

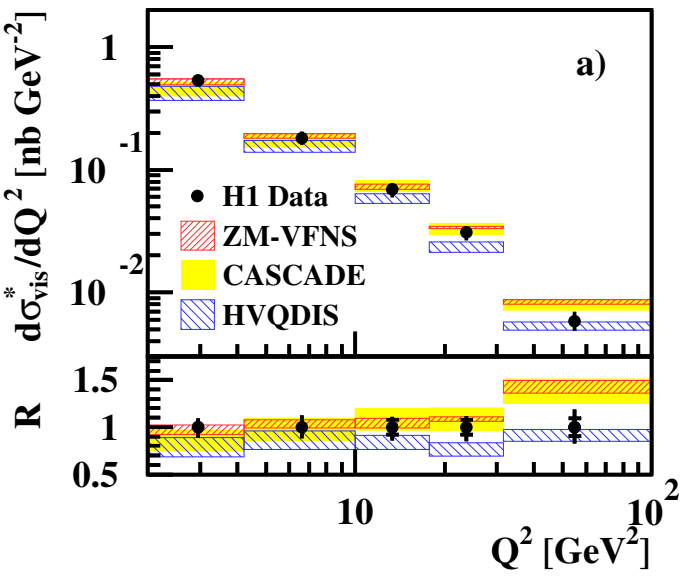

Figure 5.5: Differential cross sections for inclusive D^* meson production with $p_t^*(D^*) > 2\,\text{GeV}$ as a function of Q^2 from the measurement [105]. The inner error bars indicate the statistical errors, and the outer error bars show the statistical and systematic uncertainties added in quadrature. The bands for the expectations of ZMVFNS and of HVQDIS and CASCADE. On the bottom the ratio theory over data for the predictions is also shown.

5.2 The Charm Contribution $F_2^{c\bar{c}}$ to the Proton Structure F_2

The charm contribution $F_2^{c\bar{c}}$ to the proton structure function F_2 is defined by using the expression for the one photon exchange cross section for charm production:

$$\frac{d^2\sigma^{c\bar{c}}}{dxdQ^2} = \frac{2\pi\alpha_{em}^2}{Q^4 x}\left([1+(1-y)^2]\,F_2^{c\bar{c}}(x,Q^2) - y^2 F_L^{c\bar{c}}(x,Q^2)\right). \tag{5.2}$$

An intrinsic problem for the extraction of $F_2^{c\bar{c}}$ is the need of the extrapolation of the visible cross section of D^* production to the full phase space. Hence theoretical uncertainties of the prediction used for extrapolation have to be considered. At high Q^2 these uncertainties are small in comparison to the experimental errors. Since the extracted quantity $F_2^{c\bar{c}}$ refers to the full phase space a combination with the results from other measurements covering different visible range and exploiting other charm

tagging techniques is possible. With proper treatment of the correlations of the systematic uncertainties the combination leads to smaller experimental errors.

For the calculation of $F_2^{c\bar{c}}$ it has to be taken into account that the inclusive charm cross section depends on $F_2^{c\bar{c}}$ and $F_L^{c\bar{c}}$ according Eq. 5.2. The contribution of the second term $y^2 F_L^{c\bar{c}}$ in Eq. 5.2 to the inclusive charm cross section is calculated from the prediction of Ref. [111, 112]. The contribution amounts to at most 3 % and is neglected.

The visible inclusive $D^{*\pm}$ cross sections $\sigma_{\rm vis}^{\rm exp}(y, Q^2)$ in bins of y and Q^2 are converted to a bin centre corrected $F_2^{c\bar{c}}(\langle x \rangle, \langle Q^2 \rangle)$ in the framework of a particular model by the relation:

$$F_2^{c\bar{c}}(\langle x \rangle, \langle Q^2 \rangle) = \frac{\sigma_{\rm vis}^{\rm exp}(y, Q^2)}{\sigma_{\rm vis}^{\rm theo}(y, Q^2)} \cdot F_2^{c\bar{c}\ \rm theo}(\langle x \rangle, \langle Q^2 \rangle) \tag{5.3}$$

where $\sigma_{\rm vis}^{\rm theo}$ and $F_2^{c\bar{c}\ \rm theo}$ are the theoretical predictions from the model under consideration. For each y-Q^2 bin $F_2^{c\bar{c}}$ is calculated at a certain point in the x-Q^2 space $(\langle x \rangle, \langle Q^2 \rangle)$. For each y-Q^2 bin centers of gravity $(\langle x \rangle_{cg}, \langle Q^2 \rangle_{cg})$ are determined using data. A bin center correction is applied by interpolation of the (x, Q^2) points to proper values of $(\langle x \rangle, \langle Q^2 \rangle)$. The contribution from beauty is subtracted from the measured visible cross sections.

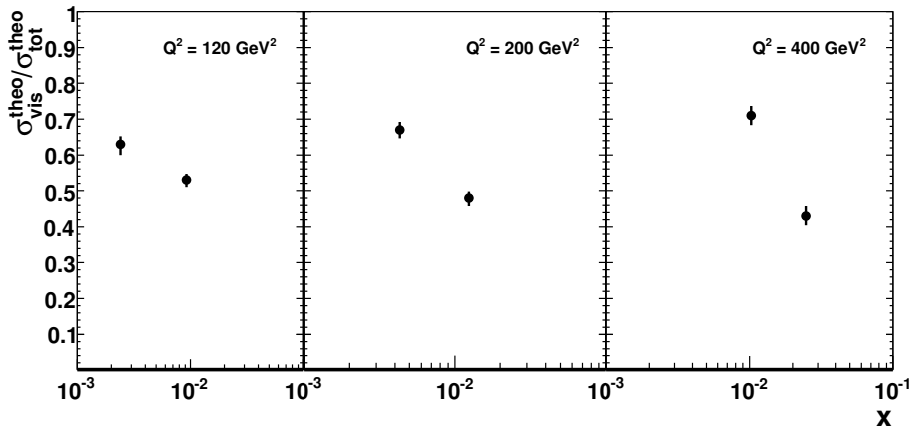

Figure 5.6: Fractions of the visible cross sections with respect to the full phase space as determined by HVQDIS in bins of the extracted $F_2^{c\bar{c}}$.

As in previous publications [113–115] the HVQDIS program and the program of Riemersma et al. [116] are used to calculate $\sigma_{\rm vis}^{\rm theo}$ and $F_2^{c\bar{c}\ \rm theo}$ in NLO. The fraction $f(c \to D^{*\pm})$ of charm quarks fragmenting into $D^{*\pm}$ mesons is taken as $f(c \to D^{*\pm}) = 23.8 \pm 0.8\%$ [30] from the combination of measurements in e^+e^-

experiments. In an earlier publication [113] CASCADE was used as an alternative extrapolation model. In the analysis presented here CASCADE is not used for F_2^c extraction as it disagrees with the kinematic distributions in data, see Fig. 5.1.

The extrapolation uncertainties on the measurement of $F_2^{c\bar{c}}$ are estimated by varying the HVQDIS model parameters as described in section 1.5. The variations of the charm mass, scales and PDFs are made simultaneously in the calculation of the visible D^* cross sections by the HVQDIS program and the prediction for $F_2^{c\bar{c}}$ in the full phase space. The total extrapolation uncertainties in the individual bins vary between 3% and 7% and are dominated by the variation of the renormalisation and factorisation scales.

The size of the extrapolation is illustrated in Fig. 5.6, where the fraction of the total D^* cross section in the visible phase space, as predicted by HVQDIS and given by $\frac{\sigma(y,Q^2)^{theo}_{vis}}{\sigma(y,Q^2)^{theo}_{tot}}$, is plotted. It varies between 0.4 and 0.7. This fraction is significantly lower at high x where the D^* mesons are mostly produced in forward direction and have larger probability to not be fully reconstructed in the detector.

Fig. 5.7 shows the values of $F_2^{c\bar{c}}$ as a function of x for different values of Q^2 and demonstrates that they are consistent with those obtained using the H1 vertex detector information [117, 118].

The expectation from the recent PDF fit to the inclusive DIS data, H1PDF2009 [119] tends to overestimate the data. In Fig. 5.8 the measured $F_2^{c\bar{c}}$ is compared to the massive FFNS calculation [116] at NLO and NNLO [120, 121] and to the GMVFNS predictions at NLO and NNLO [120–123]. The FFNS predictions agree well with the data over the full kinematic region investigated. The expectations for $F_2^{c\bar{c}}$ from a global fit in the GMVFNS at NLO tend to overestimate the data. At NNLO the GMVFNS prediction agrees better with the data.

The results of this analysis were used in the combination of the $F_2^{c\bar{c}}$ measurements by both H1 and ZEUS experiments implying different charm tagging methods [124]. In Fig. 5.9 results from the different H1 and ZEUS analyses are shown together with the combined $F_2^{c\bar{c}}$. The data cover the kinematic range of photon virtuality $2 < Q^2 < 1000\,\mathrm{GeV}^2$ and $10^{-5} < x < 10^{-1}$. This analysis contributes to the Q^2 bins at $\langle Q^2 \rangle = 120, 200, 400\,\mathrm{GeV}^2$. This measurement is consistent with the others. For the combined $F_2^{c\bar{c}}$ the correlations of the systematic uncertainties between the different measurements are taken into account. In Fig. 5.10 the combined $F_2^{c\bar{c}}$ is shown in comparison to the HERAPDF1.0 [8] and predictions from the global fit analyses of MSTW08 [125] at NLO and NNLO in the GMVFNS. The GMVFNS predictions (MSTW fit) at NNLO provide a good description of the combined H1 ZEUS $F_2^{c\bar{c}}$ data over a wide range of Q^2.

The test of reliability of different ways of implementation of GMVFNS in the PDF fits is one of the key issues in the QCD analyses and description of the nucleon structure: It has been shown that ZMVFNS fails to describe most of the DIS data

in the range of medium Q^2, where most of the HERA data contribute. On the other hand, FFNS describes the heavy flavour production very well, however PDF fits in the FFNS would cover only the NC data; for the moment no prescription of FFNS fits to the CC data exist.

Heavy flavour production at HERA is an elegant tool to test different implementations of GMVFNS. The full HERA-combined measurement of $F_2^{c\bar{c}}$ is on the way to its final precision, but already now has the decisive power to distinguish between diffent approaches. It is planned to use this combined $F_2^{c\bar{c}}$ together with inclusive HERA data for a new PDF fit with the aim of a better constraint of some parameters like the charm mass on which the measurement presented in this thesis will be included.

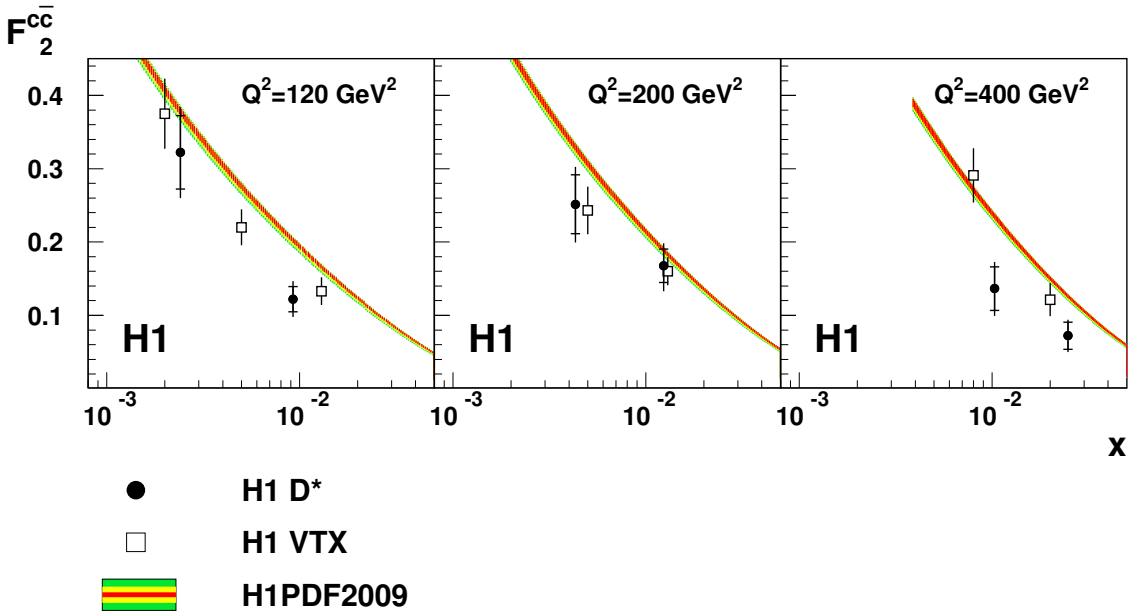

Figure 5.7: The charm contribution $F_2^{c\bar{c}}$ to the proton structure function. The data (closed symbols) are shown with statistical (inner error bars) and total (full error bars) uncertainties. The data are compared to the H1 measurement of $F_2^{c\bar{c}}$ using secondary vertex information (open symbols) [117, 118], where measurements at $Q^2 = 300\,\mathrm{GeV}^2$ are shifted to $Q^2 = 400\,\mathrm{GeV}^2$ using the NLO calculation [116]. The result of the PDF fit H1PDF2009 (shaded band) is also shown. The uncertainty band accounts for experimental, model and parametrisation uncertainties [119].

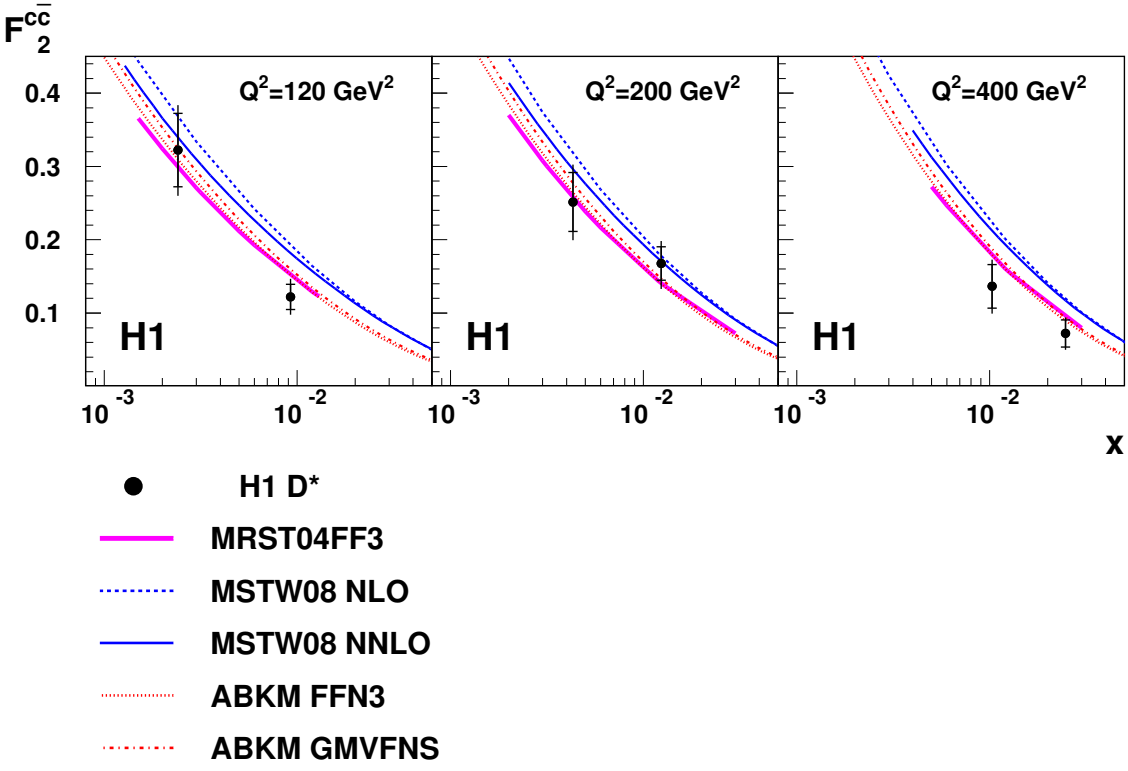

Figure 5.8: The charm contribution $F_2^{c\bar{c}}$ to the proton structure function. The data (closed symbols) are shown with statistical (inner error bars) and total (full error bars) uncertainties. The data are compared to the QCD predictions from the NLO calculation [116] in FFNS (light thick solid line). The predictions from the global PDF fits MSTW08 at NLO (dashed) and NNLO (dark solid) as well as the results of the ABKM fit [120,121] at NNLO in FFNS (dotted) and GMVFNS (dashed-dotted) are also shown.

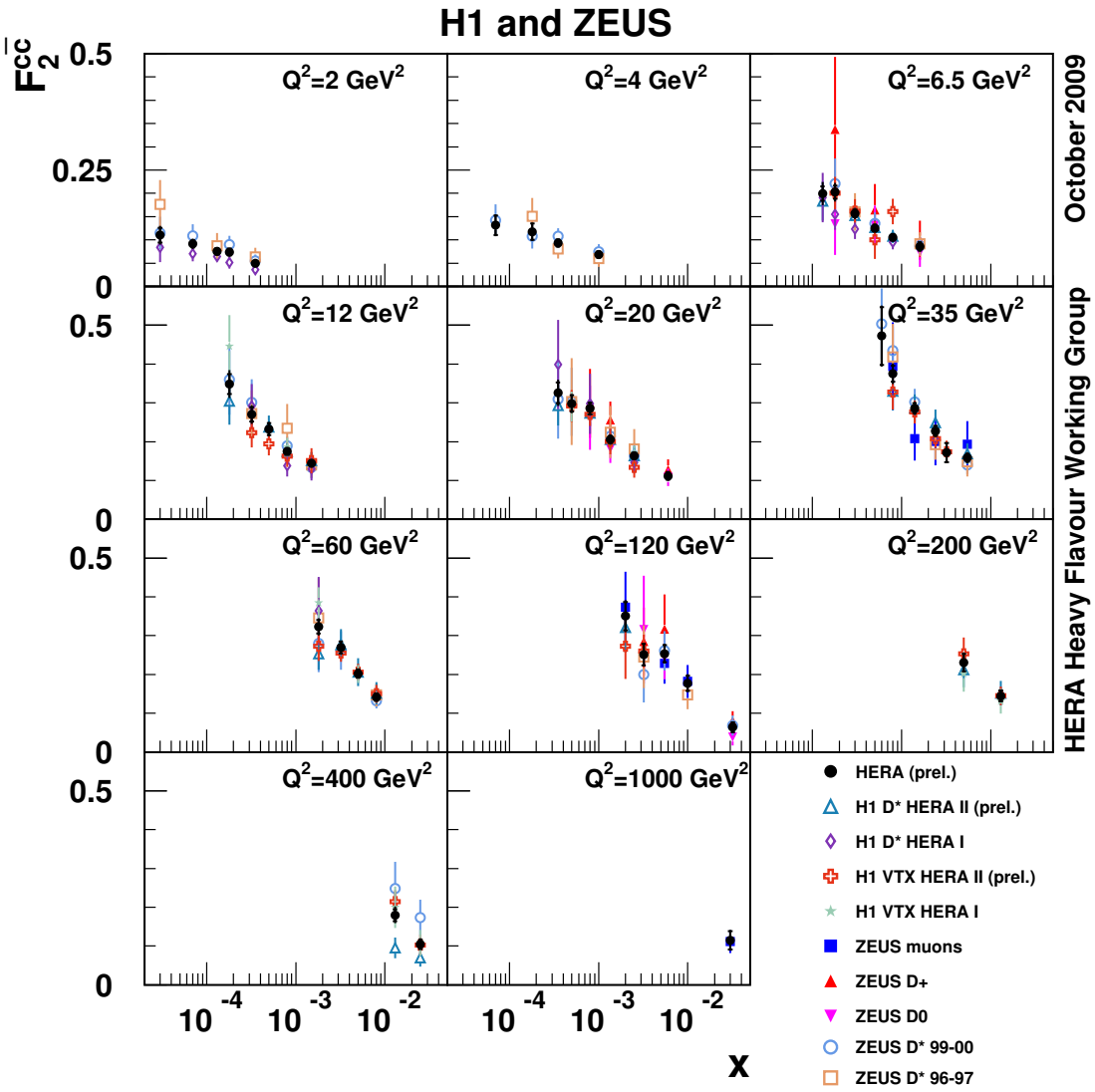

Figure 5.9: Charm contribution to the proton structure function, $F_2^{c\bar{c}}$, as a function of x in bins of Q^2. The averaged HERA $F_2^{c\bar{c}}$ (black circles) is compared to the data sets of the H1 and ZEUS measurement used for the combination. The results of this analysis are represented by open triangles in the bins according to $\langle Q^2 \rangle = 120, 200, 400\,\mathrm{GeV}^2$. The different measurements are interpolated to the common Q^2,x-values. The inner (full) error bars of the averaged value represent the uncorrelated (total) uncertainties.

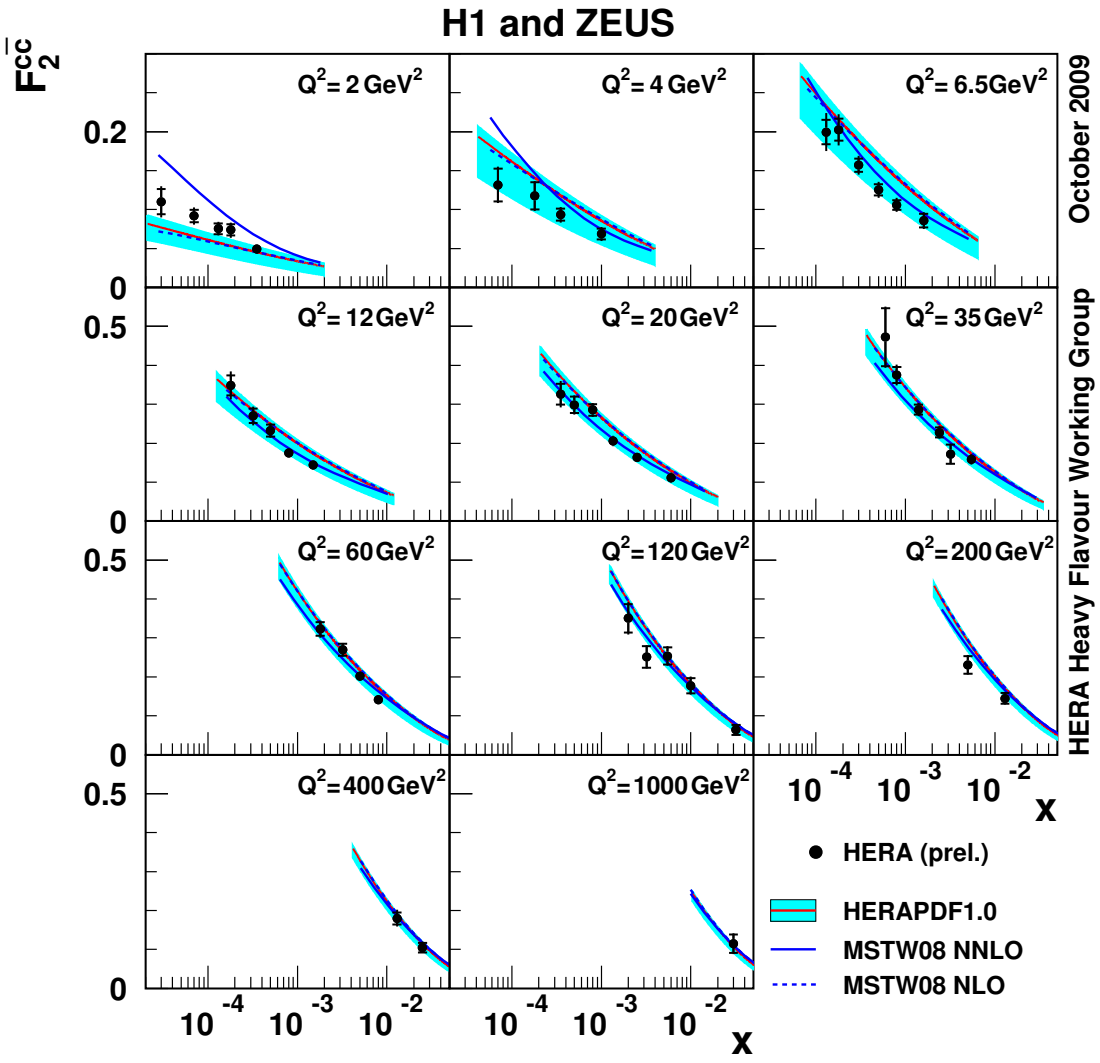

Figure 5.10: The HERA averaged $F_2^{c\bar{c}}$ (closed symbols) is shown with the uncorrelated (inner error bars) and the total (full error bars) uncertainties. The data are compared to the HERAPDF1.0 (band) and the predictions from the global PDF fits MSTW08 at NLO (dashed line) and NNLO (solid line).

Conclusions

The cross section for D^* production in ep collisions in deep inelastic scattering (DIS) at a center of mass energy $\sqrt{s} = 318\,\mathrm{GeV}$ is measured in the kinematic region of the photon virtuality $100 < Q^2 < 1000\,\mathrm{GeV}^2$ and inelasticity $0.02 < y < 0.7$ for the first time with the H1 experiment. This measurement is based on the full HERA II data taking period corresponding to an integrated luminosity of $351\,\mathrm{pb}^{-1}$. In total 646 ± 42 D^* mesons are reconstructed in the visible range defined by additional restrictions on the transverse momentum and pseudorapidity of the D^* meson to $p_t(D^*) > 1.5\,\mathrm{GeV}$ and $|\eta(D^*)| < 1.5$, respectively.

For the reconstruction of DIS events the scattered electron is detected either in the main calorimeter or in a calorimeter located in the backward region. The range in Q^2 covered by this analysis includes the overlap region between both calorimeters with an acceptance gap. Within this thesis this overlap region has been better understood using an improved detector simulation and calibration. This guarantees a good quality of the electron measurement which is crucial for the reconstruction of the event kinematics.

The D^* mesons are reconstructed in the decay channel $D^{*\pm} \to D^0\pi^\pm_{slow} \to (K^\mp\pi^\pm)\pi^\pm_{slow}$ using the tracks in the central tracking detector. Due to statistical limitations an optimisation of the signal to background ratio is essential for the analysis. A cut on $p_t(D^*)$ has been applied to take the transverse Q^2-dependent boost of the hadronic final state into account. The signal to background ratio has been improved in total by a factor of three compared to the sample defined without this cut allowing a wider kinematic range coverage. Further improvement is achieved by additional requirements on the decay topology of the D^*.

Single and double differential cross sections have been measured with an experimental precision of about 20%. The data are compared to various predictions from calculations in quantum chromodynamics (QCD). The D^* kinematical distributions are not described well by the predictions of the Monte Carlo simulations RAPGAP and CASCADE in shape and normalisation. The massive NLO calculation in the fixed flavour number scheme (FFNS) provided by the HVQDIS program however agrees with the data within the theoretical uncertainties. The double differential cross sections in bins of Q^2 and y are well described by the HVQDIS calculation.

The same holds for CASCADE, while RAPGAP significantly overestimates the visible cross section. The poor description of the data by RAPGAP can be coused by missing contributions in the LO matrix elements in the Monte Carlo. On the other hand, inproper gluon distribution function used in such a Monte Carlo program could result in a wrong cross section prediction. No consistent set of PDFs for a LO Monte Carlo with higher order corrections mimiked by parton showers exist at the moment. The disagreement of CASCADE with the data could originate from a too soft simulated p_t spectrum due to an inproper gluon k_t of the unintegrated gluon density at high Q^2.

The data are also compared to the prediction in the zero mass variable flavour number scheme (ZMVFNS). This calculation is limited to the transverse D^* momentum in the photon-proton center of mass frame $p_t^*(D^*)$, namely $p_t^*(D^*) > 2\,\mathrm{GeV}$. Therefore this additional cut is applied to the data. In this phase space however the ZMVFNS prediction fails to describe the data whereas HVQDIS still agrees well with the data. In general, massive calculations of charm production at NLO in the FFNS are expected to break down at a scale $\mu = Q$ much larger than the charm mass m_c. Contrary to this expectations, FFNS describes the data well also at larger photon virtualities Q^2. The disagreement between the data and the ZMVFNS prediction is mostly at lower $p_t(D^*)$ whereas the corresponding distributions in bins of Q^2 disagree only in normalisation. Such, the possible conclusion could be that not the photon virtuality Q, but rather $p_t^*(D^*)$, should be taken as a relevant energy scale. In the kinematic range of D^* production at HERA, the average $p_t^*(D^*)$ is $2\,\mathrm{GeV}$, which is of the order of m_c.

The charm contribution $F_2^{c\bar{c}}$ to the proton structure function F_2 is determined. HVQDIS is used for the extrapolation of the visible D^* cross sections to the full phase space in $p_t(D^*)$ and $\eta(D^*)$. The model uncertainties are found to be small in the kinematic region studied. The measured $F_2^{c\bar{c}}$ is in reasonable agreement with the results from other H1 and ZEUS measurements. The data are compared to QCD predictions at NLO in the FFNS scheme as well as to the expectations from global fit analyses, using GMVFNS implementations at NLO and NNLO. The FFNS prediction describes the measurement well. The data indicate that the NLO FFNS provides the best description of D^* production and $F_2^{c\bar{c}}$ in the kinematic region of the analysis.

The results of this analysis were used in the combination of the $F_2^{c\bar{c}}$ measurements by both H1 and ZEUS experiments using different charm tagging methods. This combined result covers the kinematic range of photon virtuality $2 < Q^2 < 1000\,\mathrm{GeV}^2$ and $10^{-5} < x < 10^{-1}$. Results of this thesis contribute to the Q^2 bins at $\langle Q^2 \rangle = 120, 200, 400\,\mathrm{GeV}^2$. The combined $F_2^{c\bar{c}}$ is compared to predictions from the QCD analyses of different PDF fit groups in FFNS and GMVFNS in NLO and NNLO. Such different schemes of heavy flavour treatment in PDF fits can be tested in a wide range of Q^2. The test of reliability of different ways of implementation of GMVFNS

in the PDF fits is one of the key issues in the QCD analyses and description of the nucleon structure: It has been shown that ZMVFNS fails to describe most of the DIS data in the range of medium Q^2, where most of the HERA data contribute. On the other hand, the PDF fits in the FFNS are limited to neutral current data since no prescription of FFNS fits to the charged current data exist. Such, heavy flavour production at HERA is an elegant tool to test different implementations of GMVFNS. The full HERA-combined measurement of $F_2^{c\bar{c}}$ is on the way to its final precision, but already now has the power to distinguish between different approaches. It is planned to use this combined $F_2^{c\bar{c}}$ together with inclusive HERA data for a new PDF fit with the aim of a better constraint of some parameters like the charm mass. In this new PDF fit the measurement presented in this thesis will be included.

Appendix A

Tables of Results

variable	bin	cross section		δ_{stat}[%]	δ_{uncorr}[%]	δ_{corr}[%]
$p_T(D^*)$ [GeV]	1.5 – 6.0	$\frac{d\sigma}{dp_T}[\frac{\text{pb}}{\text{GeV}}]$	27.8	11.1	7.4	$^{+9.2}_{-8.9}$
	6.0 – 9.5		17.8	9.1	8.3	$^{+8.3}_{-8.4}$
	9.5 – 20		3.31	11.4	11.6	$^{+8.1}_{-8.1}$
$\eta(D^*)$	-1.5 – -0.6	$\frac{d\sigma}{d\eta}$[pb]	51.5	12.0	7.5	$^{+7.4}_{-7.4}$
	-0.6 – 0.7		94.9	8.4	8.5	$^{+9.7}_{-9.6}$
	0.7 – 1.5		68.1	16.4	8.8	$^{+8.0}_{-8.2}$
$z(D^*)$	0.0 – 0.3	$\frac{d\sigma}{dz}$[pb]	233.6	17.3	7.8	$^{+8.9}_{-8.7}$
	0.3 – 0.6		327.9	8.4	8.3	$^{+8.6}_{-8.7}$
	0.6 – 1.0		134.8	8.8	9.0	$^{+14.5}_{-13.8}$
$\log(\frac{Q^2}{\text{GeV}^2})$	2.0 – 2.2	$\frac{d\sigma}{d\text{Q}^2}[\frac{\text{pb}}{\text{GeV}^2}]$	1.88	10.1	7.6	$^{+8.6}_{-8.7}$
	2.2 – 2.4		0.767	10.0	8.2	$^{+7.7}_{-7.6}$
	2.4 – 3.0		0.0572	15.7	9.6	$^{+9.7}_{-9.7}$
$\log(x)$	-2.8 – -2.4	$\frac{d\sigma}{dx}$[pb]	24787	13.2	7.6	$^{+6.9}_{-7.2}$
	-2.4 – -2.0		15993	9.5	8.0	$^{+9.5}_{-9.1}$
	-2.0 – -1.2		1292	12.3	9.2	$^{+10.2}_{-10.2}$

Table A.1: Single differential cross sections for $D^{*\pm}$ production averaged over bins of Q^2, x and the meson kinematics, $p_T(D^*)$, $\eta(D^*)$ and $z(D^*)$, as measured in the visible range defined in Tab. 3.2. The central values of the cross section are listed together with relative statistical (δ_{stat}), uncorrelated (δ_{uncorr}) and correlated (δ_{corr}) systematic uncertainties.

variable	bin	cross section		δ_{stat}[%]	δ_{uncorr}[%]	δ_{corr}[%]
$p_T(D^*)$ [GeV]	1.5 – 6.0	$\frac{d\sigma}{dp_T}[\frac{\text{pb}}{\text{GeV}}]$	16.6	11.8	7.5	$^{+7.3}_{-7.4}$
	6.0 – 10		11.4	9.6	8.5	$^{+10.1}_{-10.2}$
	10 – 20		2.25	13.3	12.1	$^{+6.7}_{-6.7}$
$p_T^*(D^*)$ [GeV]	2 – 3	$\frac{d\sigma}{dp_T^*}[\frac{\text{pb}}{\text{GeV}}]$	60.0	13.3	7.9	$^{+7.0}_{-6.9}$
	3 – 5		26.8	10.9	8.3	$^{+8.6}_{-8.8}$
	5 – 10		6.21	11.4	9.4	$^{+18.7}_{-18.8}$
$\eta(D^*)$	-1.5 – -0.5	$\frac{d\sigma}{d\eta}$[pb]	28.9	14.3	7.3	$^{+7.5}_{-7.7}$
	-0.5 – 0.5		61.6	10.2	8.9	$^{+7.2}_{-7.2}$
	0.5 – 1.5		60.2	11.2	8.8	$^{+10.1}_{-10.3}$
$\log(\frac{Q^2}{\text{GeV}^2})$	2.0 – 2.2	$\frac{d\sigma}{dQ^2}[\frac{\text{pb}}{\text{GeV}^2}]$	1.20	10.5	7.8	$^{+8.1}_{-8.6}$
	2.2 – 2.4		0.475	11.0	8.3	$^{+7.0}_{-6.9}$
	2.4 – 3.0		0.0470	13.5	9.7	$^{+7.2}_{-7.2}$
$\log(x)$	-2.8 – -2.4	$\frac{d\sigma}{dx}$[pb]	15508	15.1	7.7	$^{+6.4}_{-6.7}$
	-2.4 – -2.0		10876	10.2	8.4	$^{+6.8}_{-6.8}$
	-2.0 – -1.2		878	11.3	9.3	$^{+8.6}_{-8.4}$

Table A.2: Single differential cross sections for $D^{*\pm}$ production averaged over bins of Q^2, x and the meson kinematics, $p_T(D^*)$, $p_T^*(D^*)$ and $\eta(D^*)$, as measured for $p_t(D^*) > 2\,\text{GeV}$. The central values of the cross section are listed together with relative statistical (δ_{stat}), uncorrelated (δ_{uncorr}) and correlated (δ_{corr}) systematic uncertainties.

$\log(\frac{Q^2}{\text{GeV}^2})$	y	$\frac{d^2\sigma}{dQ^2dy}[\frac{pb}{\text{GeV}^2}]$	δ_{stat}[%]	δ_{uncorr}[%]	δ_{corr}(%)
2.0 – 2.2	0.020 – 0.350	3.39	13.7	7.6	$^{+11.6}_{-10.8}$
2.0 – 2.2	0.350 – 0.700	2.11	14.8	7.6	$^{+6.4}_{-6.7}$
2.2 – 2.4	0.020 – 0.300	1.61	13.3	8.2	$^{+8.0}_{-7.9}$
2.2 – 2.4	0.300 – 0.700	0.810	15.0	8.2	$^{+7.6}_{-7.4}$
2.4 – 3.0	0.020 – 0.275	0.0921	24.8	9.6	$^{+10.5}_{-10.4}$
2.4 – 3.0	0.275 – 0.700	0.0803	20.2	9.6	$^{+9.7}_{-9.7}$

Table A.3: Double differential cross sections for $D^{*\pm}$ production averaged over bins of Q^2 and y as measured in the visible range defined in Tab. 3.2. The central values of the cross section are listed together with relative statistical (δ_{stat}), uncorrelated (δ_{uncorr}) and correlated (δ_{corr}) systematic uncertainties.

bin	$< Q^2 >$ [GeV^2]	$< x >$	$F_2^{c\bar{c}}$	δ_{exp} [%]	δ_{extr} [%]	$\sigma_{vis}/\sigma_{tot}$	δ_{stat} [%]	δ_{uc} [%]	δ_{uc}^{sig} [%]	$\delta_{uc}^{D^0 win}$ [%]	δ_{uc}^{rad} [%]	δ_{uc}^{refl} [%]
1	120	0.00924	0.122	$\pm$ 20	$^{+3.2}_{-3.8}$	0.53	14	5.9	5.0	2.8	1.5	0.5
2	120	0.00241	0.322	$\pm$ 19	$^{+3.4}_{-4.8}$	0.63	15	5.9	5.0	2.8	1.5	0.5
3	200	0.01240	0.168	$\pm$ 18	$^{+3.8}_{-4.6}$	0.48	13	6.6	5.0	4.0	1.5	0.5
4	200	0.00432	0.251	$\pm$ 20	$^{+3.3}_{-3.5}$	0.67	15	6.6	5.0	4.0	1.5	0.5
5	400	0.02480	0.072	$\pm$ 30	$^{+6.5}_{-5.9}$	0.43	25	8.3	5.0	6.4	1.5	0.5
6	400	0.01030	0.136	$\pm$ 26	$^{+3.7}_{-3.8}$	0.71	20	8.3	5.0	6.4	1.5	0.5

Table A.4: The measured values and relative errors for the charm contribution to the proton structure function $F_2^{c\bar{c}}$. The results are obtained from the measured cross sections using the NLO calculation. Relative experimental (statistical and systematic errors added in quadrature) and the extrapolation uncertainties are listed, respectively. Extrapolation uncertainties are obtained from the variation of the input parameters for the calculations of the extrapolation factors and should be treated as correlated between data points. The fractions of the total D^* cross section in the visible phase space $\sigma_{vis}/\sigma_{tot}$ are also given. Further are listed the individual contributions to the experimental error namely the statistical error δ_{stat} and the uncorrelated error δ_{uc} as well as its different contributions from signal extraction δ_{uc}^{sig}, D^0 mass window $\delta_{uc}^{D^0 win}$, radiative corrections δ_{uc}^{rad} and reflections δ_{uc}^{refl}. The listing of the individual error sources continues in Tab. A.5

bin	δ_c [%]	δ_c^{mod} [%]	δ_c^{lum} [%]	$\delta_c^{\theta_e}$ [%]	$\delta_c^{E'_e}$ [%]	δ_c^{BR} [%]	$\delta_c^{\gamma p-bck}$ [%]	δ_c^{tri} [%]	δ_c^{fr} [%]	$\delta_c^{E_{had}}$ [%]	δ_{pc} [%]	δ_{pc}^{trck} [%]	δ_{pc}^{vf} [%]	δ_{pc}^{eltr} [%]
1	$^{+10.5}_{-9.7}$	4.7	3.2	$^{+6.8}_{-6.1}$	$^{+5.2}_{-4.5}$	1.5	1.2	1.0	$^{+0.2}_{-0.2}$	$^{+0.5}_{-0.5}$	6.8	6.0	2.5	2.0
2	$^{+4.2}_{-4.7}$	0.9	3.2	$^{+0.0}_{-0.7}$	$^{+0.0}_{-1.4}$	1.5	1.2	1.0	$^{+0.6}_{-0.6}$	$^{+1.5}_{-1.8}$	6.8	6.0	2.5	2.0
3	$^{+6.4}_{-6.3}$	4.5	3.2	$^{+0.5}_{-0.0}$	$^{+2.2}_{-1.4}$	1.5	1.2	1.0	$^{+0.4}_{-0.4}$	$^{+0.9}_{-1.2}$	6.8	6.0	2.5	2.0
4	$^{+5.9}_{-5.6}$	3.6	3.2	$^{+1.8}_{-1.0}$	$^{+1.0}_{-0.1}$	1.5	1.2	1.0	$^{+0.7}_{-0.6}$	$^{+1.7}_{-1.4}$	6.8	6.0	2.5	2.0
5	$^{+9.3}_{-9.2}$	7.4	3.2	$^{+1.2}_{-1.7}$	$^{+3.7}_{-3.5}$	1.5	1.2	1.0	$^{+0.2}_{-0.2}$	$^{+1.5}_{-1.1}$	6.8	6.0	2.5	2.0
6	$^{+8.4}_{-8.4}$	7.2	3.2	$^{+0.8}_{-1.0}$	$^{+0.0}_{-0.2}$	1.5	1.2	1.0	$^{+0.6}_{-0.5}$	$^{+1.4}_{-1.6}$	6.8	6.0	2.5	2.0

Table A.5: The listing of the individual systematic errors continued from Tab. A.4. Shown are the correlated errors concerning: model uncertainty δ_c^{mod}, luminosity measurement δ_c^{lum}, electron theta $\delta_c^{\theta_e}$ and energy measurement $\delta_c^{E'_e}$, branching fraction δ_c^{BR}, photoproduction background $\delta_c^{\gamma p-bck}$, trigger efficiency δ_c^{tri}, fragmentation δ_c^{fr} and measurement of the hadronic final state energy $\delta_c^{E_{had}}$. Further shown the individual partially correlated errors concerning: track finding efficiency δ_{pc}^{trck}, vertex fit efficiency δ_{pc}^{vf} and matching of the electron track δ_{pc}^{eltr}.

Appendix B

Track Efficiency Studies

The goal of these studies is to determine the p_t dependent total track reconstruction efficiency for low momentum tracks in the central tracking detector (CJC1/2) of the H1 experiment. Within this effort the efficiency has to be determined on a data-driven level. The efficiency obtained from data is compared to that determined using the Monte Carlo simulation.

The total track reconstruction efficiency relevant for a physics analysis can be split into several contributions:

- the probability that a charged particle reaches the detector is smaller than unity due to interactions with the material and its finite lifetime,
- the efficiency to reconstruct a non vertex fitted track from the signals caused by a charged particle going through the CJC,
- the efficiency of a reconstructed track originating from the primary ep-interaction vertex being fitted to the reconstructed primary vertex and
- the limited acceptance of the detector in p_t and η.

Two different approaches are used to determine the total reconstruction efficiency. The first method is based on the fact that tracks of small p_t curl up in the CJC. Per turn two track segments are expected and the reconstruction efficiency is determined by searches for matches, where the standard helix parametrization described by the five parameters κ, dca, ϕ, θ and z_0 is used (see Sec. 2.3.3). By applying appropiate criteria the background in the matching distributions is reduced significantly. Due to the geometry of the CJC and the magnetic field this method is only valid for transverse momenta $p_t < 0.15\,\mathrm{GeV}$.

With the second algorithm one can calculate the p_t dependence of the reconstruction efficiency in the region of $0.07 < p_t < 0.4\,\mathrm{GeV}$. This method was used for the first time in [126]. The idea is to use $K^0_S \to \pi^+\pi^-$, which shows an isotropic

decay. By comparing the expected and the measured p_t spectra of the pions the reconstruction efficiency may be deduced. The main assumption in this method is that the efficiency is only p_t dependent. The disadvantage is the unknown normalisation. Together with the curler method providing the absolute normalisation the estimation of the track reconstruction efficiency as a function of p_t up to $p_t = 0.4\,\mathrm{GeV}$ is possible.

B.1 Curler Method

In the following the curler method for determination of the track reconstruction efficiency will be presented. After a discussion of the principle behavior of curling particles and the corresponding reconstructed track segments, the selection of curlers will be described. From this selection the track reconstruction efficiency cannot be determined directly it rather provides a well defined sample on which the efficiency is obtained from scanning. The selection of curlers and some examples of scanned events are shown for inclusive DIS data. The results on the efficiencies are given for inclusive DIS Monte Carlo too. The determined efficiencies are for the track reconstruction and does not include the vertex fit efficiency.

B.1.1 Properties of Curling Tracks in CJC

Fig. B.1 illustrates the curler method. A curling track in the $r\phi$-plane is shown in a radial view of the CJC together with the CIP, COP and beampipe. On the bottom half expectations for curling particles at different p_t are shown without any interaction with material where the bending is calculated from Eq. 2.1 with a magnetic field of $B_z = 1.15\,\mathrm{T}$. The curling tracks are restricted to $p_t < 0.145\,\mathrm{GeV}$ since a large inefficiency for returning is expected for particles leaving the CJC through steel tank and calorimeter.

On the upper half of Fig. B.1 two sample curlers are shown where in both cases the particles originate from the primary vertex and curl up. Two segments each with the track parameters κ_1, κ_2, ϕ_1, ϕ_2 and $dca1$, dca_2 are available. In the following the track candidate caused by the returning of the particle is called return track with index 1 and the other start segment get the index 2. Without energy loss and multiple scattering one has the conditions $\kappa_1 + \kappa_2 = 0$, $\phi_1 - \phi_2 = \pm\pi$ and $dca_1 + dca_2 = 0$. Due to energy loss and multiple scattering these conditions are not fulfilled. The deviations are stronger for particles passing CJC2 due to multiple interactions in the dead material between CJC1 and CJC2.

Three regions in p_t are defined: tracks with $p_t < 0.075\,\mathrm{GeV}$ curl up in CJC1 where both halfs fit reasonably well[1]. Tracks with $0.1\,\mathrm{GeV} < p_t < 0.145\,\mathrm{GeV}$ curl

[1] The matching is not perfect because of finite resolution of the chamber and interactions of the

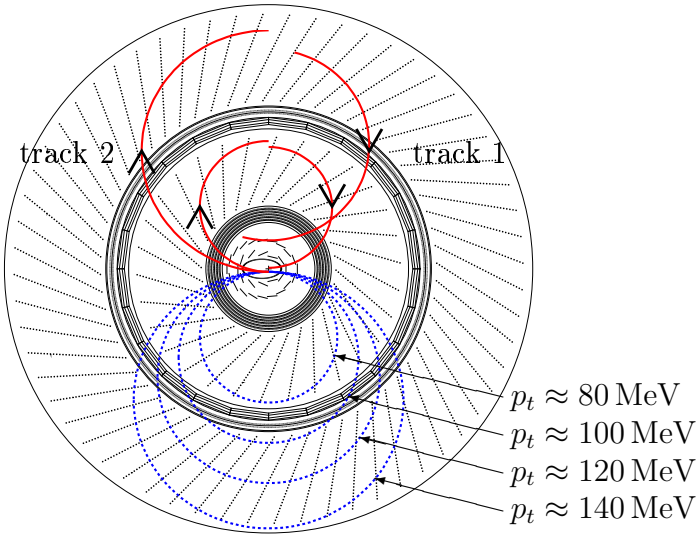

Figure B.1: Behavior of curling particles in the CJC in the r-ϕ plane. On the lower half the expected trajectories of curling particles with different p_t assuming a magnetic field of 1.15 T and no interaction with the material are shown. On the upper half a schematic view of both track segments reconstructed from the hits of real curlers are shown under consideration of energy loss and multiple scattering. Due to the energy loss the *dca* is larger for the return track. Due to multiple scattering ϕ of the return track is different from that of the incoming one. The effect of multiple interactions with the material is stronger for the curler reaching the CJC2 due to the material between the CJC1 and CJC2.

up in CJC2 where the energy loss leads to a large negative $dca_1 \cdot \mathrm{sgn}(\kappa_1)$ for the return track[2]. In addition the matching is affected by multiple scattering. The momentum region $0.075\,\mathrm{GeV} < p_t < 0.1\,\mathrm{GeV}$ where particles travel long distances in the material between CJC1 and CJC2 are difficult to match or even stop inside the dead material. They are therefore excluded from this study.

Concerning the helix parametrisation there are two additional parameters per track to be considered: the z positions of the track segments at *dca*, z_{01} and z_{02} and their polar angles θ_1 and θ_2. To describe the matching in z a parametrization of a helix in z is needed:

$$z = z_0 + s \tan\left(\frac{\pi}{2} - \theta\right). \tag{B.1}$$

particle with chamber gas and wires.

[2]In the used tracking conventions a $dca_1 \cdot \mathrm{sgn}(\kappa_1) < 0$ means that the origin is outside the circle in the $r\phi$ plane

Here s is the arc length in the $r\phi$ plane with $s = 2\pi/\kappa$ for one full turn. Applying this equation to the parameters of track 1 the z position extrapolated to the starting point of the curler $z_{01,ext}$ can be calculated:

$$z_{01,ext} = z_{01} + \left(\frac{2\pi}{\kappa_1}\right) \tan\left(\frac{\pi}{2} - \theta_1\right), \tag{B.2}$$

where for an ideal curler the matching condition $z_{01,ext} = z_{02}$ applies. In practice z has a large error of several cm as long as only the CJC information is used. Due to this large error $z_{01,ext}$ is matched to the z position of the primary vertex z_{vtx}. A direct matching in θ with the ideal matching condition $\theta_1 + \theta_2 = \pi$ is not applied due to large errors in the θ measurement.

In addition to the helix parameters, the time measurement provides further information for curler selection. The measured value associated to a track $t_{0,track}$ is called track - t_0 and corresponds to the time where the particle is in the middle of the measured arc segment. Due to the finite velocity of the particle the track - t_0 of the returning particle tends to larger values. For the curler selection, the difference $\Delta\, t_{0,event}$ to the event - t_0:

$$\Delta\, t_{0,event} = t_{0,track} - t_{0,CJC} \tag{B.3}$$

is used. As event - t_0 the average $t_{0,track}$ from all CJC tracks $t_{0,CJC}$ is taken.

B.1.2 Reconstruction of Curlers

For the reconstruction of curlers the track parametrisations before applying the vertex fit (non-vertex-fitted tracks) are used, the parameters of those are not corrected for the energy loss in the material between the vertex and the CJC1. To get a better matching of the track segments at the apex point[3] with respect to the energy loss between CJC1 and CJC2 a correction for tracks measured in the CJC1 extrapolated into the CJC2 is applied. For the correction a routine from the H1 reconstruction software is used which estimates an additive correction to the track parameters due to energy loss and multiple scattering. The sign of the correction is different for the incoming and outcoming track hypothesis[4]. With the (corrected) track parameters the position of the apex point for each track segment is calculated.

For the definition of the intervals of the transverse momentum in which the efficiency is calculated, the expected transverse momentum of the outgoing particle in CJC1 $p_{t1,exp}$ is used. In the case of CJC2 curlers where the apex point reaches

[3] point on helix after a half turn in r-ϕ relative to the point at dca

[4] Track 1 is always treated to be caused by an incoming particle and vice versa

the CJC2, $p_{t1,exp}$ is calculated from the parameters of track 1 by taking two times the energy loss in the material between CJC1 and CJC2 into account:

$$p_{t1,exp} = \frac{qB}{\kappa_1 - 2\Delta\kappa} \tag{B.4}$$

where κ_1 is the curvature of track 1 and $\Delta\kappa$ the additive correction due to the energy loss. For CJC1 curlers no correction is applied and therefore $p_{t1,exp} = p_{t1} = qB/\kappa_1$ is used.

The reconstruction of curling tracks of particles starting at the vertex is made in three steps: first the selection criteria of the return track 1 are applied based on the curler properties discussed in Sec. B.1.1. These selection criteria have to ensure that this track is caused by an incoming particle which started at the vertex. The shape of the distributions in the parameters of track 1 are compared for the two cases where a second track has been matched successfully and no successful match, respectively. The requirements on track 1 are optimized such that these distributions agree reasonably well. In the second step, the track candidates of outgoing particles (track 2) for matching are selected. For candidates for which the reconstruction efficiency is determined, only minimal cuts are applied. Finally both halfs are matched. The requirements on the tracks and the matching criteria are summarized in Tab. B.1 and are described in more detail in the following.

Selection of the Return Track 1

The selection cuts of track 1 are listed in the upper part of Tab. B.1. The different transverse moment ranges of the tracks are chosen to define the different analysis samples: CJC1 curlers and CJC2 curlers. These requirements are based on the transverse momenta expected for the outgoing particle in CJC1 $p_{t1,exp}$ (see Eq. B.4).

The requirements on dca, which ensures that the selected track 1 is indeed the return track are illustrated in Fig. B.2. In the upper two plots $dca_1 sgn(\kappa_1)$ is plotted versus p_{t1} and is shown for the two cases: first where at least one outgoing track is matched according to the criteria described below and secondly with no successful matching. The distribution of $dca_1 sgn(\kappa_1)$ versus p_{t1} with match (a) shows the expected behavior of the p_t dependent energy loss for a curling particle originating from the vertex. The band covering the whole displayed momentum region corresponds to curlers which all reach the COZ and/or CJC2. The lower the p_t the longer is the path of the particle in the COZ material and the corresponding energy loss. Above the band mentioned above is completely separated the region of the curlers in CJC1, where a much smaller energy loss occurs. For the final sample only return tracks are taken into account according to the both boxes shown. The corresponding distribution without matched second track (Fig. B.2 b)) is much more uniform. This indicates that this distribution is background dominated i.e. most

quantity	cut
cuts on track 1	
CJC2: expected p_t of outgoing particle	$0.1\,\mathrm{GeV} < p_{t1,exp} < 0.14\,\mathrm{GeV}$
CJC1: expected p_t of outgoing particle	$0.06\,\mathrm{GeV} < p_{t1,exp} < 0.08\,\mathrm{GeV}$
CJC2: $\Delta t_{0,event}$	between lines in Fig. B.2 (c,d)
$dca_1 sgn(\kappa_1)$	see boxes in Fig. B.2 (a,b)
vertex constraint	no vertex fitted hypothesis
z position	$30\,\mathrm{cm} < \lvert z_{01}\rvert < 90\,\mathrm{cm}$
errors in z and θ	$\Delta z_{01} < 5\,\mathrm{cm}$ and $\Delta\theta_1 < 8^\circ$
expected z position at curler start	$\lvert z_{01,ext} - z_{vtx}\rvert < 20\,\mathrm{cm}$
start radius	$r_{1,start} < 50\,\mathrm{cm}$
radial tracklength	$s_{1,meas} > 15\,\mathrm{cm}$
cuts on track 2	
vertex constraint	require vertex fitted hypothesis
radial tracklength	$s_{2,meas} > 10\,\mathrm{cm}$
start radius	$r_{2,start} < 50\,\mathrm{cm}$
matching	
opposite sign of kappa	$\kappa_1\kappa_2 < 0$
CJC2: Matching of apex points:	$\lvert\Delta\phi\rvert < 20^\circ$; $d_{s\lvert\rvert} < 20\,\mathrm{cm}$
CJC1: Matching of apex points:	$\lvert\Delta\phi\rvert < 20^\circ$; $d_{s\lvert\rvert} < 10\,\mathrm{cm}$

Table B.1: Selection criteria for curling tracks.

of the selected track candidates are not real return tracks. To this background contribute especially tracks with larger p_t and larger $dca_1 sgn(\kappa_1)$ which arise from secondary vertices caused by nuclear interactions of the outgoing particles with the detector material as well as by decays.

The bottom half of Fig. B.2 shows the distributions in $\Delta t_{0,event}$ versus p_{t1} of the return tracks with matched second half (c) and without matched second half (d), respectively. For these plots the cuts on $p_{t1,exp}$ as listed in Tab. B.1 are applied. The lower part in both histograms corresponds to the CJC1 tracks and the upper part to tracks with the apex point in the CJC2. For the CJC2 tracks a clear shift in $\Delta t_{0,event}$ to larger values in case of matching is observed, which means that the track 1 sample is really enriched with "true" return tracks. The p_t dependence of $\Delta t_{0,event}$ is due to the fact that with increasing p_t the flight length of the particle becomes larger[5]. For the CJC1 tracks the shift in $\Delta t_{0,event}$ for the curlers is less distinct. For the selection of the curlers in CJC2 only the region between the red

[5]There is still a compensating effect due to the fact that the velocity of the particle increases in this p_t region significantely too (except electrons and positrons)

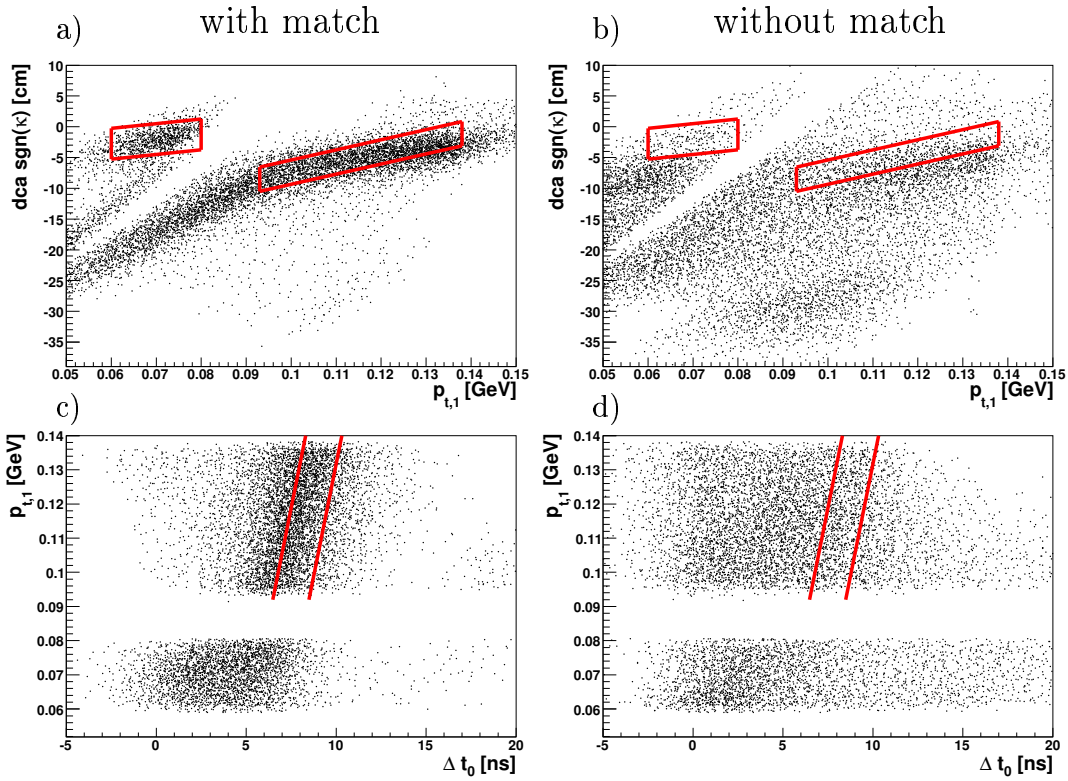

Figure B.2: Distributions of $dca_1 sgn(\kappa_1)$ and t_0 versus p_{t1} for complete curler candidates with successful (a,c) and unsuccessful matches (b,d). The applied cuts on track 1 are indicated by the lines.

lines is considered. This region has been set more to the right of the signal for better reduction of the background at smaller $\Delta t_{0,event}$. For the CJC1 curlers $\Delta t_{0,event}$ is not restricted.

In order to ensure that track 1 is really the return track and is not mistaken as outgoing particle further conditions are applied. It is required that the return track candidate is not fitted to the primary vertex. In Fig. B.3 a) the distribution in z_{01} vs. θ_1 of the return track candidates is shown. It can be seen that the region around the nominal vertex position at $z = 0$ is less dense because of the requirement that the track is not fitted to the primary vertex. The region between the red lines is rejected. The band shows the expected behavior of a return track from curling particles originating from the primary vertex: when $\theta_1 < 90°$ the value of z_{01} is negative while for $\theta_1 > 90°$ z_{01} is positive. To obtain the band the z position of track 1 extrapolated to the starting point of the curler $z_{01,ext}$ (see Eq. B.2) is matched to the z position of the primary vertex z_{vtx}. The distribution in $z_{01,ext} - z_{vtx}$ is shown in

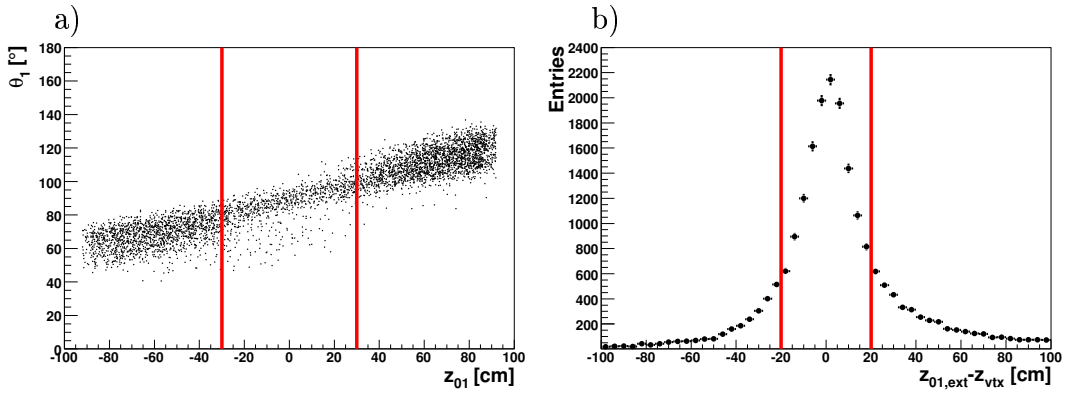

Figure B.3: Histogramm a) shows the distribution in z_{01} versus θ_1. The region between the red lines is rejected. In b) the difference $z_{01,ext} - z_{vtx}$ for the remaining tracks is shown of which only those between the red lines will be taken for the further selection.

Fig. B.3 b). Only the region between both lines is accepted. To make the restrictions in the z-θ-plane more effective further cuts on the errors of z_{01} and θ_1 according to Tab. B.1 are applied.

The requirement on the start radius of the track $r_{1,start}$ which is defined as the radial distance in the $r\phi$ plane from the origin to the first hit used in the track fit has been made to ensure that the return track starts in CJC1. If a particle passes through CJC2 it may lead to two independent tracks being reconstructed in CJC1 and CJC2 separately due to multiple scattering and energy loss in the dead material between the two jet chambers. The cut mentioned above is imposed to avoid double counting in such a case. To increase the general quality of the return track measurement, a minimum radial track lengh $s_{1,meas}$ defined as the arc length between the first and the last hit used in the track fit, is required in addition.

To test the quality of the curler selection for the efficiency determination the distribution in the track parameters p_{t1}, dca_1, ϕ_1, θ_1 and z_{01} as well as $\Delta t_{0,event}$ are compared for the two cases: successful match of at least one second track and no match. This comparison for the CJC1 curlers is shown in Fig. B.4 and for the CJC2 curler in Fig. B.5. A reasonable agreement in the shapes of all distributions is achieved. Especially no artificial inefficiencies are introduced due to the curler selection. However some deviations occur for example in case of p_{t1} for CJC1 curlers. The distribution in the case "with match" decreases at low p_{t1}. One reason for this behavior is the p_t dependence of the track reconstruction and vertex fit efficiency (see below). Another reason for the slightly different shapes of the distributions could be due to the behavior of the background which arises from wrongly matched tracks which are not part of the curler.

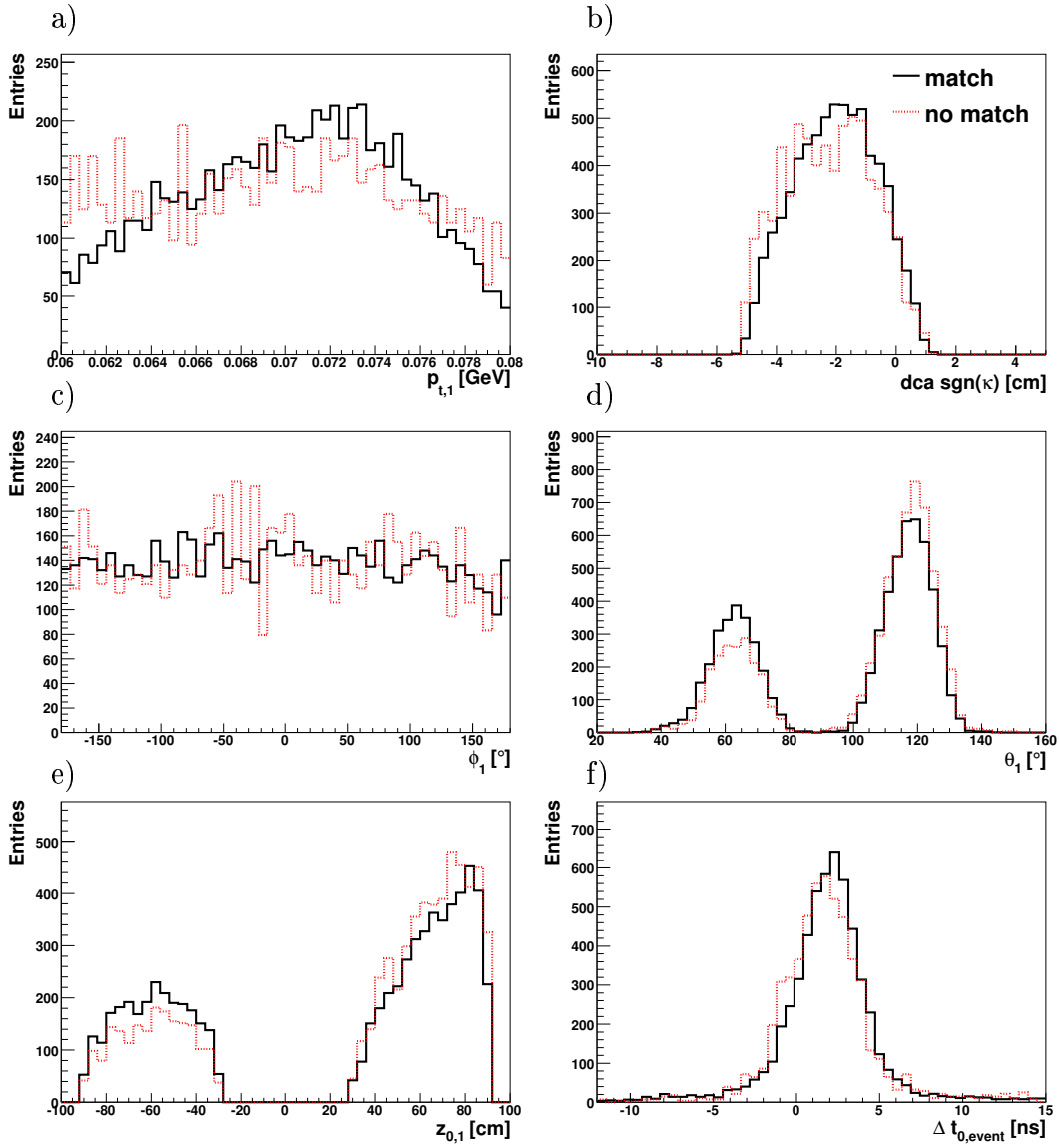

Figure B.4: Distributions in the track parameters p_{t1}, dca, ϕ_1, θ_1, z_{01} and $\Delta t_{0,event}$ for the CJC1 curlers in comparison with and without matched second track. The distributions are area normalized.

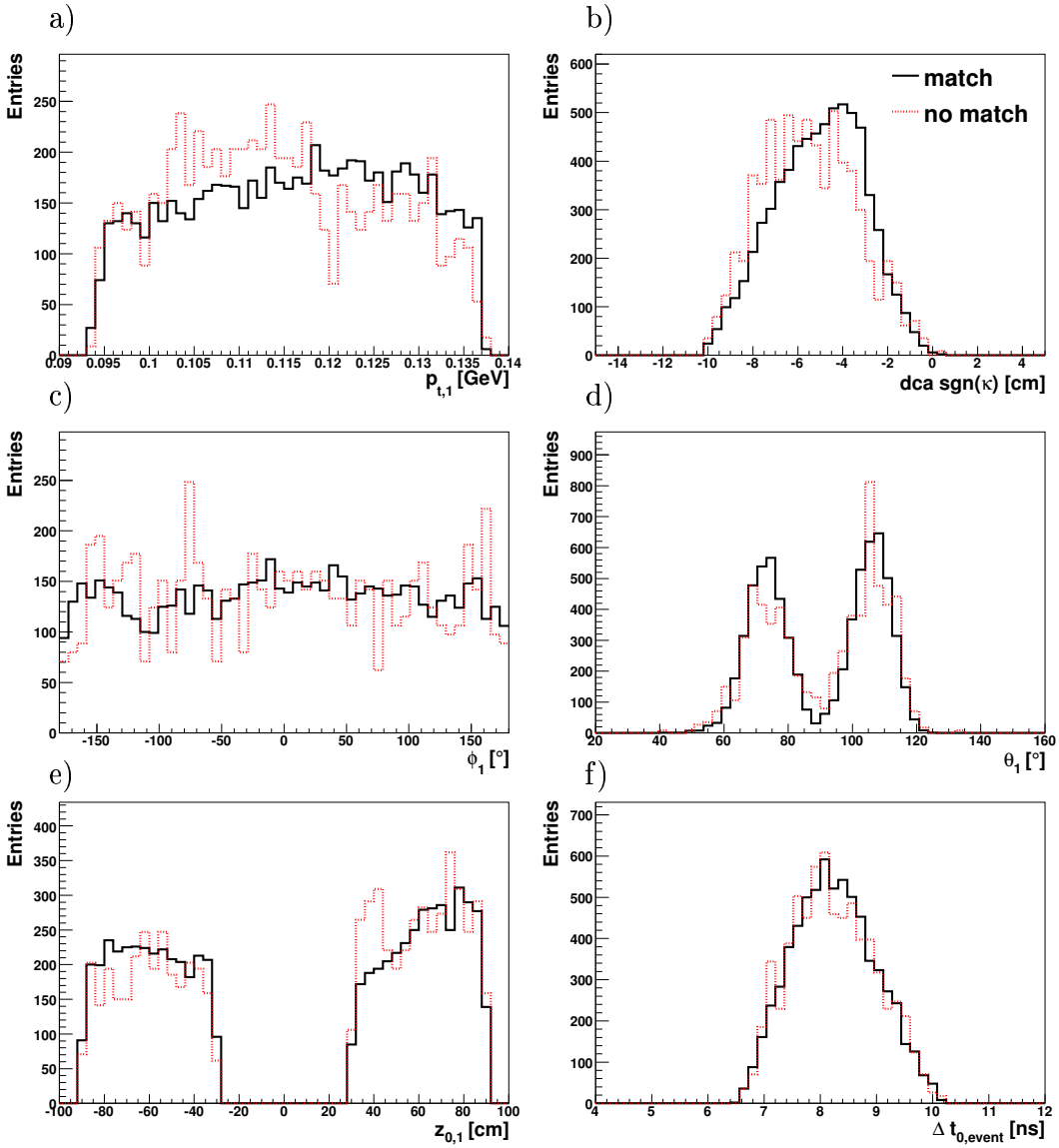

Figure B.5: Distributions in the track parameters p_{t1}, dca, ϕ_1, θ_1, z_{01} and $\Delta t_{0,event}$ for the CJC2 curlers in comparison with and without matched second track. The distributions are area normalized.

Selection of the Outgoing Track 2

For the second track only the minimal Lee-West criteria [127] of central tracks used in all analysis at H1 are applied according Tab. B.1: A corresponding vertex fitted hypothesis has to exist, a minimal radial tracklength $s_{2,meas}$ is required and the track has to start in CJC1 which is ensured by the requirement on the start radius $r_{2,start}$.

Matching

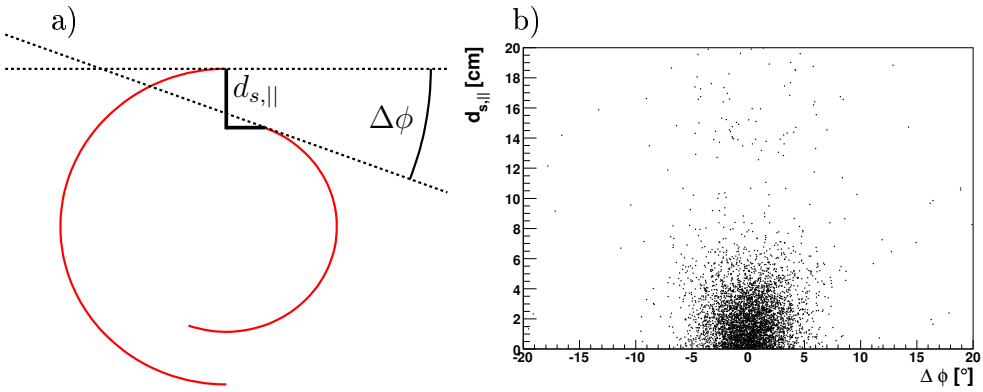

Figure B.6: Definition of the matching variables $d_{s,||}$ and $\Delta\phi$ at the apex point (a) and correlation between both variables (b).

The sign of the curvature κ is defined as opposite to the charge of the particle assuming outward going particles. A returning particle is treated like an outgoing particle with opposite charge. Therefore the first matching condition is the requirement that the curvatures κ_1 and κ_2 have opposite signs.

Further conditions are applied to match both segments at the apex. In Fig. B.6 a) the quantities $\Delta\phi$ [°] and a component of the distance vector of the two reconstructed apex points $d_{s||}$ [cm] are shown. The cut values for the CJC1 and CJC2 selection are listed in Tab. B.1. In Fig. B.6 b) both variables are plotted against each other. The curlers peak around the point $(0, 0)$ in the $\Delta\phi$, $d_{s||}$ plane where no correlations between both variables are observed. In case of more than one successful match, the track with the lowest $R^2_{match} = (\Delta\phi/°)^2 + (d_{s||}/cm)^2$ is defined as best match.

In Fig. B.7 the match multiplicities are shown for curlers in CJC1 and CJC2. In case of CJC1 the fraction of selected track 1 candidates with zero matches is about 20% and in about 3% of all cases more than one track is matched. For the CJC2 curler in only 10% of all cases no second track is matched and in about 8% of all cases the multiplicity is larger than one.

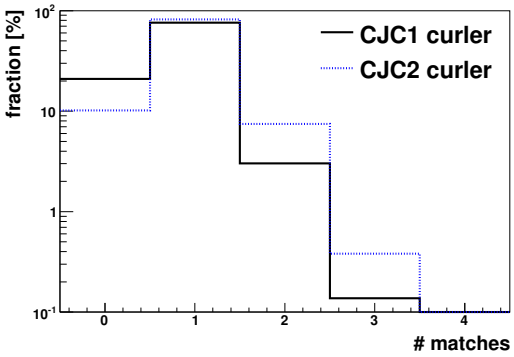

Figure B.7: Number of matches per track.

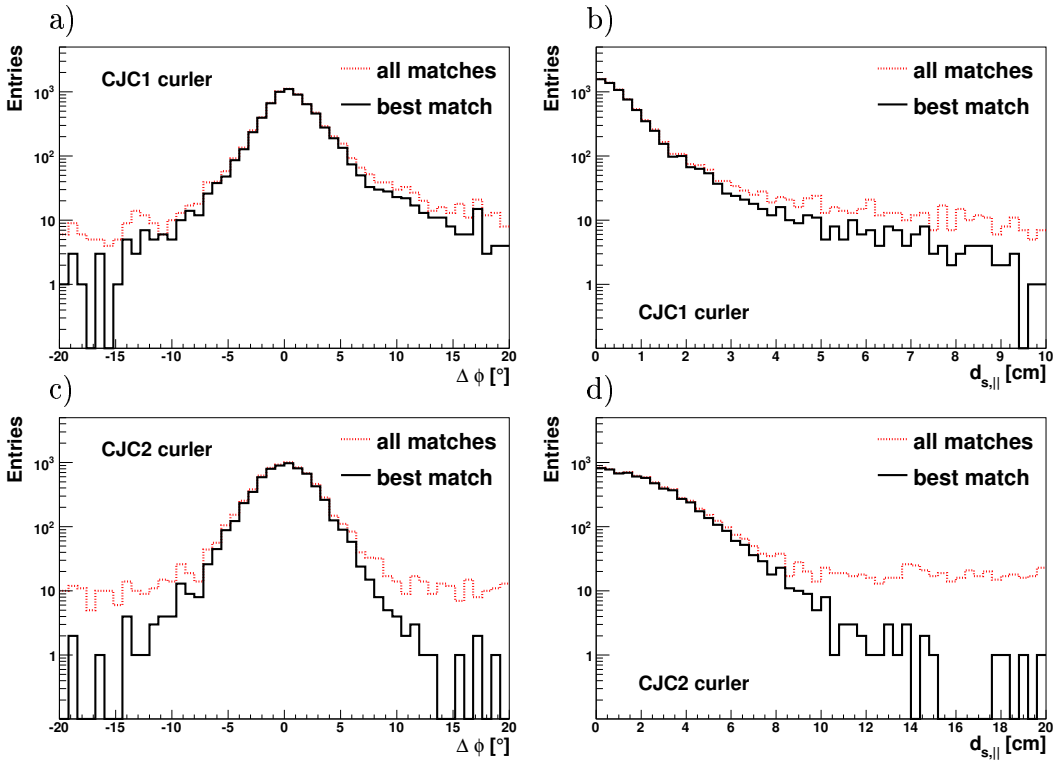

Figure B.8: Distribution in the matching variables $\Delta\phi$ and $d_{s||}$ for CJC1 (a,b) and CJC2 curlers (c,d). These are shown for all matches (dotted line) and the best match (solid line).

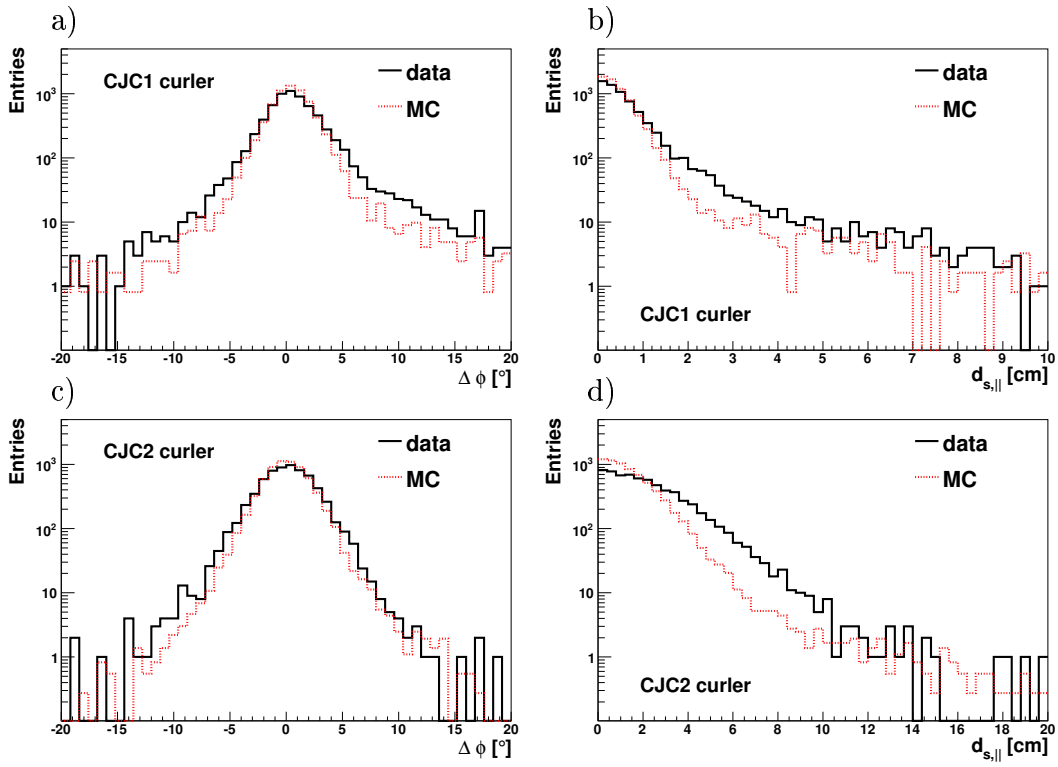

Figure B.9: Distribution in the matching variables $\Delta\phi$ and $d_{s||}$ for CJC1 (a,b) and CJC2 curlers (c,d) for the best match. These are shown for data (solid line) and MC (dotted line).

In Fig. B.8 the distributions in the matching parameters $\Delta\phi$ and $d_{s||}$ are shown for the CJC1 curlers (a,b) and the CJC2 curlers (c,d). The abscissa ranges shown correspond to the respective cut-acceptance regions. The distributions are shown for all matches and for the best match separately. For CJC2 curlers a constant background is visible in both matching variables which is significantly reduced when considering only the best match. For CJC1 curlers the background is also significantely reduced. In Fig. B.9 the same distributions for the best match are compared to the results from the Monte Carlo simulation. The distributions for the Monte Carlo sample are narrower than in data with the largest effect in $d_{s||}$ for the CJC2 curler. This discrepancy is due to the fact that in the Monte Carlo the dead material especially between CJC1 and CJC2 is not completely simulated.

B.1.3 Scanning of Events

The determination of the track reconstruction inefficiency is based on tracks not being matched by the preselection described in the previous section. The events containing such tracks are visually inspected using the H1 event display [128]. Since

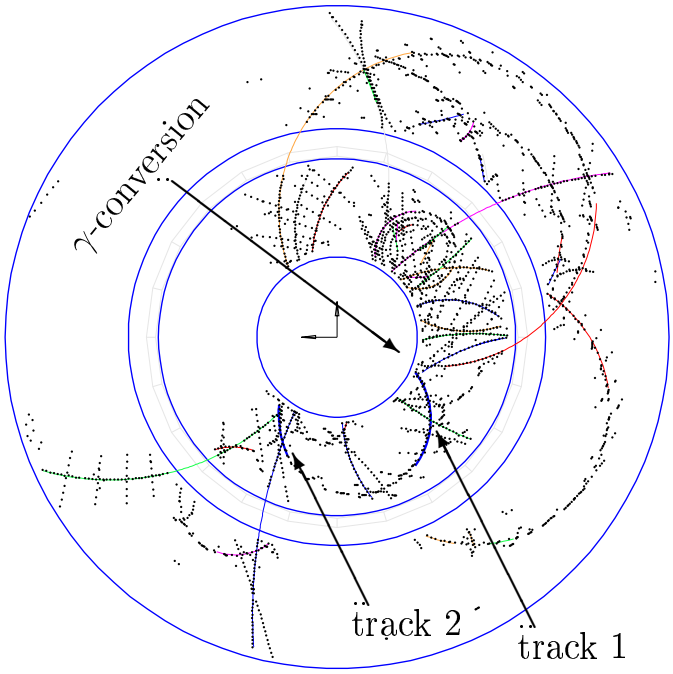

Figure B.10: Sample event in data with no matched second track visualized by an event display. Shown are the hits and fitted non vertex fitted tracks. Here the selected track 1 originates from a photon conversion. The second half of the curler is reconstructed but is not fitted to the primary vertex.

the matching probability of the preselection is very high (see Fig. B.7) the scanning of the unmatched tracks is more efficient than starting from an unselected sample. In many cases the preselection fails to find the match because of physics (e.g. decays or interactions) which may be identified by the scanning and thereby do not contribute to the reconstruction efficiency.

In Fig. B.10 an example for such a case is shown: an event is shown where no second track half is matched to the original one. Here the track 1 selected as return track candidate belongs to an outgoing positron originating from a photon conversion in the inner CJC wall and is therefore not fitted to the primary vertex. A second non vertex fitted track indicated as track 2 is matched but does also has not been fitted to the primary vertex bacause it is not a primary track.

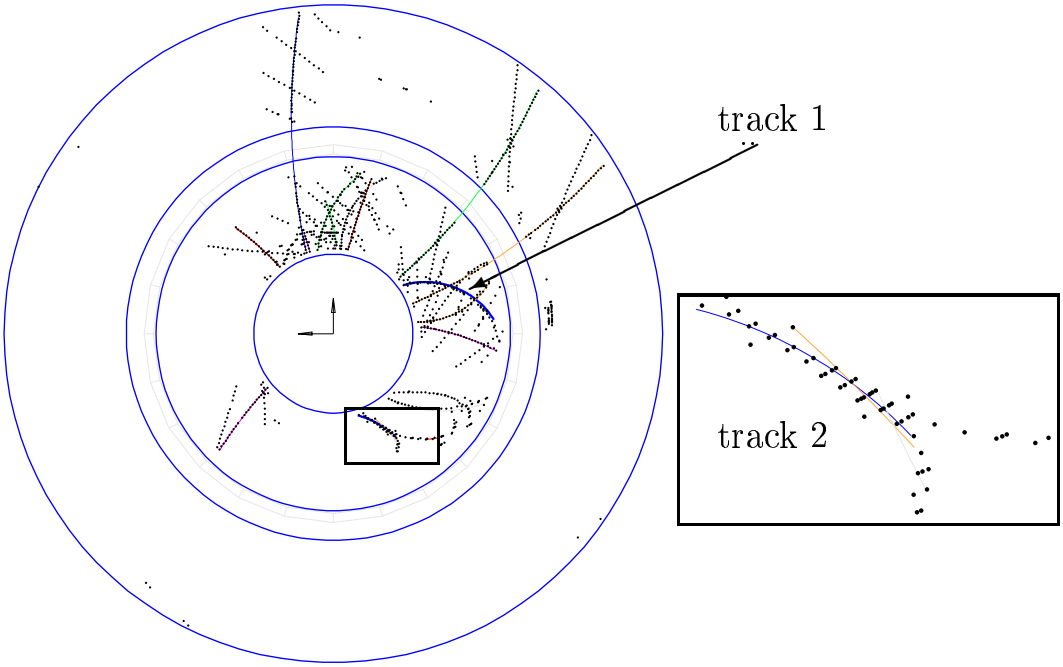

Figure B.11: An example for an event in data with no match to the reconstructed return track 1. In the region indicated by the small box where the proper track segment is expected a mirror track has been reconstructed. This region can be seen in an enlarged view according to the large box on the right.

During the scanning it is also possible to identify the different reasons for the reconstruction inefficiencies[6]. In Fig. B.11 an example for a reconstruction failure is shown. The enlarged region of the curler in which the second track is expected is shown in the box on the right. In this example the reconstruction software finds a mirror track (see Sec. 2.3.1).

Another problem in track reconstruction is shown in Fig. B.12. The enlarged region containing the curler (small box) is shown on the right. The second part of the curler goes through a region of high hit density. The expected track half is not reconstructed.

[6]This information has also been used to improve the reconstruction algorithm for reconstruction versions later than what has been used in this analysis.

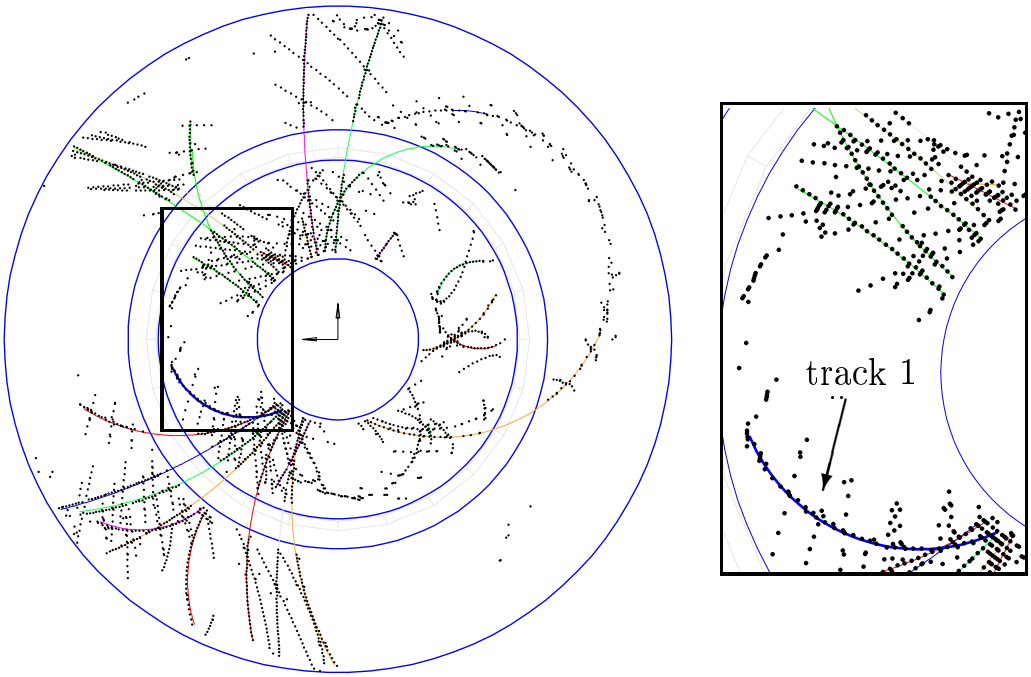

Figure B.12: An example for an event in data without a match to the reconstructed return track 1. An enlarged view of the region containing the curling track is shown on the right. The curling track goes through a region of high hit density where no proper track segment is reconstructed.

B.1.4 Track Reconstruction Efficiency

The track reconstruction efficiency is determined for data and Monte Carlo in three bins of the transverse momenta expected for the outgoing particle in CJC1 $p_{t1,exp}$: one bin for the CJC1 curler 60 MeV to 80 MeV and for the CJC2 curlers the two bins from 100 MeV to 120 MeV as well as 120 MeV to 140 MeV.

The efficiency is calculated for positive and negative tracks separately. Since only those curler candidates have to be scanned which were failing the matching criteria and which amount to $10-20\%$ only limited scanning statistics is needed for reasonable accuracy. Therefore in each case only the first 100 events with unsuccessful match are scanned. The track reconstruction efficiency is then calculated as follows:

$$\epsilon_{rec} = 1 - \frac{N_{norec}}{N_{tot} - N_{bck}}, \tag{B.5}$$

where N_{tot} is the total number of selected return track candidates (inclusive success-

negative tracks		
$p_{t1,exp}$[MeV]	ϵ(data)[%]	ϵ(Monte Carlo)[%]
$60-80$	98.6 ± 0.6	$> 99.6 \,@\, 90\%\, C.L.$
$100-120$	99.8 ± 0.15	$> 99.7 \,@\, 90\%\, C.L.$
$120-140$	99.9 ± 0.1	99.8 ± 0.14
positive tracks		
$p_{t1,exp}$[MeV]	ϵ(data)[%]	ϵ(Monte Carlo)[%]
$60-80$	86.2 ± 2.0	89.4 ± 1.4
$100-120$	98.9 ± 0.3	98.6 ± 0.5
$120-140$	99.3 ± 0.4	99.6 ± 0.2

Table B.2: Track reconstruction efficiencies determined from the curler method in bins of $p_{t1,exp}$ for both charges. Shown are the results obtained for data and Monte Carlo. For the two lower $p_{t1,exp}$ bins for negative tracks in Monte Carlo the 90% C.L. lower limit on the efficiency is given since $N_{norec} = 0$.

ful matches) and N_{bck} is the number of background events identified via scanning. To these background events curling particles contribute which do not originate from the primary vertex like photon conversions, nuclear interactions and decays as well as selected return track candidates not belonging to the first turn of the curling track. These background events are excluded. The quantity N_{norec} is the number of failed matches where the outgoing track has not or wrongly been reconstructed.

In Tab. B.2 the track reconstruction efficiency for data and Monte Carlo in bins of $p_{t1,exp}$ separated in charge of track 2 is summarized. In the two upper bins the efficiencies are larger than $98,9\%$. This inefficiency is much lower than the no match rate of the preselection of about 10% for CJC2 curler (see Fig. B.7) since most of the expected tracks are correctly reconstructed but not vertex fitted as required in the preselection. The difference in the track reconstruction efficiencies between data and Monte Carlo for the last two $p_{t1,exp}$ bins is less than 1%.

The efficiency for the lowest $p_{t1,exp}$ bin is significantly lower for positive than for negative tracks. This is because positive tracks at low momenta move almost parallel to the drift field which results in long pulses on the signal wires with bad timing information. This prevents the track of the particle being properly reconstructed.

B.2 K_S^0-Method

In this section the K_S^0-method to determine the relative p_t dependence of the track efficiency will be presented. After describing the algorithm, the selection of the K_S^0 sample will be described. Finally the results of the numerical estimation of the efficiencies using both data and Monte Carlo are compared to estimate a systematic error.

B.2.1 Algorithm

The isotropic decay of the K_S^0 in the decay channel $K_S^0 \to \pi^+\pi^-$ is considered. Let $f_{P_K}(p_t^+, p_t^-)$ be the normalized p_t spectrum of the decay pions in the laboratory frame with well defined four vector P_K of the kaons. $N_K(p_t^+, p_t^-)$ is defined as the measured p_t spectrum of decay pions of a produced K_S^0 sample. The measured spectrum is given as a sum over the $f_{P_K}(p_t^+, p_t^-)$ for each kaon produced:

$$\frac{d^2N_K}{dp_t^+\,dp_t^-} = \epsilon(p_t^+)\,\epsilon(p_t^-) \sum_{prod.\,K} f_{P_K}(p_t^+, p_t^-) = \epsilon(p_t^+)\epsilon(p_t^-) \sum_{rec.\,K} \frac{f_{P_K}(p_t^+, p_t^-)}{\epsilon^{P_K}} \qquad \text{(B.6)}$$

with

$$\epsilon^{P_K} = \int \epsilon(p_t^+)\epsilon(p_t^-) f_{P_K}(p_t^+, p_t^-) dp_t^+ dp_t^- \qquad \text{(B.7)}$$

where only a p_t depencence of the efficiency is assumed. The sum over the produced K_S^0 can be replaced by the sum over the reconstructed K_S^0 taking into account that a K_S^0 with well defined four vector P_K is reconstructed with the probability ϵ^{P_K}.

To get the p_t dependence of the efficiency an additional assumption is made: At p_t larger than a certain value $p_{t,max}$ no p_t dependence of the efficiency is assumed. Considering a subset of K_S^0 where one pion has $p_t > p_{t,max}$ and the second one $p_t < p_{t,max}$ named as π_s the equations B.6 and B.7 can be written as:

$$\frac{dN_{K^0}(p_{t,\pi_s})}{dp_{t,\pi_s}} = \epsilon(p_{t,\pi_s}) \sum_{rec.\,K^0} \frac{f_{P_K}(p_{t,\pi_s})}{\epsilon^{P_K}} \qquad \text{(B.8)}$$

with

$$\epsilon^{P_K} = \int \epsilon(p_{t,\pi_s}) f_{P_K}(p_{t,\pi_s}) dp_{t,\pi_s} \qquad \text{(B.9)}$$

If $\epsilon(p_{t,\pi_s})$ is a solution of Eq. B.8 the efficiency shifted by a global factor $\epsilon'(p_{t,\pi_s}) \to const * \epsilon(p_{t,\pi_s})$ solves the equation too. Hence only a p_t dependence of the efficiency can be estimated but not the absolute normalisation!

The equations are solved considering $N_{p_{t,\pi_s}}$ finite sized bins in the transverse momentum p_{t,π_s} of the slow pion as well as N_{θ_K} and $N_{p_{t,K}}$ bins in the polar angle θ_K

and transverse momentum $p_{t,K}$ of the kaon respectively. Here an axial symmetry in the azimuth angle ϕ of the kaon is assumed. The following system of equations is achieved:

$$N_K^m = \epsilon_m \sum_{j=1}^{N_{\theta_K}} \sum_{k=1}^{N_{p_{t,K}}} \tilde{N}_K^{j,k} \frac{f_{j,k}^m}{\epsilon^{j,k}} \quad , m = 1, ..., N_{p_{t,\pi_s}} \tag{B.10}$$

with

$$\epsilon^{j,k} = \sum_{m=1}^{N_{p_{t,\pi_s}}} \epsilon_m f_{j,k}^m. \tag{B.11}$$

The quantity N_K^m denotes the number of reconstructed kaons in the m-th bin in the transverse momentum of the slow pion p_{t,π_s}. On the right hand side of Eq. B.10 the reconstruction efficiency ϵ_m for the m-th bin is multiplied with a sum over the individual contributions from each $[\theta_K, p_{t,K}]$ bin with indices j,k, where $\tilde{N}_K^{j,k}$ is the number of reconstructed kaons in the particular $[\theta_K, p_{t,K}]$ bin. The probabilities $f_{j,k}^m$, that a reconstructed kaon falls in the m-th bin in p_{t,π_s} are estimated using the known isotropic decay topology in the rest frame of the kaon. Each term of the sum in Eq. B.10 is divided by the efficiency $\epsilon^{j,k}$ (Eq. B.11) for reconstructing a kaon in the particular $[\theta_K, p_{t,K}]$ bin.

For calculating the statistical error $\delta\epsilon_m$ of the efficiency ϵ_m in the m-th bin the fluctuations in the sum of Eq. B.10 are neglected since in the sum all reconstructed kaons are involved whereas on the left hand side of the equation only the kaons in the m-th bin are counted. Naming the sum with S, Eq. B.10 becomes $\epsilon_m = N_K^m/S$ with $\delta\epsilon_m = \delta N_K^m/S$. With a statistical error of $\delta N_K^m = \sqrt{N_K^m}$ the error on the efficiency becomes:

$$\delta\epsilon_m = \frac{\epsilon_m}{\sqrt{N_K^m}}. \tag{B.12}$$

B.2.2 K_S^0 Reconstruction

In order to estimate the efficiency ϵ_m in bins of p_{t,π_s} according to Eq. B.10 for data and Monte Carlo, a K_S^0 sample is selected from which the K_S^0 spectra $\tilde{N}_K^{j,k}$ as well as N_K^m are extracted. The reconstruction of the K_S^0 is performed in the decay channel $K_S^0 \to \pi^+\pi^-$. Due to the relatively long decay length of the K_S^0 with $c\tau = 2.68\,cm$ [93] the displacement of the decay vertex can be resolved using the CJC tracks. The selection of the K_S^0 is based on V^0 candidates found by the H1 reconstruction program. These are pairs of tracks with opposite curvature fitted to a common secondary vertex. The further selection criteria for K_S^0 are summarized in Tab. B.3.

To take into account the limited acceptance of the CJC several requirements on the polar angles and transverse momenta of the K_S^0 and their decay tracks as well

quantity	cut
acceptance cuts	
polar angle of kaon	$30^\circ < \theta_K < 150^\circ$
transverse momentum of kaon	$0.4\,\mathrm{GeV} < p_{t,K} < 2\,\mathrm{GeV}$
polar angle of pions	$20^\circ < \theta_{\pi_s}, \theta_{\pi_f} < 160^\circ$
transverse momentum of slow pion	$p_{t,\pi_s} < 0.4\,\mathrm{GeV}$
transverse momentum of fast pion	$p_{t,\pi_f} > 0.4\,\mathrm{GeV}$
angle of $\pi^+\pi^-$ decay plane	$\phi^* < 70^\circ \vee \phi^* > 110^\circ$
background rejection cuts	
trans. momentum of pions rel. K^0_S flight direction	$p_{t,rel}(\pi, K) > 0.1\,\mathrm{GeV}$
proton pion invariant mass	$m(p,\pi) > 1.125\,\mathrm{GeV}$
distance of primary and secondary vertex in $r\phi$	$2\,\mathrm{cm} < d_{prim,sec} < 8\,\mathrm{cm}$
track quality cuts	
radial tracklength of pion tracks	$s_{\pi_s,meas}, s_{\pi_f,meas} > 10\,\mathrm{cm}$
quality of vertex fit	$\chi^2 < 10$

Table B.3: Selection criteria for reconstructing K^0_s.

as ϕ^* are applied. The angle ϕ^* defines the orientation of the $\pi^+\pi^-$ decay plane relative to the plane spanned by the z axis and the direction of flight of the K^0_S:

$$\phi^* = \cos^{-1}\left(\frac{\vec{c}\cdot(\vec{p}_{\pi^+}\times\vec{p}_{\pi^-})}{|\vec{c}|\cdot|\vec{p}_{\pi^+}\times\vec{p}_{\pi^-}|}\right) \; with\; \vec{c}\equiv(\vec{p}_{K^0_s}\times\vec{z})\times\vec{p}_{K^0_s}, \tag{B.13}$$

where $\vec{p}_{\pi^+}$, $\vec{p}_{\pi^-}$ and $\vec{p}_{K^0_s}$ are the three momenta of the pions and the kaon respectively. The vector $\vec{z}\equiv(0,0,1)$ defines the direction of the z axis.

To reduce the background further cuts are applied: A minimum $p_{t,rel}(\pi, K^0_s)$ is required to reject converted photons $\gamma \rightarrow e^+e^-$ with opening angle $\sphericalangle(e^+,e^-) \approx 0$. To reduce contributions from Λ baryons ($m_\Lambda = 1.116\,\mathrm{GeV}$ [93]), a cut on the invariant mass of two tracks with proton and pion mass hypothesis $m(p,\pi)$ is made where the particle with the highest three momentum is assumed to be a proton. The minimal requirement on the decay length $d_{prim,sec}$ of the kaon is choosen to get rid of backgroud from particles coming from the primary vertex. The upper cut on the decay length ensures that the tracks to be investigated differ not too much from primary vertex fitted tracks. Otherwise predictions concerning track reconstruction efficiencies made here would be less relevant. Furthermore, a minimum radial tracklength is required which is the same for primary vertex fitted tracks and an upper limit on the χ^2 value of the secondary vertex fit is set.

In Fig. B.13 the invariant mass $M(\pi^+,\pi^-)$ of the V^0 candidates surviving all selection criteria is shown for the data and Monte Carlo. The mass peak of the

K_S^0 is clearly visible. The position of the mass peak for data is compatible with the nominal K_S^0 mass of 0.497 GeV [93]. In the case of Monte Carlo the peak is narrower and shifted by about 2 MeV to the higher mass. There is still some background left. To get the kinematic distributions of the K_S^0 and the decay pions, the background is subtracted using the sideband method. The signal region and both sidebands are shown in Fig. B.13.

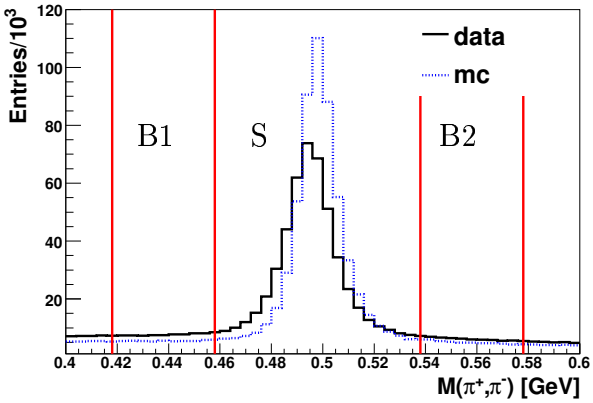

Figure B.13: Invariant mass $M(\pi^+, \pi^-)$ for the selected data (full line) and Monte Carlo (dotted line) sample. Further the signal region S and the sidebands B1 and B2 are indicated by the vertical lines.

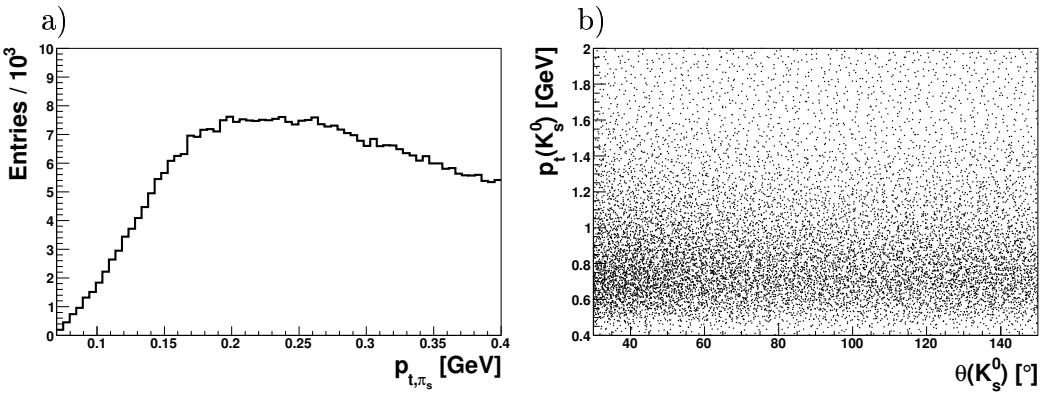

Figure B.14: Background subtracted distributions of the K_s^0 in bins of the transverse momentum of the slow pion p_{t,π_s} (a) and in bins of the polar angle θ_K and transverse momentum $p_{t,K}$ (b)

In Fig. B.14 the K_s^0 spectra in bins of p_{t,π_s} (a) and $[\theta_K, p_{t,K}]$ (b) are shown.

For each bin the sidebands are subtracted. These distributions are the base for the efficiency estimation according to Eq. B.10.

B.2.3 Efficiency Estimate

The efficiency is estimated according to Eq. B.10 using the reconstructed K^0_S spectra $N^m_{K^0}$ in bins of p_{t,π_s} and $\tilde{N}^{j,k}_{K^0}$ in bins of $[\theta_K, p_{t,K}]$. The contributions $f^m_{j,k}$ are numerically calculated as follows: For each $[\theta_K, p_{t,K}]$ bin an isotropic decay in the K^0_S rest frame is simulated by choosing isotropic decay angles $\cos(\theta^*)$ and ϕ^* in 200 equidistant intervalls each. For each direction the corresponding four-vectors of the pions are determined, using the fact that the three momenta are opposite to each other with the same magnitude of 0.206 GeV assuming an invariant mass of 0.497 GeV [93] for K^0_S. All four-vectors are boosted in the laboratory frame according to θ_K and $p_{t,K}$ equal to the center of the j,k bin. In the laboratory frame all selection cuts on the pion tracks according Tab. B.3 are applied except the cut on the decaylength and the track quality cuts. Based on the remaining four vectors $f^m_{j,k}$ is retrieved by counting the number of decays in the m-th p_{t,π_s} bin.

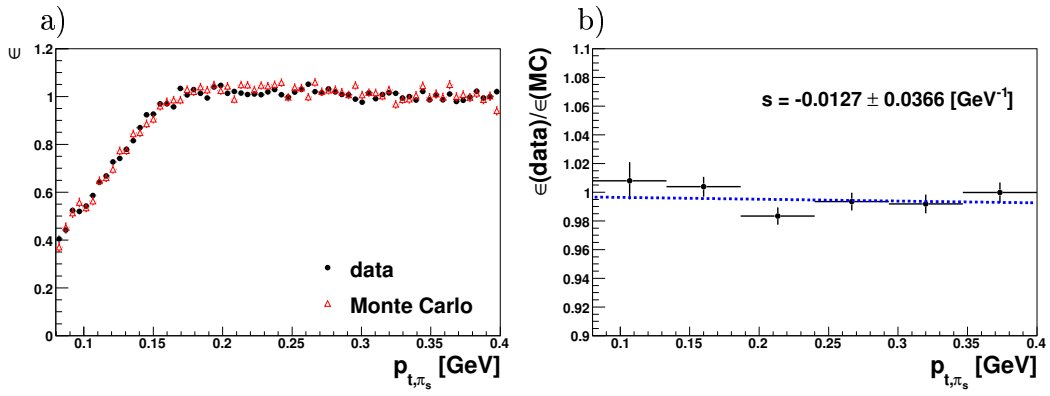

Figure B.15: On the left the track reconstruction efficiencies in bins of the transverse momentum of the slow pion for data and Monte Carlo are shown. In each case the absolute scale is choosen in a way that the mean of the upper 10 bins normalised to 1. The ratio of both efficiencies for data and Monte Carlo with a coarse binning is shown on the right. To this ratio a straight line is fitted with a slope s shown.

The efficiency is calculated by solving Eq. B.10 iteratively. As a first step the efficiency is choosen $\epsilon_m = 1$ for each p_{t,π_s} bin. Then the measured p_{t,π_s} spectrum (left side of Eq. B.10) is divided by the sum calculated with the starting efficiency to get the efficiency for the next iteration. This procedure converges after the

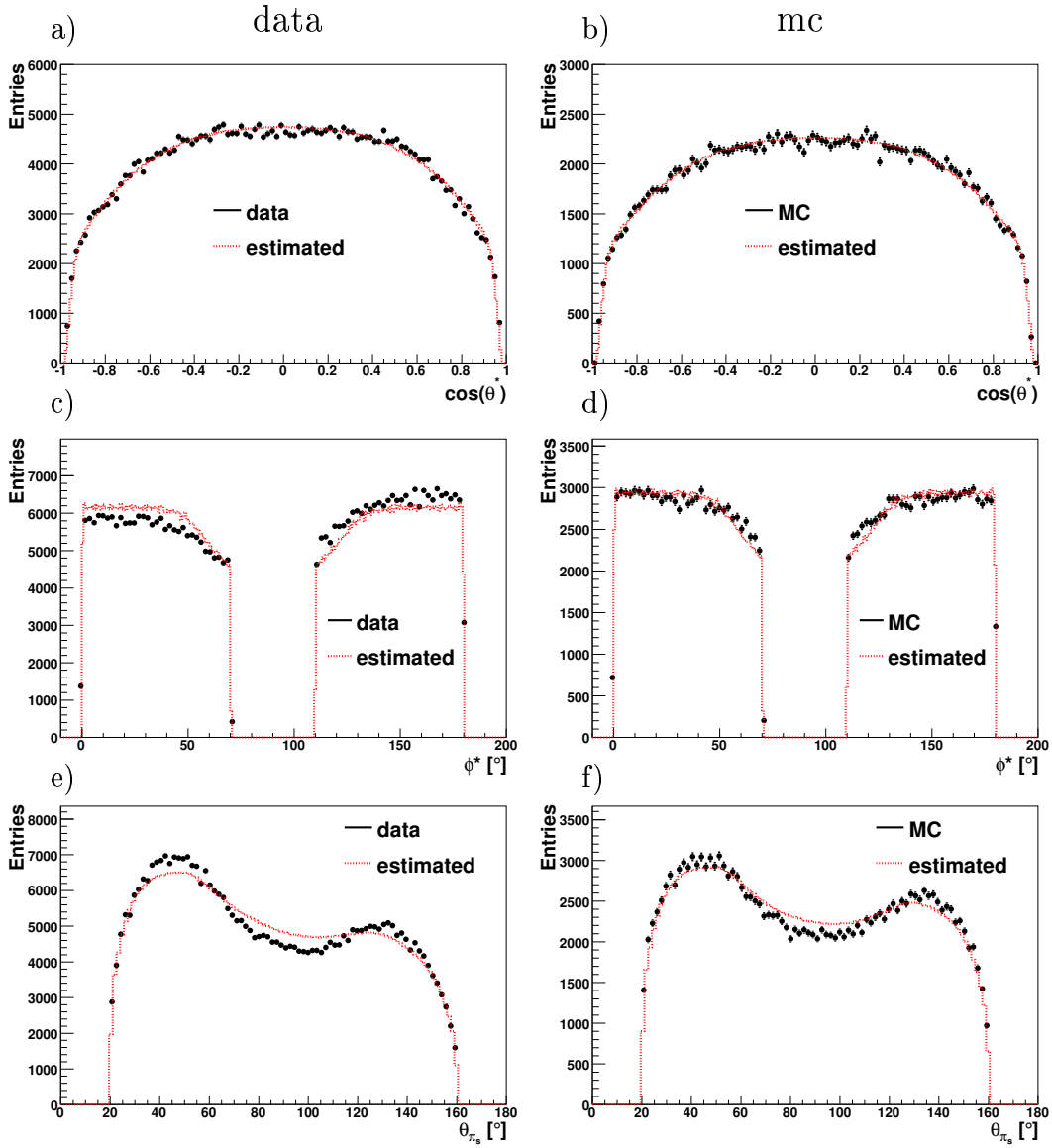

Figure B.16: Control distributions of $\cos\theta^*$, ϕ^* and θ_{π_s} for data (a,c,e) and Monte Carlo (b,d,f). In each case the reconstructed distribution is compared to the distribution estimated from the isotropic decay topology.

fourth iteration. The maximum relative deviation between the measured (left side of Eq. B.10) and expected p_{t,π_s} spectrum (right side of Eq. B.10) is smaller than 0.005. The statistical error on the efficiency is calculated according Eq. B.12.

In Fig. B.15 (a) the resulting efficiency in bins of p_{t,π_s} for the data and Monte Carlo is shown. In each case the absolute normalisation is choosen by normalising the average efficiency in the upper 10 bins to 1. The efficiencies are about 100% for $p_{t,\pi_s} > 0.17\,\mathrm{GeV}$ and drop to 40% at $p_{t,\pi_s} = 0.08\,\mathrm{GeV}$. In Fig. B.15 (b) the ratio of the efficiencies obtained in the data and Monte Carlo is shown. To the ratio a straight line is fitted with a slope s of $s = -0.0127 \pm 0.0366\,\mathrm{GeV}^{-1}$. The change of the efficiency in the considered p_{t,π_s} range is within $\pm 1\%$.

The efficiency determination solving Eq. B.10 means that the p_{t,π_s} dependent efficiency is choosen in a way that the p_{t,π_s} spectra reconstructed in the data and Monte Carlo simulation becomes identical with the calculated p_{t,π_s} spectra. To cross check the efficiency determination it has to be checked in how far reconstructed and calculated spectra in other observables of the kaon decay agree. To get the calculated distributions, the estimated four vectors of the decay pions in the lab frame are statistically weighted with the resulting p_{t,π_s}-dependent efficiency and the number of reconstructed K_S^0 in the j,k bins.

In Fig. B.16 the comparison of the calculated with the reconstructed spectra is shown for data and Monte Carlo in the decay angles $\cos\theta^*$ (a,b) and ϕ^* (c,d) as well as the polar angle of the slow pion θ_{π_s} (e,f). The distributions in $\cos\theta^*$ agree reasonably well whereas in ϕ^* some deviations are observed. In data for $\phi^* < 90°$ the calculated spectrum is above the measured spectrum whereas for $\phi^* > 90°$ the calculation is below. This difference could be related to the different decay topologies: For $\phi^* < 90°$ ($> 90°$) one gets $\vec{p}_{\pi^+} \times \vec{p}_{\pi^-} > 0$ (< 0) according to Eqn. B.13. The two possibilities lead to different reconstruction properties [129]. Both decay topologies in a magnetic field are shown in Fig. B.17. The so-called seagull decay topology (Fig. B.17 a)) belongs to the case $\vec{p}_{\pi^+} \times \vec{p}_{\pi^-} > 0$ whereas

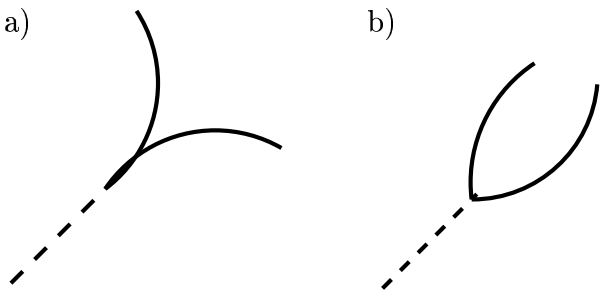

Figure B.17: Decay topologies of K_S^0. Seagull (a)) and Sailor (b)) decay topology.

for $\vec{p}_{\pi^+} \times \vec{p}_{\pi^-} < 0$ the so-called sailor decay topology (Fig. B.17 b)) holds. For the seagull decay topology the track reconstruction is worse than for the other topology because both tracks overlap near the vertex. For future track efficiency studies with K_S^0 the K_S^0 candidates with the seagull decay topology should be removed. The comparison in θ_{π_s} shows a clear disagreement between reconstructed and calculated distributions which is a hint for a θ-dependence of the track reconstruction efficiency. This disagreement is visible for both data and Monte Carlo. It is not a priori clear in how far this effect cancels out within calculating the ratio of the p_{t,π_s} dependent efficiencies from data and Monte Carlo.

B.3 Conclusions

The goal of the track efficiency studies to understand the total track reconstruction efficiency within a systematic error of less than 1% has been partly reached. At transverse momenta below 150 MeV the track reconstruction efficiency has been determined from the curler method with an agreement between data and Monte Carlo within 1%. Still missing is the vertex fit efficiency. The precise determination of the vertex fit efficiency based on the curler sample is not possible since the distinction whether a track comes from the primary vertex or a nearby secondary vertex like a nuclear interaction in the beam pipe can not be made with sufficient accuracy [128]. Within the K_S^0 method the p_t dependence of the total reconstruction efficiency for data and Monte Carlo has been estimated up to a transverse momentum of 400 MeV where the ratio in the efficiencies between data and Monte Carlo changes within 1%. But it has been further shown that there is some hint for a dependence of the reconstruction efficiency on the polar angle of the tracks. This additional dependence has to be considered for the efficiency calculation. A comparison of both methods in the overlap region at $p_t < 150$ MeV is not possible up to now because the curler method provides only the pure track reconstruction efficiency whereas the K_S^0 method makes predictions concerning the p_t dependence of the total track reconstruction efficiency including the vertex fit efficiency.

References

[1] **H1** Collaboration, "Measurement of the D^* Meson Production Cross Section and $F_2^{c\bar{c}}$, at High Q^2, in ep Scattering at HERA," `arXiv:0911.3989 [hep-ex]`.

[2] R. P. Feynman, "Photon-hadron interactions,". Reading 1972, 282p.

[3] J. D. Bjorken, "Asymptotic Sum Rules at Infinite Momentum," *Phys. Rev.* **179** (1969) 1547–1553.

[4] J. Callan, Curtis G. and D. J. Gross, "High-energy electroproduction and the constitution of the electric current," *Phys. Rev. Lett.* **22** (1969) 156–159.

[5] P. Schmueser, *Feynman-Graphen und Eichtheorien für Experimentalphysiker.* Springer, 1995.

[6] W. B. Ellis R.K., Stirling W.J., *QCD and Collider Physics.* Cambridge University Press, 1996.

[7] O. Behnke, "Production of Charm and Beauty Quarks at HERA." Habilitation, Ruprecht-Karls-Universität Heidelberg, 2005.

[8] The **H1** and **ZEUS** Collaborations, "Combined Measurement and QCD Analysis of the Inclusive ep Scattering Cross Sections at HERA," `arXiv:0911.0884 [hep-ex]`.

[9] A. Nikiforov, *Measurement of the Neutral Current $e^{\pm}p$ Cross Sections Using Longitudinally Polarized Lepton Beams at HERA II.* PhD thesis, Ludwig-Maximilians Universität München, 2007.

[10] G. Altarelli and G. Parisi, "Asymptotic Freedom in Parton Language," *Nucl. Phys.* **B126** (1977) 298.

[11] Y. L. Dokshitzer, "Calculation of the Structure Functions for Deep Inelastic Scattering and e+ e- Annihilation by Perturbation Theory in Quantum Chromodynamics. (In Russian)," *Sov. Phys. JETP* **46** (1977) 641–653.

[12] E. A. Kuraev, L. N. Lipatov, and V. S. Fadin, "The Pomeranchuk Singularity in Nonabelian Gauge Theories," *Sov. Phys. JETP* **45** (1977) 199–204.

[13] I. I. Balitsky and L. N. Lipatov, "The Pomeranchuk Singularity in Quantum Chromodynamics," *Sov. J. Nucl. Phys.* **28** (1978) 822–829.

[14] M. Ciafaloni, "Coherence Effects in Initial Jets at Small q**2 / s," *Nucl. Phys.* **B296** (1988) 49.

[15] S. Catani, F. Fiorani, and G. Marchesini, "QCD Coherence in Initial State Radiation," *Phys. Lett.* **B234** (1990) 339.

[16] S. Catani, F. Fiorani, and G. Marchesini, "Small x Behavior of Initial State Radiation in Perturbative QCD," *Nucl. Phys.* **B336** (1990) 18.

[17] G. Marchesini, "QCD coherence in the structure function and associated distributions at small x," *Nucl. Phys.* **B445** (1995) 49–80.

[18] J. Kwiecinski, A. D. Martin, and P. J. Sutton, "The description of F2 at small x incorporating angular ordering," *Phys. Rev.* **D53** (1996) 6094–6099.

[19] J. Kwiecinski, A. D. Martin, and P. J. Sutton, "Constraints on gluon evolution at small x," *Z. Phys.* **C71** (1996) 585–594.

[20] H. Jung, "CCFM prediction for F2 and forward jets at HERA," *Nucl. Phys. Proc. Suppl.* **79** (1999) 429–431.

[21] A. D. Martin, R. G. Roberts, W. J. Stirling, and R. S. Thorne, "MRST2001: Partons and alpha(s) from precise deep inelastic scattering and Tevatron jet data," *Eur. Phys. J.* **C23** (2002) 73–87.

[22] J. Pumplin *et al.*, "New generation of parton distributions with uncertainties from global QCD analysis," *JHEP* **07** (2002) 012.

[23] S. Alekhin, "Parton distributions from deep-inelastic scattering data," *Phys. Rev.* **D68** (2003) 014002.

[24] S. Alekhin, K. Melnikov, and F. Petriello, "Fixed target Drell-Yan data and NNLO QCD fits of parton distribution functions," *Phys. Rev.* **D74** (2006) 054033.

[25] C. Adloff, *Open Charm Production in Deep Inelastic Electron-Proton Scattering with the H1 Detector at HERA.* PhD thesis, University Wuppertal, 2001.

[26] R. S. Thorne and W. K. Tung, "PQCD Formulations with Heavy Quark Masses and Global Analysis," arXiv:0809.0714 [hep-ph].

[27] S. J. Brodsky, P. Hoyer, C. Peterson, and N. Sakai, "The Intrinsic Charm of the Proton," *Phys. Lett.* **B93** (1980) 451–455.

[28] S. J. Brodsky, C. Peterson, and N. Sakai, "Intrinsic Heavy Quark States," *Phys. Rev.* **D23** (1981) 2745.

[29] **H1** Collaboration, C. Adloff *et al.*, "Inclusive D0 and D*+- production in neutral current deep inelastic e p scattering at HERA," *Z. Phys.* **C72** (1996) 593–605.

[30] L. Gladilin, "Charm hadron production fractions," arXiv:hep-ex/9912064.

[31] X. Artru and G. Mennessier, "String model and multiproduction," *Nucl. Phys.* **B70** (1974) 93–115.

[32] M. G. Bowler, "e+ e- Production of Heavy Quarks in the String Model," *Zeit. Phys.* **C11** (1981) 169.

[33] B. Andersson, G. Gustafson, G. Ingelman, and T. Sjostrand, "Parton Fragmentation and String Dynamics," *Phys. Rept.* **97** (1983) 31–145.

[34] B. R. Webber, "A QCD Model for Jet Fragmentation Including Soft Gluon Interference," *Nucl. Phys.* **B238** (1984) 492.

[35] G. Marchesini and B. R. Webber, "Monte Carlo Simulation of General Hard Processes with Coherent QCD Radiation," *Nucl. Phys.* **B310** (1988) 461.

[36] C. Peterson, D. Schlatter, I. Schmitt, and P. M. Zerwas, "Scaling Violations in Inclusive e+ e- Annihilation Spectra," *Phys. Rev.* **D27** (1983) 105.

[37] V. G. Kartvelishvili, A. K. Likhoded, and V. A. Petrov, "On the Fragmentation Functions of Heavy Quarks Into Hadrons," *Phys. Lett.* **B78** (1978) 615.

[38] J. Kuti and V. F. Weisskopf, "Inelastic lepton - nucleon scattering and lepton pair production in the relativistic quark parton model," *Phys. Rev.* **D4** (1971) 3418–3439.

[39] **Belle** Collaboration, J. S. Lange, "Charmed hadrons from fragmentation and B decays," *Int. J. Mod. Phys.* **A21** (2006) 5488–5495.

[40] **H1** Collaboration, F. D. Aaron *et al.*, "Study of Charm Fragmentation into $D^{*\pm}$ Mesons in Deep- Inelastic Scattering at HERA," *Eur. Phys. J.* **C59** (2009) 589–606.

[41] **Particle Data Group** Collaboration, W. M. Yao *et al.*, "Review of particle physics," *J. Phys.* **G33** (2006) 1–1232.

[42] H. Jung, "Hard diffractive scattering in high-energy e p collisions and the Monte Carlo generation RAPGAP," *Comp. Phys. Commun.* **86** (1995) 147–161.

[43] H. Jung and G. P. Salam, "Hadronic final state predictions from CCFM: The hadron- level Monte Carlo generator CASCADE," *Eur. Phys. J.* **C19** (2001) 351–360.

[44] W. K. Tung *et al.*, "Heavy quark mass effects in deep inelastic scattering and global QCD analysis," *JHEP* **02** (2007) 053.

[45] H. Jung, "Un-integrated uPDFs in CCFM," *hep-ph/0411287* (2004) .

[46] M. Hansson and H. Jung, "Status of CCFM: Un-integrated gluon densities," `arXiv:hep-ph/0309009`.

[47] A. Kwiatkowski, H. Spiesberger, and H. J. Mohring, "HERACLES: AN EVENT GENERATOR FOR e p INTERACTIONS AT HERA ENERGIES INCLUDING RADIATIVE PROCESSES: VERSION 1.0," *Comp. Phys. Commun.* **69** (1992) 155–172.

[48] J. Meyer, *Guide for the H1 simulation program H1SIM.* Internal Software-Note 03-11/89, DESY, 1989.

[49] R. Brun *et al*, *GEANT User's Guide.* CERN-DD/EE-84-1, 1987.

[50] **H1** Collaboration, *H1REC docu page.* available at https://www-h1.desy.de/icas/imanuals/h1rec/h1rec9/h1rec.html, DESY, 2008.

[51] B. W. Harris and J. Smith, "Charm quark and D*+- cross sections in deeply inelastic scattering at HERA," *Phys. Rev.* **D57** (1998) 2806–2812.

[52] B. W. Harris and J. Smith, "Heavy quark correlations in deep inelastic electroproduction," *Nucl. Phys.* **B452** (1995) 109–160.

[53] A. D. Martin, W. J. Stirling, and R. S. Thorne, "MRST partons generated in a fixed-flavour scheme," *Phys. Lett.* **B636** (2006) 259–264.

[54] **CTEQ** Collaboration, H. L. Lai *et al.*, "Global QCD analysis of parton structure of the nucleon: CTEQ5 parton distributions," *Eur. Phys. J.* **C12** (2000) 375–392.

[55] C. Sandoval, "Inclusive single hadron production in neutral current deep-inelastic scattering at next-to-leading order," in *Proceedings of XVII International Workshop on Deep-Inelastic Scattering and Related Subjects (DIS 2009).* 2009. [arXiv:0908.0824v1].

[56] C. Sandoval, *Inclusive Production of Hadrons in Neutral and Charged Current Deep Inelastic Scattering.* PhD thesis, Universiät Hamburg, 2009.

[57] P. M. Nadolsky *et al.*, "Implications of CTEQ global analysis for collider observables," *Phys. Rev.* **D78** (2008) 013004.

[58] T. Kneesch, B. A. Kniehl, G. Kramer, and I. Schienbein, "Charmed-Meson Fragmentation Functions with Finite-Mass Corrections," *Nucl. Phys.* **B799** (2008) 34–59.

[59] **H1** Collaboration. See http://www-h1.desy.de/.

[60] **ZEUS** Collaboration. See http://www-zeus.desy.de/.

[61] **HERMES** Collaboration. See http://www-hermes.desy.de/.

[62] **HERA-B** Collaboration. See http://www-hera-b.desy.de/.

[63] DESY, "HERA Home Page." See http://adweb.desy.de/mpy/hera/.

[64] V. Andreev et al. [H1 background working group], "Technical Report on the Beam Induced Backgrounds in the H1 Detector." H1 note H1-IN-606, 2002.

[65] V. Andreev et al. [H1 background working group], "Further Report on the Beam Induced Backgrounds in the H1 Detector." H1 note H1-IN-607, 2003.

[66] **H1** Collaboration, I. Abt *et al.*, "The H1 detector at HERA," *Nucl. Instrum. Meth.* **A386** (1997) 310–347.

[67] **H1** Collaboration, I. Abt *et al.*, "The Tracking, calorimeter and muon detectors of the H1 experiment at HERA," *Nucl. Instrum. Meth.* **A386** (1997) 348–396.

[68] J. Burger *et al.*, "The Central jet chamber of the H1 experiment," *Nucl. Instrum. Meth.* **A279** (1989) 217–222.

[69] **H1** Collaboration, A. Aktas *et al.*, "Tests of QCD factorisation in the diffractive production of dijets in deep-inelastic scattering and photoproduction at HERA," *Eur. Phys. J.* **C51** (2007) 549–568.

[70] D. Pitzl *et al.*, "The H1 silicon vertex detector," *Nucl. Instrum. Meth.* **A454** (2000) 334–349.

[71] M. Cuje *et al.*, "H1 high luminosity upgrade 2000 CIP and Level 1 vertex trigger." DESY-PRC 98/02 and H1 internal note H1-01/98-535, 1998.

[72] M. Urban, *The new CIP2k z-vertex trigger for the H1 experiment at HERA*. PhD thesis, Zürich University, 2004.

[73] V. Blobel, "Central track finding and reconstruction in the h1 detector." talk at H1 (http://www-h1.desy.de/∼blobel/phystat.html), 2003.

[74] V. Blobel, "Central track reconstruction." talk at H1 internal tracking group meeting (https://www-h1.desy.de/idet/itracker/TrackingGroup/AgnMin/Meet041103/blobel041103.pdf), 2004.

[75] **H1 Calorimeter Group** Collaboration, B. Andrieu *et al.*, "The H1 liquid argon calorimeter system," *Nucl. Instrum. Meth.* **A336** (1993) 460–498.

[76] V. Shekelyan, "Simulation and reconstruction in h1 liquid argon calorimetry." H1-internal note H1-04/93-288, 1993.

[77] H. W. L. Goerlich, "Documentation of the lar clustering." H1-internal note H1-12/91-204, 1991.

[78] D. W. C. Issever, K. Bornas, "An improved weighting algorithm to achieve software compensation in a fine grained lar calorimeter." H1-internal note H1-03/03-608, 2003.

[79] **H1 Calorimeter Group** Collaboration, B. Andrieu *et al.*, "Results from pion calibration runs for the H1 liquid argon calorimeter and comparisons with simulations," *Nucl. Instrum. Meth.* **A336** (1993) 499–509.

[80] **H1 SPACAL Group** Collaboration, R. D. Appuhn *et al.*, "The H1 lead/scintillating-fibre calorimeter," *Nucl. Instrum. Meth.* **A386** (1997) 397–408.

[81] **H1 SPACAL Group** Collaboration, T. Nicholls *et al.*, "Performance of an electromagnetic lead / scintillating fiber calorimeter for the H1 detector," *Nucl. Instrum. Meth.* **A374** (1996) 149–156.

[82] **H1** Collaboration, "Luminosity Measurement in the H1 Experiment at HERA." Contributed Paper to the 28th International Conference on High Energy Physics, paper pa17-026, 1996.

[83] H. Bethe and W. Heitler, "On the stopping of fast particles and on the creation of positive electrons," *Proc. Roy. Soc. Lond.* **A146** (1934) 83.

[84] E. Elsen, "Aspects of the H1 trigger and data acquisition system,". Prepared for 2nd Annual Conference on Electronics for Future Colliders, Chestnut Ridge, N.Y., 19-21 May 1992.

[85] **H1** Collaboration, *The H1 ToF and VETO Systems*. available at http://www-h1.desy.de/h1det/tracker/tof/, DESY, 2006.

[86] A. W. Jung, *Measurement of the $D^*\pm$ Meson Cross Section and Extraction of the Charm Contribution ($F_2^c(x, Q^2)$, to the Proton Structure in Deep Inelastic ep Scattering with the H1 Detector at HERA*. PhD thesis, Ruprecht-Karls-Universität, Heidelberg, 2009.

[87] U. Bassler and G. Bernardi, "Structure function measurements and kinematic reconstruction at HERA," *Nucl. Instrum. Meth.* **A426** (1999) 583–598.

[88] M. Peez *et al.*, "An energy flow algorithm for Hadronic Reconstruction in OO: Hadroo2." H1 internal note H1-01/05-616, 2005.

[89] S. Osman and D. Salek, "The Low Pt HFS and Jet Energy Calibration." H1 internal note H1-02/09-631, 2009.

[90] B. Heinemann, *Measurement of Charged Current and Neutral Current Cross Sections in Positron-Proton Collisions at $\sqrt{s} \simeq 300\,\mathrm{GeV}$*. PhD thesis, Universität Hamburg, 1999.

[91] G.A. Schuler and H. Spiesberger, "DJANGO: The Interface for Event Generators HERACLES and LEPTO," in *W. Buchmueller and G. Ingelman, Proceedings of the Workshop: Physics at HERA*, vol. 3, p. 1419, DESY. 1992.

[92] **H1** Collaboration, *H1 Trigger Home Page*. available at https://www-h1.desy.de/itrigger/, DESY, 2007.

[93] **Particle Data Group** Collaboration, C. Amsler *et al.*, "Review of particle physics," *Phys. Lett.* **B667** (2008) 1.

[94] M. O. Boenig, *Messung des D^*-Meson-Produktionsquerschnitts in tiefinelastischer Streuung mit dem H1-Experiment*. PhD thesis, Universität Dortmund, 2007.

[95] J. E. Gaiser, *Charmonium Spectroscopy from radiative Decays of the J/Ψ and Ψ′**. PhD thesis, Stanford University, 1982.

[96] **French-Soviet** Collaboration, P. Granet *et al.*, "Inclusive Production Cross-Sections of Resonances in 32- GeV/c K+ p Interactions," *Nucl. Phys.* **B140** (1978) 389.

[97] W. Verkerke and D. Kirkby. http://roofit.sourceforge.net.

[98] F. James, "MINUIT, Function Minimization and Error Analysis." Computing and networks division, cern geneva, swizerland.

[99] V. Blobel. Desy, 1984. DESY 84-118 (Red Report).

[100] I.G. Knowles, T.Sjöstrand, "CERN yellow report: QCD event generators.," tech. rep., CERN, 1996. http://doc.cern.ch/yellowrep/1996/ 96-01_v2/p103.ps.

[101] C. Niebuhr and S. Schmitt, "Luminosity status report." H1 Physics Plenary, https://www-h1.desy.de/h1/iww/ iminutes/talks.20080605/Niebuhr.pdf, June, 2008.

[102] **H1** Collaboration, K. Daum. Private communication, 2006.

[103] **H1** Collaboration, K. Daum. Private communication, 2007.

[104] D. Pitzl, "CJC theta bias and electron track efficiency." H1 internal Talk, https://www-h1.desy.de/idet/itracker/TrackingGroup/home.html, Dec, 2008.

[105] **H1** Collaboration, A. Aktas *et al.*, "Production of D*+- mesons with dijets in deep-inelastic scattering at HERA," *Eur. Phys. J.* **C51** (2007) 271–287.

[106] **ZEUS** Collaboration, S. Chekanov *et al.*, "Measurement of D+- and D0 production in deep inelastic scattering using a lifetime tag at HERA," *Eur. Phys. J.* **C63** (2009) 171–188.

[107] **ZEUS** Collaboration, S. Chekanov *et al.*, "Measurement of D*+- meson production in ep scattering at low Q^2," *Phys. Lett.* **B649** (2007) 111–121.

[108] The **ZEUS** Collaboration, "Measurement of charm production in deep inelastic scattering at HERA II." ZEUS-prel-06-021, http://www-zeus.desy.de/physics/hfla/public/PublicResults/, 2006.

[109] **ZEUS** Collaboration, S. Chekanov *et al.*, "Measurement of D*+- production in deep inelastic e+- p scattering at HERA," *Phys. Rev.* **D69** (2004) 012004.

[110] R. S. Thorne. Discussion at XV International Workshop on Deep-Inelastic Scattering and Related Subjects, 2007.

[111] E. Laenen, S. Riemersma, J. Smith, and W. L. van Neerven, "Complete O (alpha-s) corrections to heavy flavor structure functions in electroproduction," *Nucl. Phys.* **B392** (1993) 162–228.

[112] E. Laenen, S. Riemersma, J. Smith, and W. L. van Neerven, "O(alpha-s) corrections to heavy flavor inclusive distributions in electroproduction," *Nucl. Phys.* **B392** (1993) 229–250.

[113] **H1** Collaboration, C. Adloff *et al.*, "Inclusive D0 and D*+- production in neutral current deep inelastic e p scattering at HERA," *Z. Phys.* **C72** (1996) 593–605.

[114] **ZEUS** Collaboration, J. Breitweg *et al.*, "D* production in deep inelastic scattering at HERA," *Phys. Lett.* **B407** (1997) 402–418.

[115] **H1** Collaboration, C. Adloff *et al.*, "Measurement of D* meson cross sections at HERA and determination of the gluon density in the proton using NLO QCD," *Nucl. Phys.* **B545** (1999) 21–44.

[116] E. Laenen, S. Riemersma, J. Smith, and W. L. van Neerven, "On the heavy quark content of the nucleon," *Phys. Lett.* **B291** (1992) 325–328.

[117] The **H1** Collaboration, "Measurement of the Charm and Beauty Structure Functions using the H1 Vertex Detector at HERA," `arXiv:0907.2643 [hep-ex]`.

[118] **H1** Collaboration, A. Aktas *et al.*, "Measurement of F2(c anti-c) and F2(b anti-b) at low Q**2 and x using the H1 vertex detector at HERA," *Eur. Phys. J.* **C45** (2006) 23–33.

[119] **H1** Collaboration, F. D. Aaron *et al.*, "A Precision Measurement of the Inclusive ep Scattering Cross Section at HERA," `arXiv:0904.3513 [hep-ex]`.

[120] S. Alekhin, J. Blumlein, S. Klein, and S. Moch, "Variable-Flavor-Number Scheme in Analysis of Heavy-Quark Electro-Production Data," `arXiv:0908.3128 [hep-ph]`.

[121] S. Alekhin and S. Moch, "Higher order QCD corrections to charged-lepton deep- inelastic scattering and global fits of parton distributions," *Phys. Lett.* **B672** (2009) 166–171.

[122] R. S. Thorne, "A variable-flavour number scheme for NNLO," *Phys. Rev.* **D73** (2006) 054019.

[123] A. D. Martin, W. J. Stirling, R. S. Thorne, and G. Watt, "Parton distributions for the LHC," *Eur. Phys. J.* **C63** (2009) 189–285.

[124] The **H1** and **ZEUS** Collaborations, "Combination of $F_2^{c\bar{c}}$ from DIS measurements at HERA." H1prelim-09-171, ZEUS-prel-09-015, https://www-h1.desy.de/h1/www/publications/htmlsplit/H1prelim-09-171.long.html, 2009.

[125] G. Watt, A. D. Martin, W. J. Stirling, and R. S. Thorne, "Recent Progress in Global PDF Analysis," `arXiv:0806.4890 [hep-ph]`.

[126] W. Erdmann, *Untersuchung der Photoproduktion von D^*-Mesonen am ep-Speicherring HERA*. PhD thesis, Eidgenössische Technische Hochschule Zürich, 1996.

[127] *QHQTRK manual (Heavy Flavour track selection code by Lee West).*

[128] **H1** Collaboration, K. Daum. Private communication, 2008.

[129] D. Sunar, *Measurement of $K^{*\pm}(892)$ Production in Deep Inelastic ep Scattering with the H1 Detector at HERA*. PhD thesis, Universiteit Antwerpen, 2009.

Danksagung

Zunächst möchte ich mich bei allen bedanken, die mich während meiner Doktorarbeit bei H1 unterstützt haben. Mein besonderer Dank gilt Frau Prof. Dr. Beate Naroska, die den Abschluss meiner Arbeit zu meinem tiefen Bedauern nicht mehr erleben kann. Ich danke ihr für die Möglichkeit meine Promotion am H1 Experiment durchzuführen und deren Betreuung. Auch an die gemeinsame Zeit bei der Betreuung des Fortgeschrittenenpraktikums denke ich gerne zurück.

Mein besonderer Dank gilt Frau Dr. Katerina Lipka für meine Aufnahme in ihrer Arbeitgruppe und der hervorragenden Betreuung der Arbeit und deren Begutachtung sowie der gemeinsamen Arbeit an unserer Analyse und deren Veröffentlichung. Ich danke dir besonders fuer die freundschaftliche Atmosphäre und der Vielzahl an auflockernden Gesprächen auch jenseits der Physik.

Insbesondere möchte ich mich auch bei Frau Dr. Karin Daum bedanken für die gemeinsam verbrachte Zeit in der Gruppe zusammen mit Katerina sowohl privat als auch bei der Arbeit bei H1. Ich danke dir besonders für die Unterstüzung bei dieser Analyse und den tiefen Einblick in die Spurrekonstruktion bei H1. Ebenfalls danke ich dir für das Korrekturlesen meiner Arbeit.

Herrn Prof. Dr. Robert Klanner danke ich sehr für das Korrekturlesen dieser Arbeit und deren Begutachtung.

Besonders möchte ich mich auch bei Herrn Prof. Dr. Peter Truöl für die Unterstützung unserer Veröffentlichung als Referee sowie des Korrekturlesens meiner Arbeit und der Begutachtung der Disputation bedanken.

Weiterhin möchte ich mich bei Herrn Dr. Benno List bedanken für die vielen hilfreichen Hinweise und Diskussionen zu der Analyse.

Herrn Prof. Dr. Gustav Kramer und Dr. Carlos Sandoval danke ich für die Berechnung der ZMVFNS Vorhersagen, deren Vergleich mit den Daten eine der wesentlichen Botschaften der Arbeit und damit auch unserer Veröffentlichung bilden.

Insbesondere möchte ich mich bei Herrn Dr. Cristinel Diaconu bedanken für das Vertrauen in meine Arbeit und deren Veröffentlichung sowie das Ermöglichen meiner Teilnahme an internationalen Konferenzen um dort Ergebnisse von HERA Messungen zu präsentieren.

Bei Monica Dobre, Dr. Maria Aldaya, Dr. Mira Krämer und Brian Grell bedanke

ich für die gute Zusammenarbeit und die angenehme Büroatmosphäre. Bei Brian Grell bedanke ich mich insbesondere für die Vielzahl an privaten Unternehmungen. Weiterhin bedanke ich mich bei Dr. Katja Krüger, Dr. Olaf Behnke, Dr. Andreas Meyer, Dr. Michael Steder, Dr. Shiraz Habib, Dr. Andreas Werner Jung, Dr. Klaus Urban, Eva Hennekemper, Dr. Deniz Sunar, Dr. Michel Sauter und Dr. Tobias Zimmermann für viele nette Gespräche und auch Hilfestellungen für meine Arbeit.

Ich danke ausserdem allen Mitgliedern der Heavy Flavour Gruppe und der ganzen H1 Kollaboration für die gute Zusammenarbeit und die Unterstützung bei unserer Veröffentlichung.

Weiterhin bedanke ich mich bei allen die für den Betrieb von HERA und H1 verantwortlich waren und diese Analyse erst ermöglicht haben.

Nicht zuletzt bedanke ich mich für die finanzielle Unterstützung dieser Arbeit durch das DESY, dem Bundesministerium für Bildung und Forschung (BMBF) unter den Vertragsnummern 05H09GUF, 05H09VHC, 05H09VHF und 05H16PEA sowie dem Impuls- und Vernetzungsfond der Helmholtzgemeinschaft (HGF) unter der Vertragsnummer VH-NG-401.

Meiner Familie und insbesondere meinem Vater danke ich für die Unterstützung während der letzten Jahre.